AD-A243 113

DTIC
ELECTE
DEC 7 1991
S D
C

The Pennsylvania State University
APPLIED RESEARCH LABORATORY
P.O. Box 30
State College, PA 16804

AN EXPERIMENTAL INVESTIGATION OF THE EFFECTS OF BODY SURFACE SUCTION ON THE WING-BODY JUNCTION VORTEX

by

D. B. Phillips
J. M. Cimbala

Technical Report No. TR 91-016
November 1991

Supported by:
Space and Naval Warfare Systems Command

L.R. Hettche, Director
Applied Research Laboratory

Approved for public release; distribution unlimited

91-17322

91 1209 028

REPORT DOCUMENTATION PAGE

Form Approved
OMB No. 0704-0188

Public reporting burden for this collection of information is estimated to average 1 hour per response, including the time for reviewing instructions, searching existing data sources, gathering and maintaining the data needed, and completing and reviewing the collection of information. Send comments regarding this burden estimate or any other aspect of this collection of information, including suggestions for reducing this burden, to Washington Headquarters Services, Directorate for Information Operations and Reports, 1215 Jefferson Davis Highway, Suite 1204, Arlington, VA 22202-4302, and to the Office of Management and Budget, Paperwork Reduction Project (0704-0188), Washington, DC 20503.

1. AGENCY USE ONLY (Leave blank)	2. REPORT DATE	3. REPORT TYPE AND DATES COVERED
	August 1990	

4. TITLE AND SUBTITLE

An Experimental Investigation of the Effects of Body Surface Suction on the Wing-Body Junction Vortex

5. FUNDING NUMBERS

6. AUTHOR(S)

D. B. Phillips, J. M. Cimbala

7. PERFORMING ORGANIZATION NAME(S) AND ADDRESS(ES)

Applied Research Laboratory
The Pennsylvania State University
P. O. Box 30
State College, PA 16804

8. PERFORMING ORGANIZATION REPORT NUMBER

TR-91-016

9. SPONSORING/MONITORING AGENCY NAME(S) AND ADDRESS(ES)

Space and Naval Warfare Systems Command
Department of the Navy
Washington, DC 20363-5100

10. SPONSORING/MONITORING AGENCY REPORT NUMBER

N000039-88-C-0051

11. SUPPLEMENTARY NOTES

12a. DISTRIBUTION/AVAILABILITY STATEMENT

Unlimited

12b. DISTRIBUTION CODE

13. ABSTRACT *(Maximum 200 words)*

Various techniques of reducing the effect of the wing-body junction vortex were studied and two approaches were implemented experimentally. The results of previous studies using the passive approach of reducing the wing leading edge radius were successfully reproduced. The active method of body surface suction to remove the approaching body boundary layer was also investigated. The elimination of this boundary layer was intended to remove the source of vorticity from which the vortex develops. The ideal or minimum suction flow rate required to totally remove the boundary layer and suppress the vortex was equal to the flow rate through the boundary layer.

Mean velocity data were acquired via five-hole probe surveys at a freestream approach velocity of 7.4 m/s. The velocity data were differentiated to yield mean vorticity contours and net circulation values; these results gave measures of the vortex strength.

(Continued)

14. SUBJECT TERMS

Experiments, body surface suction, wing body function vortex, vorticity, boundary layer

15. NUMBER OF PAGES

110

16. PRICE CODE

17. SECURITY CLASSIFICATION OF REPORT	18. SECURITY CLASSIFICATION OF THIS PAGE	19. SECURITY CLASSIFICATION OF ABSTRACT	20. LIMITATION OF ABSTRACT
Unclassified	Unclassified	Unclassified	SAR

An Experimental Investigation of the Effects of Body Surface Suction on the Wing-Body Junction Vortex

David B. Philips

Abstract (continued)

It was clearly shown that this active technique of body surface suction was capable of suppressing the large scale vortex more completely than known passive techniques. For the rectangular suction hole used, a suction volumetric flow rate of nearly twice the actual boundary layer volumetric flow rate was required to totally eliminate the vortex structure. This greater than ideal suction flow rate and the observed introduction of vorticity at the suction hole edges implied the need for future studies to investigate more efficient designs.

ABSTRACT

Various techniques of reducing the effect of the wing-body junction vortex were studied and two approaches were implemented experimentally. The results of previous studies using the passive approach of reducing the wing leading edge radius were successfully reproduced. The active method of body surface suction to remove the approaching body boundary layer was also investigated. The elimination of this boundary layer was intended to remove the source of vorticity from which the vortex develops. The ideal or minimum suction flow rate required to totally remove the boundary layer and suppress the vortex was equal to the flow rate through the boundary layer .

Mean velocity data were acquired via five-hole probe surveys at a freestream approach velocity of 7.4 m/s. The velocity data were differentiated to yield mean vorticity contours and net circulation values; these results gave measures of the vortex strength.

It was clearly shown that this active technique of body surface suction was capable of suppressing the large scale vortex more completely than known passive techniques. For the rectangular suction hole used, a suction volumetric flow rate of nearly twice the actual boundary layer volumetric flow rate was required to totally eliminate the vortex structure. This greater than ideal suction flow rate and the observed introduction of vorticity at the suction hole edges implied the need for future studies to investigate more efficient designs.

Accession For
NTIS GRA&I
DTIC TAB
Unannounced
Justification
By
Distribution/
Availability Codes
Dist | Avail and/or Special
A-1

QUALITY INSPECTED 4

TABLE OF CONTENTS

LIST OF FIGURES

LIST OF TABLES

LIST OF SYMBOLS

D = horseshoe vortex diameter

Q_s = suction volumetric flow rate

Q^* = nondimensional suction volumetric flow rate

Q_{bl} = boundary layer volumetric flow rate

S = horseshoe vortex standoff distance from wing leading edge

$\vec{V}$ = three-dimensional velocity vector

U, V, W = cartesian velocity components

U_∞ = freestream velocity

X, Y, Z = streamwise, spanwise and transverse coordinates, respectively

$\hat{X}, \hat{Y}, \hat{Z}$ = cartesian coordinates unit vectors

Γ = circulation

δ_{99} = 99% boundary layer thickness

δ^* = boundary layer displacement thickness

θ = boundary layer momentum thickness

ν = kinematic viscosity

$\vec{\omega}$ = three-dimensional vorticity vector

$\omega_x, \omega_y, \omega_z$ = cartesian vorticity components

Chapter 1

INTRODUCTION

1.1. Background

The flow field at a wing-body junction is complicated because of the three-dimensional interaction between the approaching body boundary layer and the pressure field presented by the wing. Due to this adverse pressure gradient imposed on the body boundary layer, the flow separates ahead of the junction, forming a vortex. This vortex structure is sheared by the flow about the wing, being stretched and intensified as it is forced downstream. This phenomenon is referred to as a "horseshoe vortex," because of its horseshoe shape (see Figure 1.1).

Some further light can be shed on the origins of this vortex by examination of the vorticity equation:

$$\begin{array}{ccccc} \frac{D\vec{\omega}}{Dt} & = & \vec{\omega}\cdot\nabla\vec{V} & + & \nu\,\nabla^2\vec{\omega}. \\ (A) & & (B) & & (C) \end{array} \qquad (1.1.1)$$

In a two-dimensional flow, such as a flat plate boundary layer, the vortex stretching term (B) must be zero. Thus the approaching boundary layer represents a balance in the vorticity equation between convection and viscous diffusion of vorticity.

As this bound vorticity approaches the stagnation point of the wing, the flow must decelerate, which reduces the strength of the convective term (A) in Equation 1.1.1. The viscous diffusion term (C) remains of the same order, and thus term (B) becomes nonzero, requiring the flow to be three-dimensional. This vortex stretching term oversees the rearrangement of the boundary layer vorticity into an

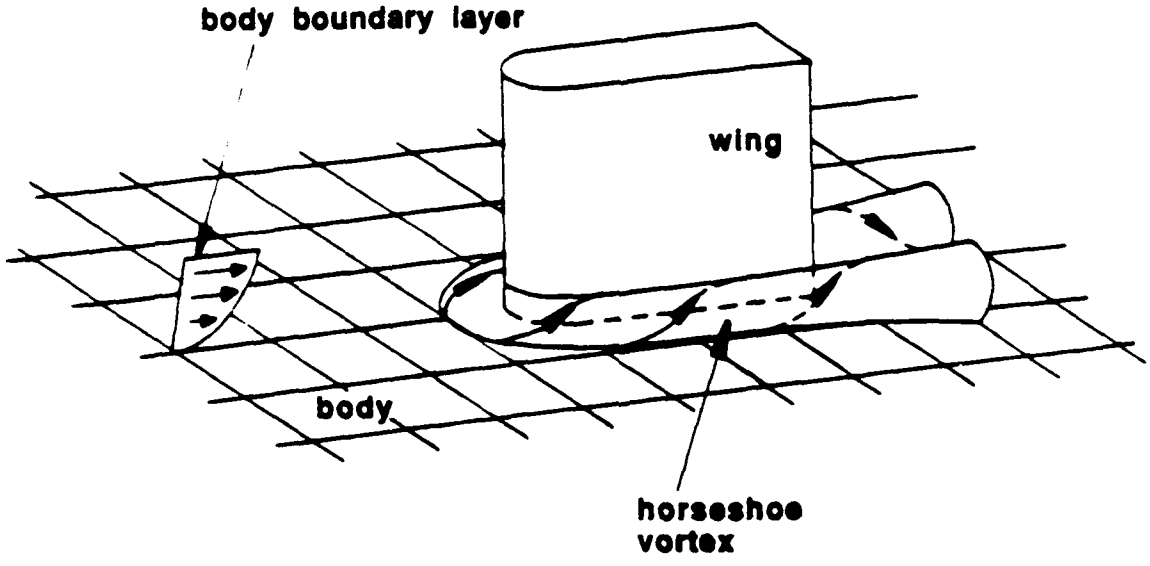

Figure 1.1 The Flow Field in the Vicinity of a Wing–Body Junction

organized vortex. The potential outer flow field of the wing away from the body imposes a strain on the vortex structure. In this manner, downstream of its origin, term (B) will have turned the vortex such that the vorticity vector is largely in the streamwise direction.

A secondary vortex system may also be set up under certain conditions. In this situation, the primary vortex viscously induces one or more counter-rotating vortices due to high local vorticity gradients (Equation 1.1.1, term B). Thus these secondary vortices are expected to be more prominent when the primary vortex is stronger.

By neglecting spanwise and tranverse convection terms, as well as the viscous effects, Equation 1.1.1, can be simplified to

$$\frac{\partial}{\partial X}\left(\frac{\omega_x}{U}\right) = \frac{\omega_x}{U^2}\frac{\partial W}{\partial X}. \tag{1.1.2}$$

In this casting of the vorticity equation, Mehta (1984) states that regions of low U and high $\frac{\partial W}{\partial X}$ correspond to large increases in ω_x. Therefore, the more blunt the wing nose, the larger the streamwise vorticity in the horseshoe vortex legs.

The z-component of vorticity, which can be used to analyze the vortex at its root, is as follows:

$$\omega_z = \frac{\partial U}{\partial Y} - \frac{\partial V}{\partial X}. \tag{1.1.3}$$

(see Appendix C). The streamwise velocities, U, will generally be an order of magnitude greater than any secondary velocities, V. Furthermore, the size of the vortex will be similar to the boundary layer thickness in both the X and Y directions. Using these order of magnitude arguments, it is easily seen that Equation 1.1.3 can be reduced to $\omega_z \sim U_\infty/\delta$. This shows that the vortex strength is mostly a function of the freestream velocity and body boundary layer thickness. This also reflects that the vortex strength will have some dependence on ambient conditions (i.e. temperature and pressure), through δ's dependance on the Reynolds

number. But this is a second order effect at best.

The effects of the horseshoe vortex on the flow field, as well as on downstream mechanical devices are usually undesirable. The vortex structure is well known to be unsteady, and thus can create unwanted vibration and dynamic stresses. Furthermore, the swirling action of the vortex acts to pump high momentum fluid from the freestream into the near body region. This can adversely affect the wing lift characteristics, as well as increase surface shear stresses and thus drag. This pumping action can also increase local heat transfer properties at the surfaces, which at times may be of concern.

This report provides a review of other works attempting to modify the horseshoe vortex structure, and then presents the approach of the current investigation to this problem.

1.2. Previous Vortex Modification Studies

Based on the interpretation of Equation 1.1.2, many studies have been performed attempting to reduce the strength of the horseshoe vortex by modifying the geometry of a standard blunt nosed airfoil. In Mehta's 1984 paper he reports the findings of an experimental study comparing the effect of various two-dimensional wing leading edge shapes on the vortex size and strength. As was expected by the theory, a somewhat weaker and smaller vortex is created when a less blunt leading edge geometry is used. When replacing a fully blunt "super-elliptic" section with a normal elliptic section an 18% circulation reduction results, and the vortex size decreases noticeably. A further 25% circulation reduction and a vortex size decrease is found when replacing the normal elliptic section with a sharp-pointed "wedge-elliptic" wing.

Kubendran et al. (1988) and Sung and Lin (1988) both investigated the effect

of fairings on the horseshoe vortex structure. Kubendran's experiments utilized swept leading edge fairings on the wing to effectively reduce the wing's leading edge radius near the root. This differed from Mehta's work in that the wing was made three-dimensional and swept. Sung and Lin performed a numerical study, utilizing leading and trailing edge fairings similar to those of Kubendran et al. In both of these studies the vortex strength was also reduced.

Devenport et al. (1989) showed that complete fillets in the wing-body corner did not reduce the strength of the vortex. Rather, they concluded that the fillet effectively created a larger nose radius and thus a blunter wing leading edge. Therefore the vortex seemed actually stronger and larger with the fillet than without.

The above geometry modifications aimed at reducing the horseshoe vortex strength were somewhat successful, but none could eliminate the phenomenon totally. Some more direct methods have also been attempted.

Barber (1978) described a series of experiments in which the distance from the wing-body junction to the body leading edge was varied. This had the effect of varying the approaching body boundary layer thickness. It was found that the smaller the boundary layer, the smaller was the region of influence of the vortex. But Barber presented no quantitative data from which the strength of the horseshoe vortex could be estimated; the order of magnitude analysis of Equation 1.1.3 implies that smaller boundary layers may even produce larger values of vorticity.

Barber's work also found that due to the lack of the large vortex, and thus its inherent mixing action, separation off the wing trailing edge occurred prematurely. Furthermore, his method of altering the boundary layer thickness is not appropriate for most real applications.

Vortex generators were applied by McGinley (1987) to produce a vorticity equal

in magnitude but opposite in sign to the vorticity in the legs of the vortex. By locating the generators at the center of the vortex, the generators would act to cancel its vorticity, eliminating it from the flow field. This procedure was found to work well. But the correct location, size, and orientation of the generators are too sensitive to too many factors for this approach to work well in an operating system.

1.3. Motivation and Objectives

From the review of Section 1.2, it can be seen that many passive methods for manipulating the horseshoe vortex have been tried, and often with some success. But none have been totally successful in eliminating the undesired structure. Furthermore, some of these passive methods seem to rely upon the assumption that the flow field will always be in a certain state, without the variation normally occurring in a real application.

As far as the author is aware, no extensive study has ever been performed to investigate active methods of suppressing the horseshoe vortex. Active methods have the natural advantage of being able to change their operating conditions merely by the adjustment of some input signal. In this way, variation in the flow field due to changes in the application state can easily be accomodated.

The possibility of using suction at the body surface to reduce the vortex strength was investigated in this study. Suction at a wing-body junction was also investigated previously by Goldsmith (1961), but his efforts seemed to be concentrated on producing a laminar flow field, and the horseshoe vortex problem was never specifically addressed.

In the present research, two possible suction schemes were initially considered, i.e. eliminating the approaching body boundary layer, or removing the legs of the horseshoe vortex from the flow field downstream of the junction. Only the former

approach was explored; elimination of the body boundary layer removes the source of vorticity from which the vortex develops.

The objective of this work was to establish the feasibility of body surface suction to suppress the horseshoe vortex. A secondary objective was to determine the effect of varying amounts of suction flow rates on the vortex structure.

Chapter 2

EXPERIMENTAL APPARATUS AND PROCEDURE

2.1. Wind Tunnel Description

This experimental research project was performed in the Subsonic Wind Tunnel Facility of the Penn State Mechanical Engineering Department. This open loop suction-type wind tunnel has an operating range of 0 to 15 m/s, and at 5 m/s the freestream turbulence intensity is of order 0.1%. A Buffalo Forge axial flow fan provides the suction power, and its rotation speed is controlled by a Parametrics frequency controller (Parajust B, Model 6075).

The test section of the tunnel is constructed entirely of Plexiglas, except for two aluminum angle supports. The test section is 2.44 m in streamwise length, and 965 mm in transverse width. The height of the section at its inlet is 305 mm, and 318 mm at its exit. This streamwise increase in cross-sectional area is to account for boundary layer displacement effects. The upper wall is segmented into 203, 406, and 610 mm pieces which are removable. This allows access into the tunnel and replacement of tunnel wall sections with special purpose wall segments. Some of these segments are illustrated in Figure 2.1.

2.2. Model and Coordinate System

The wing-body junction was simulated by the intersection of a circular leading edge model with the wind tunnel upper wall (see Figures 2.1 and 2.2). The model's leading edge was built around a 102 mm diameter aluminum duct. The body flaired

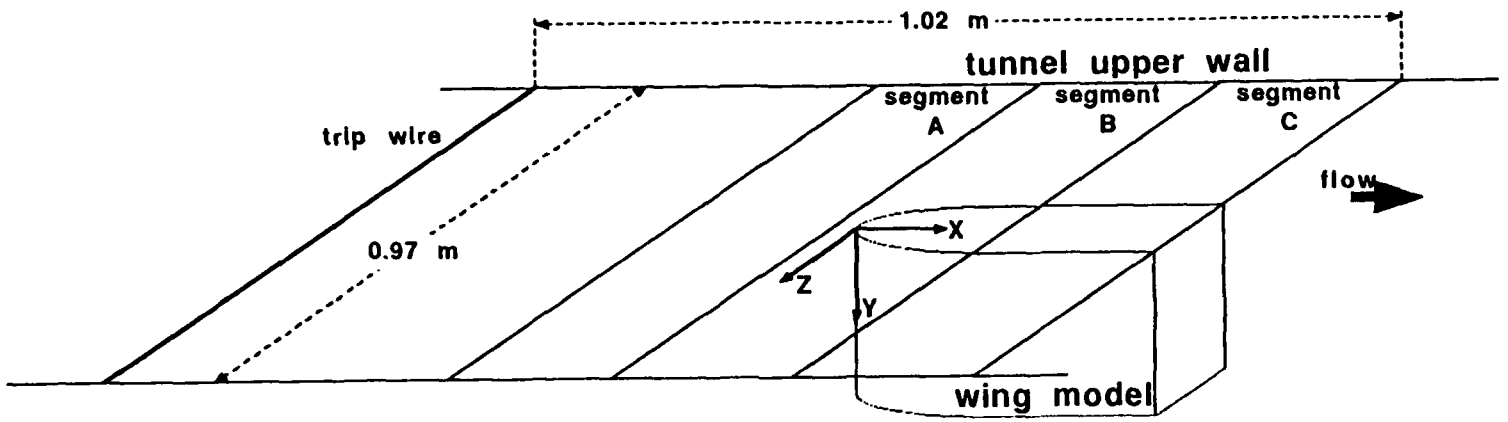

Figure 2.1 Wing–Body Junction Showing Coordinate System Convention (Not Drawn to Scale)

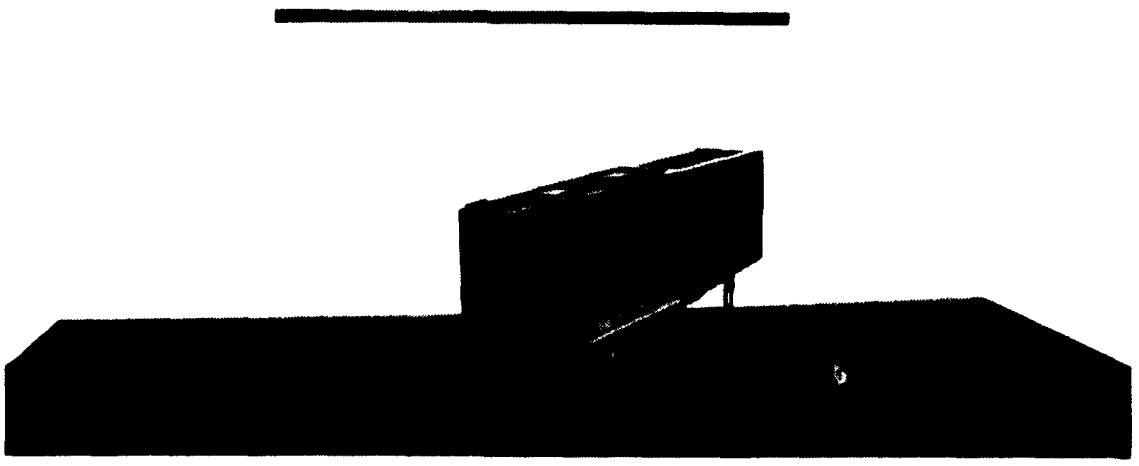

Figure 2.2 Wing Model
(Meter Stick Shown in Background for Scale)

out from this 102 mm width to a constant width of 140 mm for the downstream half of the model. The total length was 900 mm, (not fully shown in Figure 2.1). It was 203 mm in height, being supported on lag bolt legs. The model skeleton was wrapped with two layers of black poster board to give it sufficient rigidity and to reduce visible light reflection (for photographs). The goal was to create a model similar in appearance to a symmetric airfoil with a semi-infinite chord. The final model presented a physical blockage of 9.3% of the test section cross-sectional area.

A left-handed coordinate system was used for this study. As shown in Figure 2.1, the X-axis was parallel to the freestream, and had its origin at the model leading edge. The Y-axis was parallel to the model axis, and had its origin at the upper wall surface. The Z-axis pointed in the wing's transverse direction. The wing model was centered in the wind tunnel (Z-direction), and its leading edge was 1.43 m downstream of the test section inlet.

For all quantitative experiments, the boundary layer was tripped 610 mm upstream of the wing leading edge. In this way, a steady boundary layer transition location was established. The trip wire was 3.5 mm in diameter. No boundary layer trip was used for the flow visualization experiments so that laminar flow could be observed whenever possible.

2.3. Instrumentation and Data Acquisition

Most of the quantitative data acquisition and analysis was performed by a Televideo 386 computer with a math coprocessor, 2 megabytes of random access memory, and a 40 megabyte hard disk drive. Analog data were input via a Metrabyte DAS-16 data acquisition board. This board has other capabilities, including digital output (which was used to control the traversing system). Most of the digital communications were handled by a Metrabyte PIO-96 board, offering

up to 96 bits of digital input or output.

A mechanical multiplexing system was employed to enable the monitoring of multiple pressures with a single transducer. A computer controlled twelve channel Scanivalve acted as this multiplexor (Fluid Switch Wafer W1260/1P-12T). The PIO-96 board switched a relay to supply the valve's solenoid drive with the required 3 amps at 24 volts for channel stepping. Figure 2.3 shows a schematic of the Scanivalve's connections.

An MKS Baratron Differential Pressure Transducer (Type 398), in conjunction with an MKS High Accuracy Signal Conditioner (Type 270B) supplied all pressure measurement needs for determining velocities in the wind tunnel. This system has a 1.0 mm Hg maximum range, with resolution down to 10^{-6} mm Hg. The PIO-96 board was used to read the BCD pressure data of the signal conditioner, as well as remotely control its range setting.

The high pressure side of the transducer was connected to the stagnation pressure line of a pitot-static probe in the freestream. This acted as a universal reference pressure. The low pressure side was connected to the output line of the Scanivalve. Channel twelve of the Scanivalve was also connected to the probe's stagnation pressure, thus allowing a pressure short circuit across the transducer. This enabled the computer to periodically determine the zero offset of the transducer, which made the need for manual zero adjustments unnecessary.

The aforementioned pitot-static probe was 3.2 mm in diameter, and had its static pressure line ported to the first channel of the Scanivalve. Channels two through six of the Scanivalve were connected to the five holes of a five-hole probe. The five-hole probe was used in the non-nulling mode to make all the three-dimensional velocity measurements. This angle-tube type five-hole probe had a tip diameter of 1.7 mm and was handmade at the Pennsylvania State University's

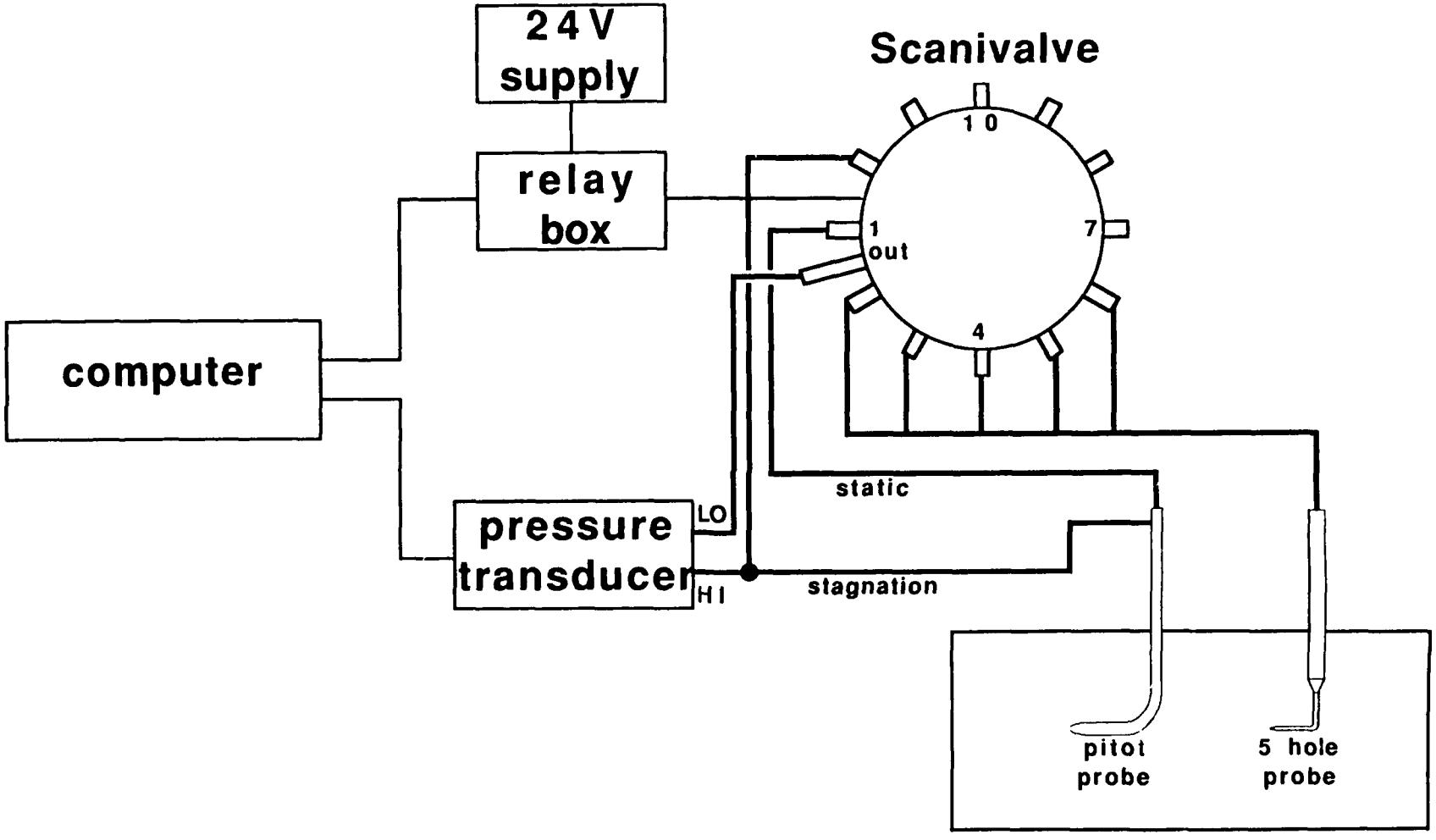

Figure 2.3 Schematic of Scanivalve Connections

Applied Research Laboratory. The calibration and application of this anemometry system is detailed in Appendix A.

The five-hole probe was mounted on a two-dimensional traversing system, made by Unislide Velmex. The traversing system was usually installed on segment C, as shown in Figure 2.1, allowing for velocity measurements in the Y-Z plane, at an X-position approximately at the border between segments B and C. For boundary layer surveys, the traversing system was placed on segment B, to measure the boundary layer approximately at the border between segments A and C. The traverse stepper motors were controlled by a Maxwell Electronics Stepper Motor Controller, Model SMC-102A. This system enabled positioning accuracy down to ± 6 microns.

A barometric pressure transducer (Setra 280) and two electronic thermometers (Stow Labs, Model 911PL) monitored the ambient conditions to allow calculation of air density and viscosity. These data were input to the computer via the DAS-16 board.

2.4. Flow Visualization Equipment

Smoke-wire flow visualization was used for photographing the flow. An in-house built dual-sequence controller synchronized the triggering of the camera and the smoke burning process. The wire was made of Nichrome, 0.13 mm diameter (California Fine Wire Company). The electrical power for burning the smoke from the wire was provided by a VARIAC voltage regulator, adjusted to between 18 and 25 volts AC, depending on the air velocity. A General Radio Strobolume (Model 1540) illuminated the field of view, and a 35 mm Nikon-F camera was used. All photographs presented here were taken with an 80-220 mm zoom lens, some also with a bellows attachment to allow greater variation in the focal length. The

film used was Kodak Tri-X Pan, black and white, ASA 400.

2.5. Suction System

When desired, boundary layer suction was achieved by replacing segment A of the tunnel upper wall (see Figure 2.1) with a specially designed segment. The segment had a 150 mm wide (in the Z-direction) and 190 mm long (in the X-direction) rectangular hole cut in its center (see Figure 2.4). The inside surface of this wall segment was covered with dense screening, to produce the required porous wall.

Suction was applied at the hole by a variable power centrifugal pump (Lamb Electric), having inlet and exit diameters of 72 mm. To reduce the volumetric flow rate lower than the power controller could allow, an orifice attachment was placed on the pump exhaust. Several different orifice hole sizes were used.

The differential pressure between static pressure taps at the tunnel upper wall and the pump inlet was monitored. Another MKS Baratron system was used here, this one with a 10 mm Hg maximum range; the readings were monitored by analog output to the DAS-16 board. This pressure provided a convenient method of monitoring the activity of the pump over long periods of time, but was not used for any quantitative measurement.

By placing a pitot-static probe in the pump exit flow at various points, an average exit velocity could be estimated. From this a volumetric flow rate was determined, using a one-dimensional flow approximation. The probe used for this was 1.7 mm in diameter, and was employed in conjunction with a Validyne transducer and signal conditioner (Models DP15-22 and CD23, respectively).

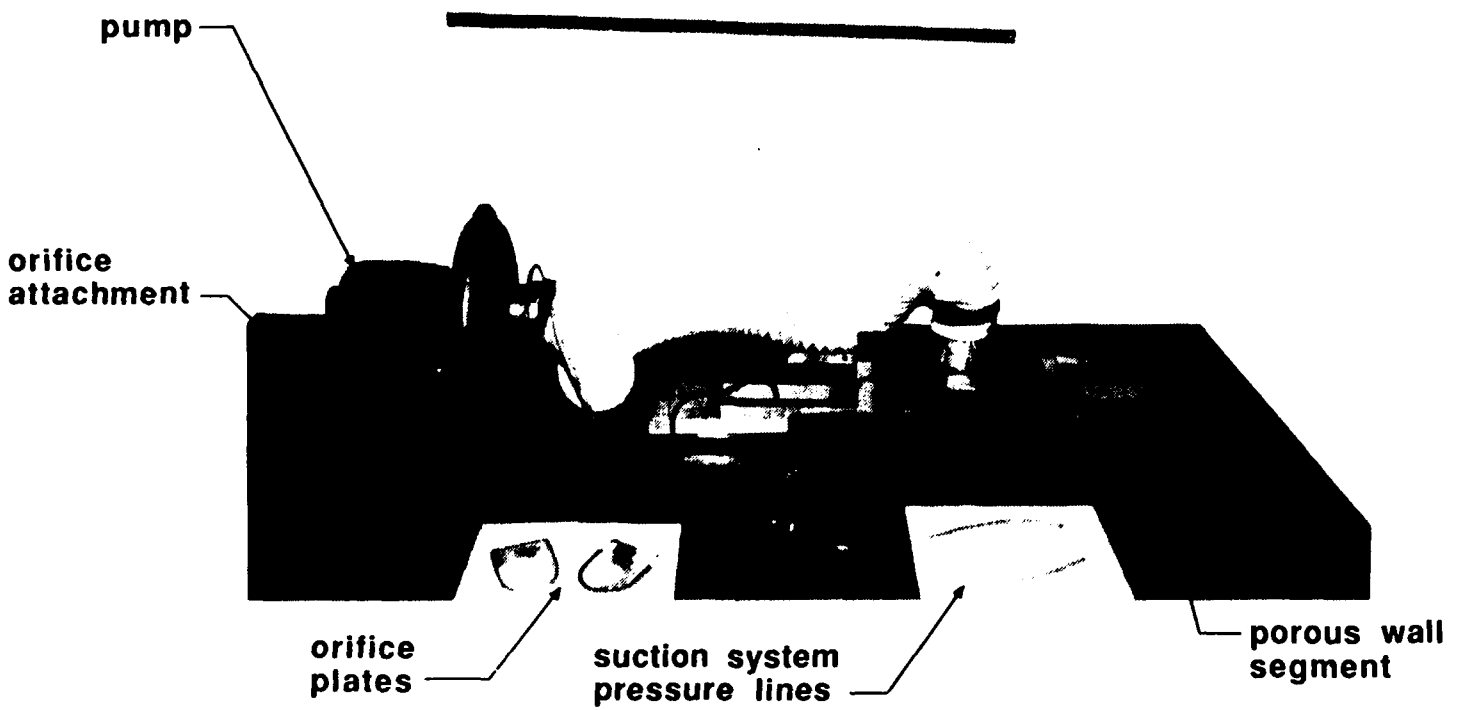

Figure 2.4 Suction System Components
(Meter Stick Shown in Background for Scale)

2.6. Experimental Procedure

The five-hole probe was calibrated at a Reynolds number based on its tip diameter of 890. This corresponds to a velocity of approximately 8.2 m/s, the exact value depending on the kinematic viscosity of air at that time. To minimize Reynolds number effects on the five-hole probe, it was desired to adjust the tunnel wind speed such that the probe would be making measurements at its calibration Reynolds number. Because the wing model presented a nonnegligible blockage, it was required that the freestream monitoring pitot-static probe be placed at approximately the same streamwise and spanwise position as the five-hole probe, (except on the negative Z side of the wing model).

The discrepancy between the approach freestream velocity and the velocity measured at the pitot-static probe was somewhat accounted for by obtaining boundary layer surveys at a wind speed of 7.4 m/s. This corresponds to (100% - 9.3%)×8.2 m/s, where 9.3% is the area blockage of the model. All boundary layer surveys were taken in a vertical line at $X = 0$ and $Z = 0$, with the model removed from the test section. The boundary layer survey data for all experimental situations are included in Appendix D.

As discussed above, velocity vector data were measured utilizing a five-hole probe system. The probe was mounted on a Y-Z traversing system such that the probe tip was always in a plane located at a streamwise position of $X = 215$ mm. Grid points for data acquisition were evenly spaced at intervals of 2.0 mm. The grid spanned an area from $Y = 2.0$ mm to $Y = 40.0$ mm, and from $Z = 70.0$ mm to $Z = 154.0$ mm. The transverse position of $Z = 70.0$ mm corresponded to approximately 8 mm from the wing surface, at that streamwise location. These parameters specified a spatial grid of 860 points.

Once the data were acquired, they were Fourier filtered by a two-dimensional

Fourier algorithm, as described in Section A.4. Cutoff wave numbers for the low-pass filter were 50 m^{-1} for the Y-frequency component, and 35 m^{-1} for the Z-frequency component. These cutoffs were used for all data sets.

The filtered data were then differentiated to obtain streamwise vorticity data. The method of vorticity calculation for this discrete data set is described in Appendix C.

2.7. Comment on Property Drifts

A typical data acquisition survey of the desired 860 spatial data points required 50 to 54 hours to complete. This introduces the question of how much the wind speed and ambient conditions drifted during the procedure. As was discussed in Section 1.1, the fluid dynamic quantities of primary concern are the wind speed and the boundary layer thickness. For these surveys, the boundary layer was always tripped well ahead of the model, making it turbulent and thus fairly impervious to small changes in Reynolds number.

Figures 2.5 show an example of the temporal drifts in a typical experiment. Cyclical drifts with a period of approximately 24 hours can be observed, due primarily to ambient temperature variations. Figure 2.5b displays the drift of the Reynolds number (based on five-hole probe tip diameter); it was maintained to better than a $\pm 5\%$ deviation. More importantly, the air speed was maintained to better than a $\pm 1\%$ deviation, as seen in Figure 2.5a. The pressure monitored across the suction system deviated by between $\pm 5\%$ and $\pm 10\%$ from its mean, depending on the amount of suction applied (see Figure 2.5c).

These drifting conditions were not taken into account in any way in the final data reduction. So for the purposes of this investigation, the $\pm 10\%$ deviation was marginally acceptable. Appendix D includes property drift plots for all experiments.

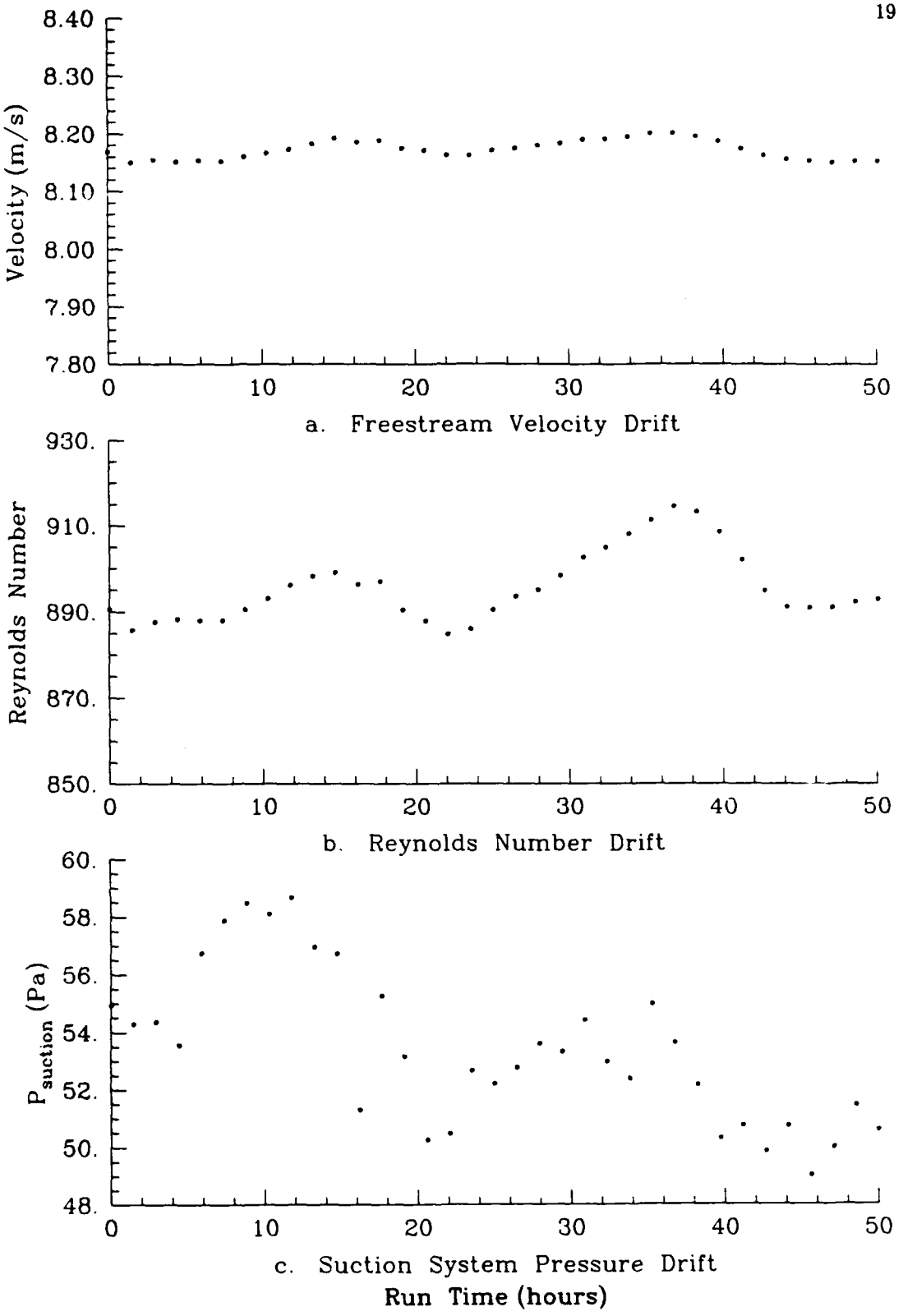

Figure 2.5 Example Property Drifts during One Experiment

Chapter 3

UNMODIFIED VORTEX RESULTS

3.1. Flow Visualization

Smoke-wire flow visualizations were performed over a range of velocities to acquire qualitative information regarding the nature of the unmodified horseshoe vortex. It was found that this flow visualization technique was most effective from about 1 m/s to 5 m/s, and as such this was the velocity range studied.

For wind speeds in the vicinity of 1 m/s, the flow field was entirely laminar, making high contrast photographs possible. At the higher speeds, turbulence was encountered at the wing-body junction. This turbulent flow quickly diffused the smoke, usually creating a blurred photographic image. To minimize this difficulty, a trip wire was not employed for flow visualizations.

Higher contrast photographs were sometimes produced by moving the wire closer to the junction, so that the smoke had less time to be diffused. But this did have the disadvantage that less of the flow field could be visualized. For the photographs presented here the wire was always placed at one of the following streamwise positions: $X = -76$ mm, or $X = -38$ mm. The smoke wire was always placed at a centered Z-location ($Z = 0$), allowing visualization of the plane of symmetry, (containing the horseshoe vortex root).

Many photographs taken did not display the vortex structure. This was primarily due to the variable quantity of smoke which was captured by the vortex. A total of over 500 negatives were shot, of which the 26 best were made into prints. Of these, the eight best are presented here.

Visualizations of the horseshoe vortex at a wind speed of 1 m/s are shown in Figures 3.1 and 3.2. For both photographs, the flow is from left to right and the smoke wire was located at $X = -76$ mm, visible as a faint vertical line at the left edge of Figure 3.1. The needle for administering the oil is also visible as the thicker line at the top of the smoke wire. The object at the right edge of the figure is the wing model leading edge. The tunnel upper wall is visible due to the reflection of the smoke lines, at the top of the picture.

Two linear measurements can be made from these photographs, to quantify the information. The first is the approximate size of the vortex, measured as the diameter, D, of the largest loop of smoke. The second is the standoff distance, S; this is the distance from the apparent center of the vortex to the model leading edge. These dimensions were not constant throughout the study due to the unsteady nature of the horseshoe vortex, and the varying amount of smoke that was captured by the vortex during each exposure.

For Figure 3.1, the vortex diameter is about 13 mm, and the standoff distance is about 23 mm. For Figure 3.2, $D \approx 12$ mm and $S \approx 20$ mm.

Figures 3.3 and 3.4 show the vortex root at a freestream velocity of 2 m/s. The smoke wire was located at $X = -76$ mm for Figure 3.3, in this case showing turbulence in the boundary layer and vortex structure (illustrated by the blurred smoke lines). Because of the turbulent diffusion of the smoke, a clearer visualization was obtained by placing the wire at $X = -38$ mm, as shown in Figure 3.4. Both of these photographs displayed somewhat larger than average vortex diameters of $D \approx 15$ mm; also for both figures, $S \approx 15$ mm.

Flow visualizations for a wind speed of 3 m/s are presented in Figures 3.5 and 3.6. For the first of these the smoke wire was located at the $X = -76$ mm station, and for the latter the wire was located at $X = -38$ mm. Again, the blurred

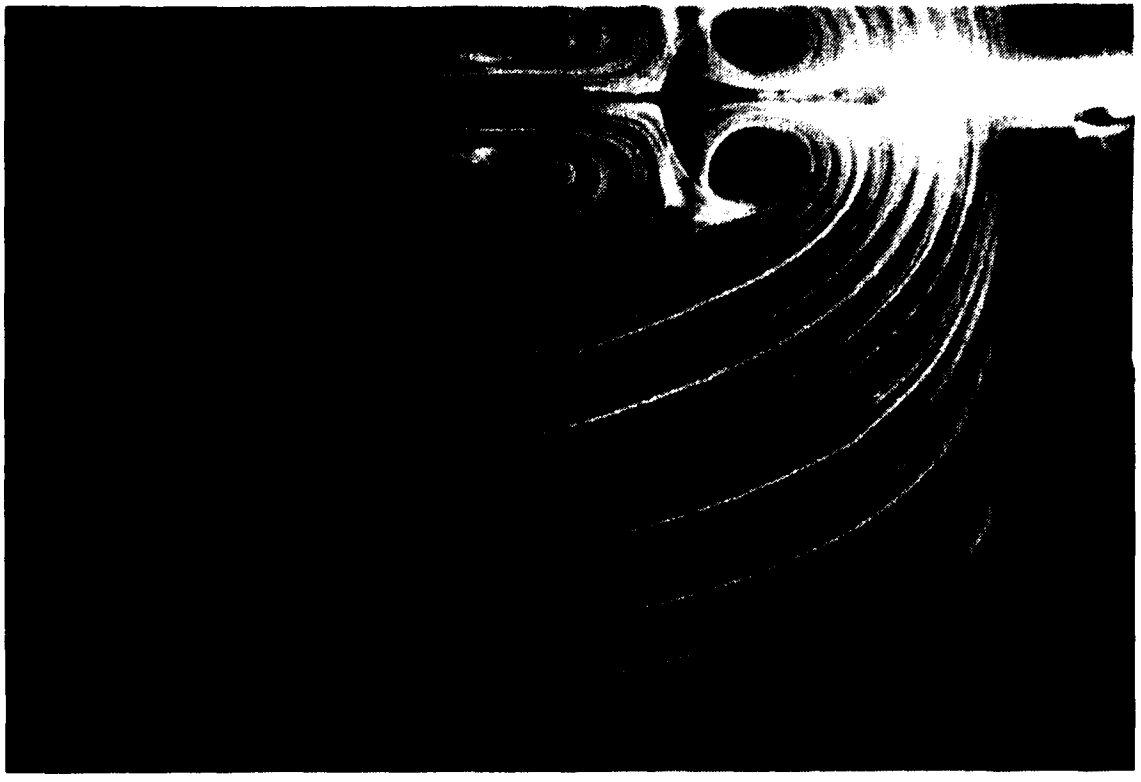

Figure 3.1 Smoke-Wire Flow Visualization at U_∞ = 1 m/s
$X_{smoke\ wire}$ = −76 mm, D = 13 mm, S = 23 mm

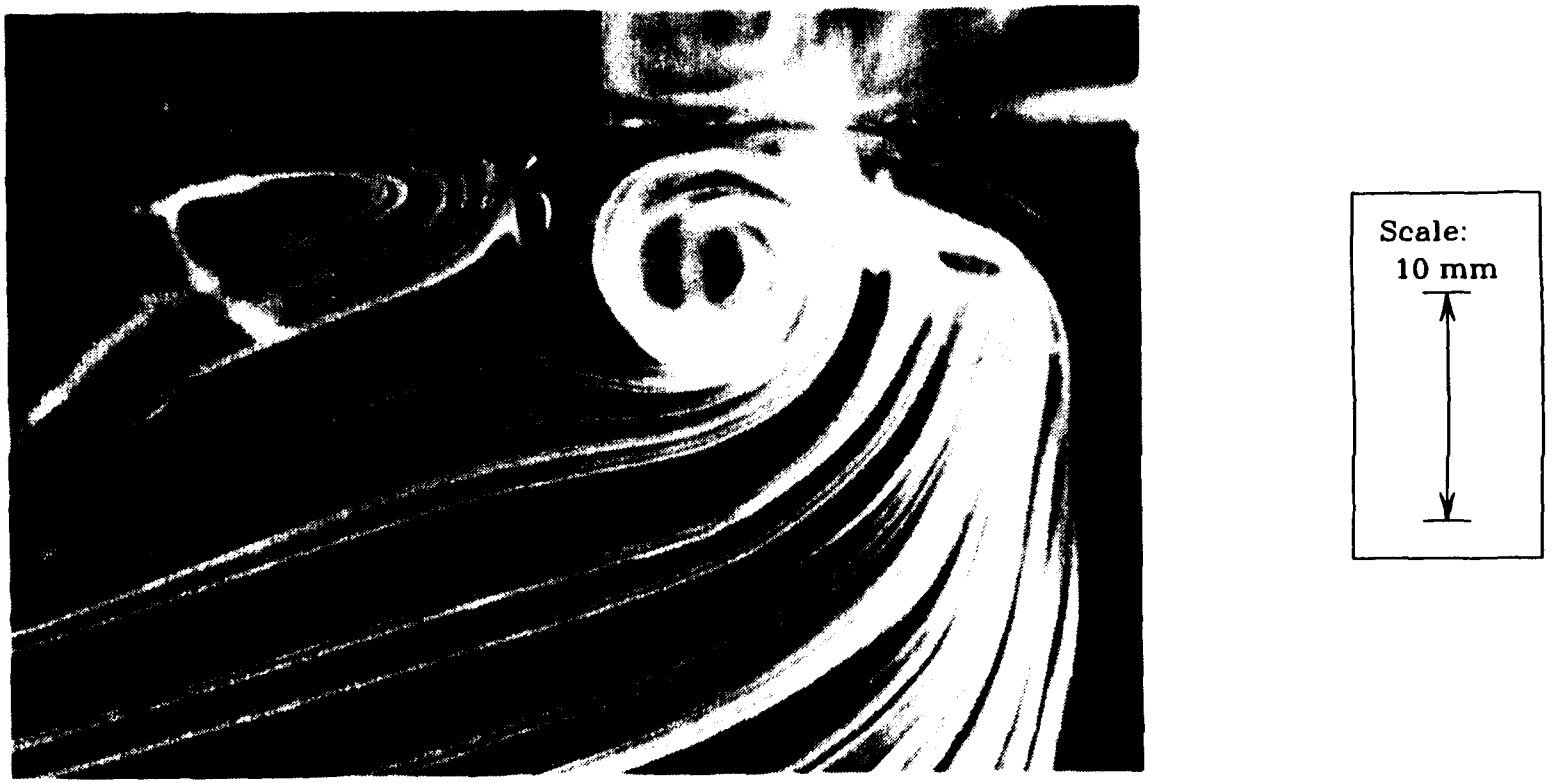

Figure 3.2 Smoke-Wire Flow Visualization at U_∞ = 1 m/s
$X_{smoke\ wire}$ = −76 mm, D = 12 mm, S = 20 mm

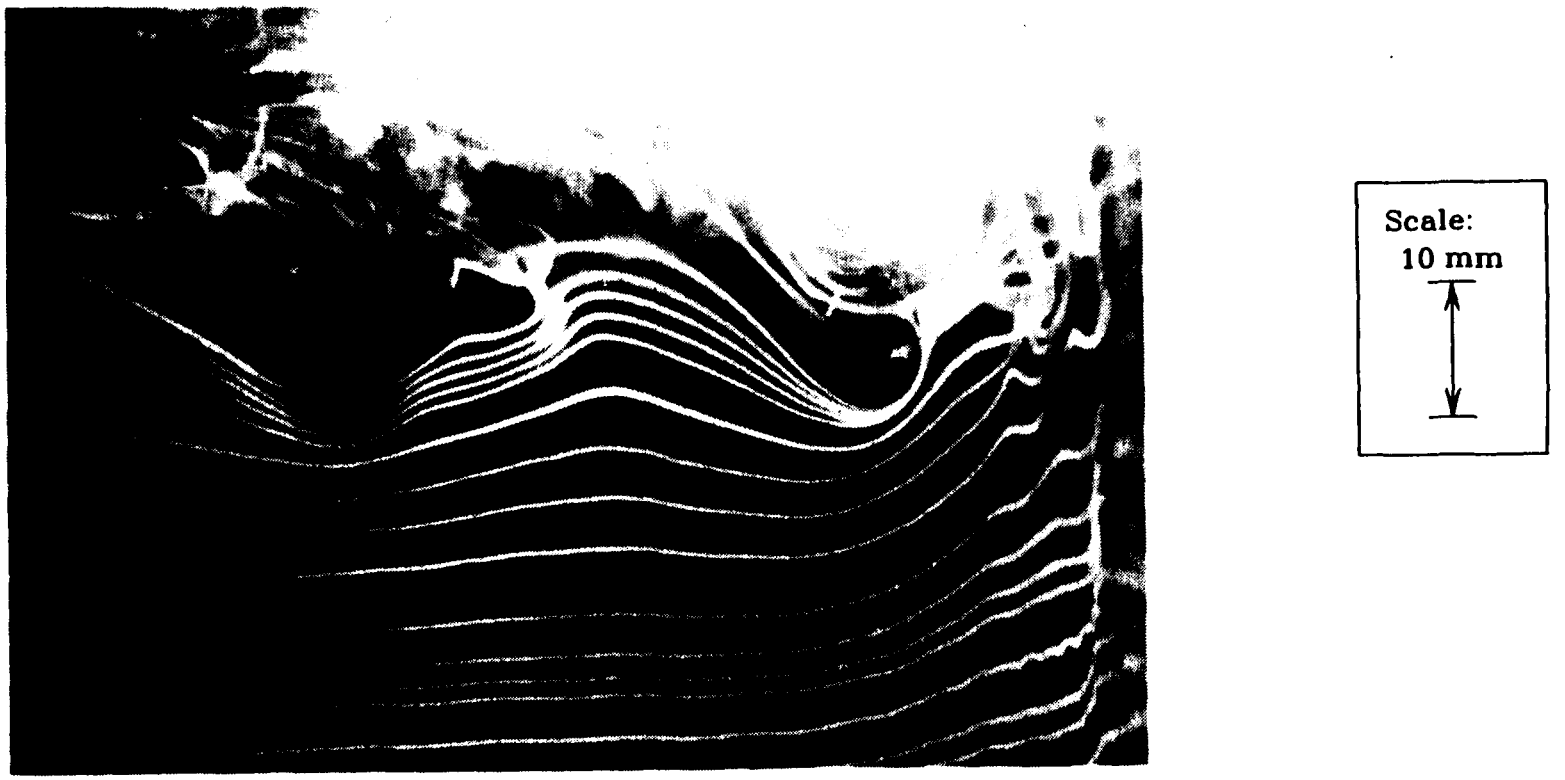

Figure 3.3 Smoke–Wire Flow Visualization at $U_\infty = 2$ m/s
$X_{\text{smoke wire}} = -76$ mm, D = 16 mm, S = 14 mm

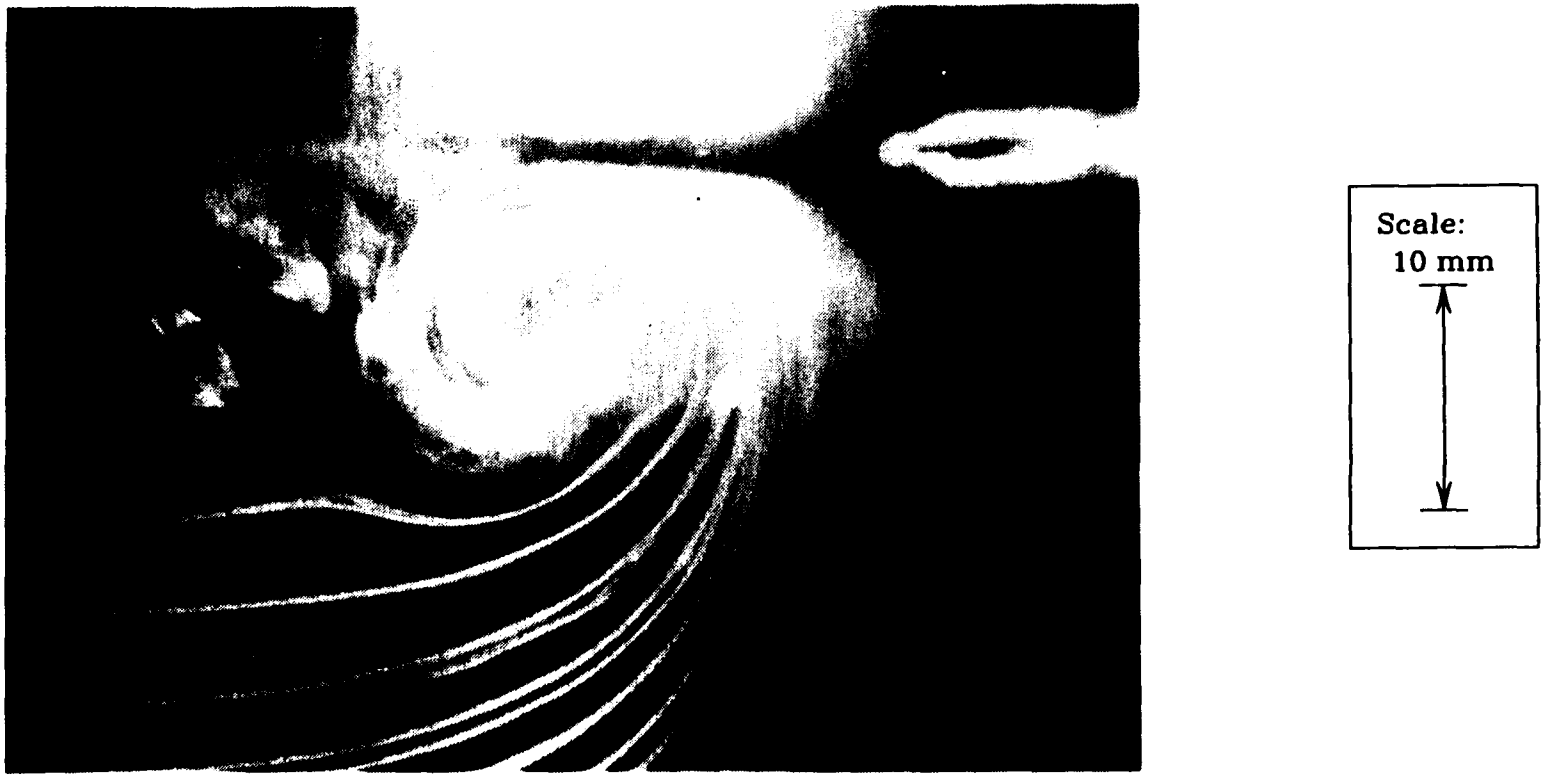

Figure 3.4 Smoke–Wire Flow Visualization at $U_\infty = 2$ m/s
$X_{\text{smoke wire}} = -38$ mm, D = 15 mm, S = 15 mm

Figure 3.5 Smoke-Wire Flow Visualization at $U_\infty = 3$ m/s
$X_{smoke\ wire} = -76$ mm, D = 13 mm, S = 16 mm

Figure 3.6 Smoke-Wire Flow Visualization at $U_\infty = 3$ m/s
$X_{\text{smoke wire}} = -38$ mm, D = 11 mm, S = 16 mm

smoke images imply a turbulent flow field. In Figure 3.6, a smaller secondary vortex also seems to be visible just downstream of the oil supply needle. Figure 3.5 shows a vortex diameter of about 13 mm, and a standoff distance of about 16 mm. The visualization of Figure 3.6 yields $D \approx 11$ mm and $S \approx 16$ mm.

Figures 3.7 and 3.8 were photographed at a freestream velocity of 5 m/s, both of which having the smoke wire placed at the $X = -38$ mm station. Just upstream of the major vortex, a secondary vortex seems to be visible in both of these figures. A vortex diameter of 8 mm is seen in Figure 3.7, with a standoff distance of 17 mm. Figure 3.8 has $D \approx 10$ mm and $S \approx 19$ mm.

A summary of the dimensions measured for all 26 printed photographs is given in Table 3.1. For reference, the accompanying Figure 3.9 illustrates the definitions of the vortex dimensions. The diameter of the visualized vortex seems to be independent of the freestream velocity, in the range of velocities investigated. It is not obvious from these data whether or not the standoff distance varies with velocity. It should be noted that the mean standoff distance for each velocity set is within a standard deviation of the overall mean standoff distance. Therefore it seems that S is at most a weak function of freestream velocity, in this range. One pattern that can be observed is the apparent decrease in the standoff distance standard deviation with increasing velocity. This may be a consequence of the increasing turbulence intensity stabilizing the vortex's dependancy on fluctuating parameters. The observed velocity independence of the vortex's dimensions agrees with Dickinson's conclusions in his December, 1986 report.

The successful visualization of secondary vortices did seem to occur more often at higher velocities. As these secondary vortices were induced by the vorticity gradients setup by the primary vortex, one can infer that the primary vortex became stronger at higher wind speeds, even if its size did not change appreciably. This

Figure 3.7 Smoke-Wire Flow Visualization at $U_\infty = 5$ m/s
$X_{\text{smoke wire}} = -38$ mm, D = 8 mm, S = 17 mm

Figure 3.8 Smoke-Wire Flow Visualization at $U_\infty = 5$ m/s
$X_{smoke\ wire} = -38$ mm, D = 10 mm, S = 19 mm

Table 3.1 Summary of Measurements from Flow-Visualization Prints

Velocity	Number of Photographs Used	Diameter, D		Standoff Distance, S	
		mean	*standard deviation*	*mean*	*standard deviation*
1 m/s	6	11 mm	2 mm	21 mm	9 mm
2 m/s	9	10 mm	3 mm	15 mm	2 mm
3 m/s	7	10 mm	2 mm	17 mm	3 mm
5 m/s	4	11 mm	3 mm	18 mm	1 mm
Overall	26	10 mm	3 mm	17 mm	5 mm

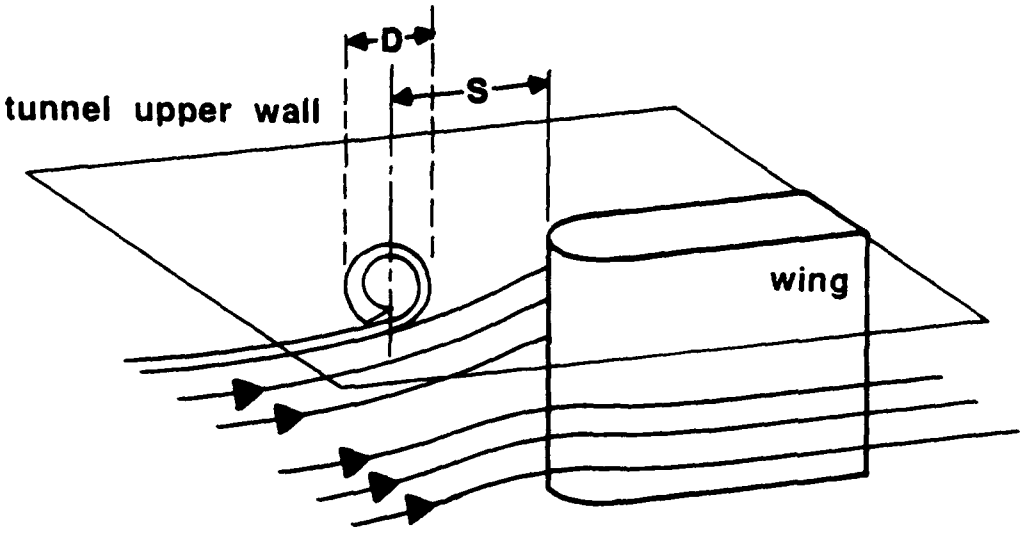

Figure 3.9 Wing-Body Junction Showing Definitions of Vortex Diameter, D, and Standoff Distance, S

agrees with the order of magnitude analysis of Equation 1.1.2, $\omega_z \sim U_\infty/\delta$, if δ is assumed approximately constant.

3.2. Five-Hole Probe Measurements - Solid Walled Body

The experimental procedure for quantitative data acquisition utilizing a five-hole probe system is detailed in Section 2.6. As discussed there, all five-hole probe surveys were made with an approach freestream velocity of 7.4 m/s. A boundary layer survey was performed at the streamwise location of the model leading edge, with the model removed from the test section (all boundary layer data plots are included in Appendix D). This yielded an approximate 99% boundary layer thickness of $\delta_{99} \approx 30$ mm (boundary layer measurements cannot be considered totally accurate due to five-hole probe Reynolds number effects being neglected). Based upon this boundary layer survey, a boundary layer displacement thickness of $\delta^* \approx 5$ mm and a momentum thickness of $\theta \approx 2$ mm were calculated. The volumetric flow rate through a control volume enclosing the boundary layer (up to δ_{99}), and being 150 mm wide (in the Z-direction) is calculated to be $Q_{bl} \approx 0.026\text{m}^3/\text{s}$. This is a reference volumetric flow rate, to allow nondimensionalization of suction volumetric flow rates in later experiments.

The flow field in one leg of the horseshoe vortex was measured with an unmodified wing geometry and the usual solid wall of the wind tunnel. Figure 3.10 shows the fourier filtered secondary flow velocity vectors measured by the five-hole probe. In this study the secondary flow velocity vectors are defined as a projection of the three-dimensional velocity field onto the Y-Z plane:

$$\vec{V}_{secondary} = \vec{V} \cdot \hat{Y} + \vec{V} \cdot \hat{Z}. \tag{3.2.1}$$

The wing model surface was located at $Z = 62$ mm at this streamwise position

of $X = 215$ mm. The wind tunnel wall coincides with the Z-axis. The data have been plotted such that the vector arrow lengths are equal to the distance a fluid particle would travel in 2 milliseconds if the particle traveled in a straight path from the arrow origin. The arrow origin corresponds to the spatial point at which each velocity datum was acquired.

All the data points in Figure 3.10 display a velocity in the positive Z-direction. This flow away from the wing is due to the increasing thickness of the model with streamwise distance; therefore this observation can be accounted for entirely by potential flow effects. A positive Y-flow can also be seen in the region close to the wind tunnel wall, and close to the wing surface. This is probably due largely to boundary layer growths.

In the center of the measured flow field shown in Figure 3.10, a flow turning seems to have occurred. This phenomenon must be the horseshoe vortex, as it cannot be accounted for by any other effect.

A streamwise vorticity contour plot calculated for this data set is shown in Figure 3.11. As described in Appendix C, the Diamond Cell approach for computing vorticities was used. The contours are plotted in increments of $25\,s^{-1}$, with the thicker contour lines being multiples of $50\,s^{-1}$. Negative vorticity contours are shown as dashed lines, and the contour of $0\,s^{-1}$ has not been plotted, for clarity.

The center of the flow turning discussed above for Figure 3.10 is at approximately $Y = 12$ mm, and $Z = 112$ mm. This corresponds to a region of high vorticity in Figure 3.11. The flattened shape of the vortex agrees with the findings reported in Dickinson's March 1986 paper, where he described it as a "tank track".

The contour of maximum vorticity in Figure 3.11 has a value of $100\,s^{-1}$, implying that the greatest calculated vorticity value was slightly in excess of $100\,s^{-1}$. Recall that the order of magnitude analysis of Equation 1.1.2 yields: $\omega_z = U_\infty/\delta = 200\,s^{-1}$,

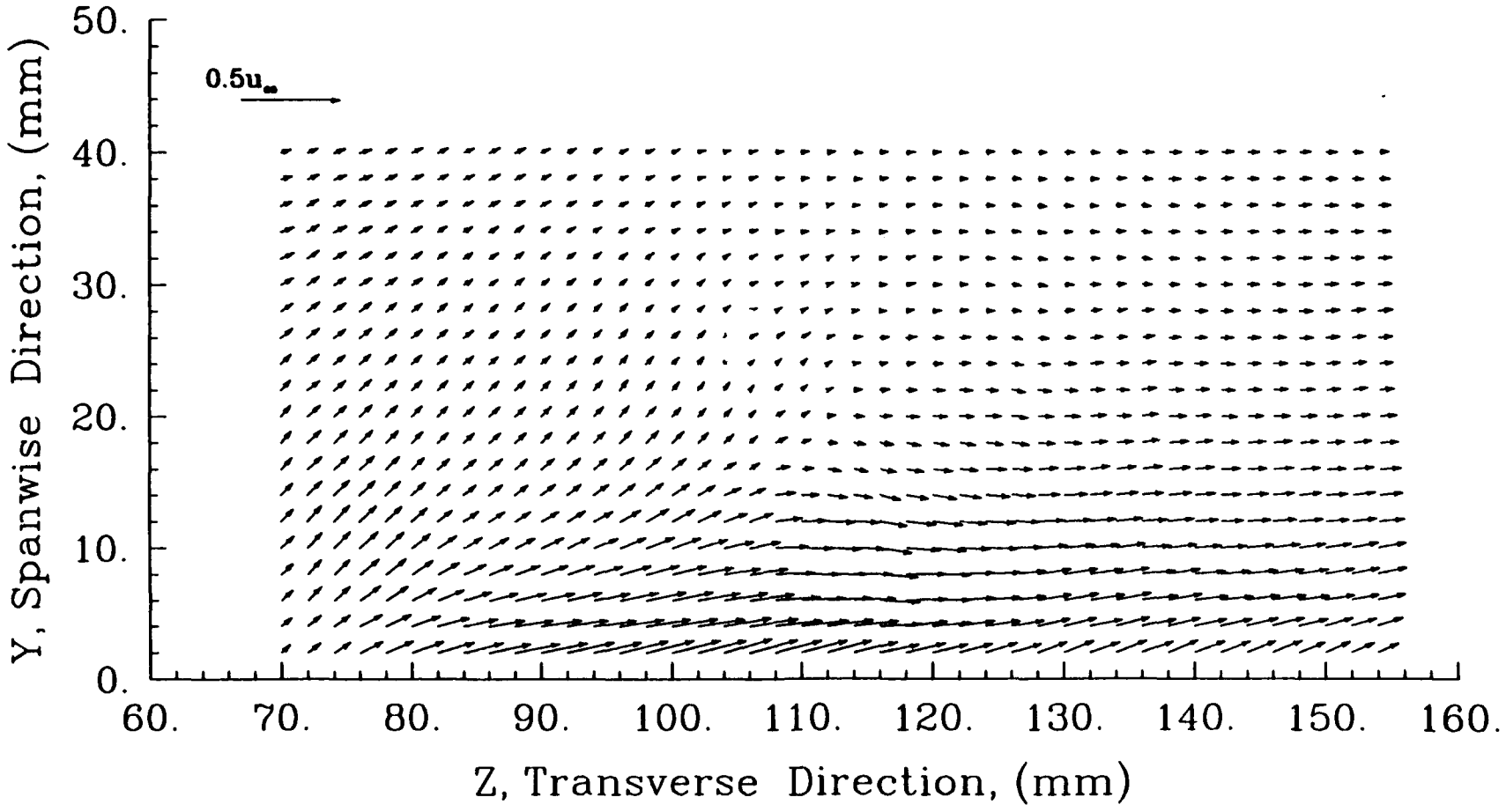

Figure 3.10 Filtered Secondary Flow Velocity Vectors for Experiment with: Solid Wall, Unmodified Geometry

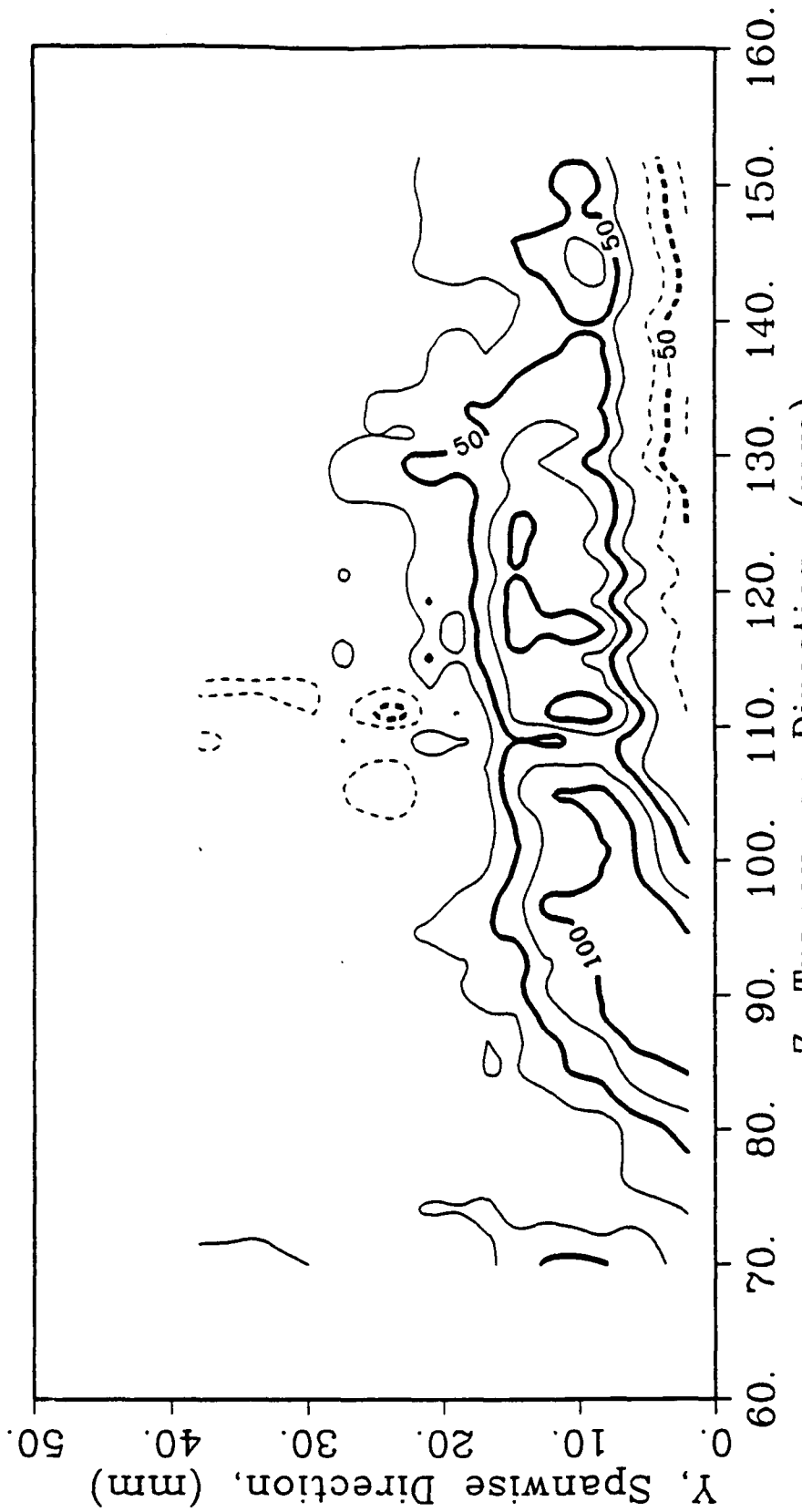

Figure 3.11 Streamwise Vorticity Contours for Experiment with: Solid Wall, Unmodified Geometry

which represents the expected maximum vorticity value at the vortex root. The fact that these two values are on the same order adds to the validity arguments of this investigation's experimental technique.

The spots of negative vorticity shown at approximately $Y = 25$ mm, and $Z = 110$ mm are most probably the secondary vortex system, discussed previously.

Utilizing the already calculated vorticity values, a net circulation can be found using Equation C.1.3. The summation operation was performed over the spatial range from $Y = 7.0$ mm to $Y = 27.0$ mm, and from $Z = 80.0$ mm to $Z = 150.0$ mm. The determined circulation provided a single value which summarized the measurements for an entire experiment. Since this quantity allows comparison of the results of different experiments, this spatial range of summation was used for all data sets. For the situation discussed above, the net circulation was determined to be $0.058\,\mathrm{m}^2/\mathrm{s}$.

3.2. Five-Hole Probe Measurements - Porous Walled Body

For this experiment the suction system described in Section 2.5 was installed in the wind tunnel, but with no suction power applied. The pump exhaust was taped over to eliminate any chance of a net flow through the suction system. Without this "stopper" in the system, the lower than ambient test section pressure would have drawn atmospheric air in through the pump.

The measured 99% boundary layer thickness was approximately 30 mm. The boundary layer displacement thickness was calculated to be $\delta^* \approx 9$ mm, and the momentum thickness was found to be $\theta \approx 5$ mm. These integral boundary layer values, measured with a porous wall segment installed in the wind tunnel, were larger than the previous solid wall results. This difference was due to the screens on the inside surface of the porous wall segment having a greater roughness than

the surrounding Plexiglas, and to the fact that the screening was not exactly flush with the Plexiglas surface of the adjacent wall segments.

The measured secondary flow velocity vectors are plotted in Figure 3.12, after fourier filtering. As in Figure 3.10, positive Y-flow near the surfaces and net positive Z-flow are observed. The flow turning seen previously seems to be much stronger in this experiment, when Figures 3.10 and 3.12 are compared. This difference is also illustrated in the vorticity contours of Figure 3.13. The horseshoe vortex structure was larger and stronger, as was the secondary vortex system. This disagreement was due to the greater vortical energy in the approaching boundary layer, as described above. The computed net circulation value for this experiment was $\Gamma = 0.086\,\mathrm{m}^2/\mathrm{s}$, which was 50% larger than the solid wall case.

In a more applications oriented installation, a smoother porous wall surface would need to be designed for maximum suction efficiency. But for the purpose of demonstrating the ability of suction to eliminate the horseshoe vortex, the existence of a larger and stronger vortex can only reinforce the arguments of this study.

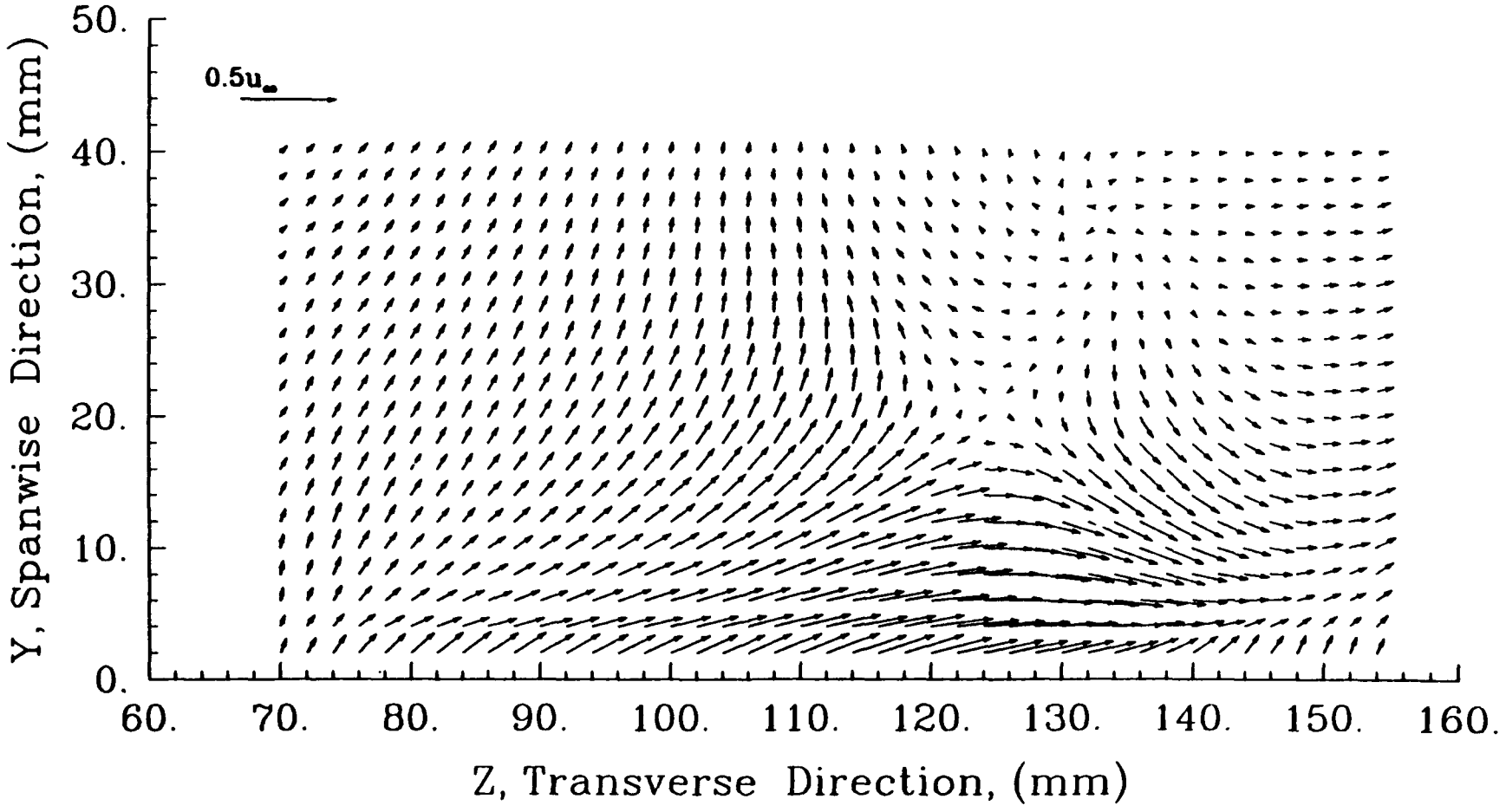

Figure 3.12 Filtered Secondary Flow Velocity Vectors for Experiment with: Porous Wall, No Suction ($Q_s = 0$)

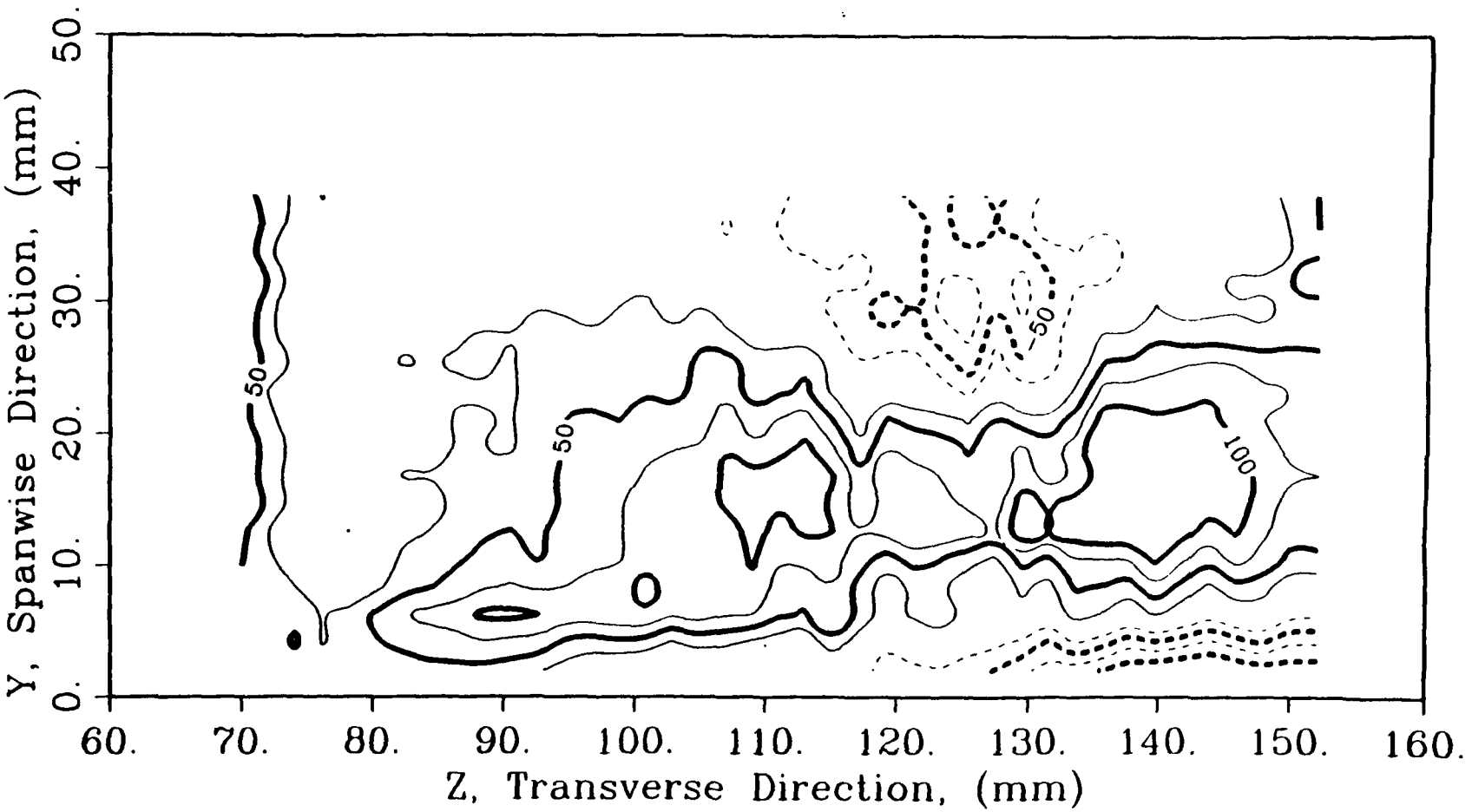

Figure 3.13 Streamwise Vorticity Contours for Experiment with: Porous Wall, No Suction ($Q_s = 0$)

Chapter 4

MODIFIED VORTEX RESULTS

4.1. Leading Edge Fairing

For the purpose of validating the experimental technique used, the general results of some other studies were reproduced in this investigation. The simplest passive method of reducing the horseshoe vortex strength has been to modify the wing nose geometry. For ease of fabrication, a new model was not constructed, but rather a two-dimensional leading edge fairing was fashioned for attachment onto the usual model. The resulting fairing is shown in Figures 4.1. An approximation of a cusped leading edge was the design intent, thereby reducing the leading edge radius as much as possible.

The usual solid wall of the wind tunnel was used in this experiment, so that all boundary layer data are the same as that acquired for the unmodified vortex solid wall experiment (see Section 3.2). A standard five-hole probe survey was performed, as described in Section 2.6. The filtered velocity vector data are presented in Figure 4.2. Very little flow turning can be observed by examination of this figure, as compared to the unmodified vortex velocity diagrams of Chapter 3. This initially implied that the strength of the horseshoe vortex had been successfully reduced.

Vorticity contours were generated from the velocity data and are shown in Figure 4.3. The region of concentrated vorticity does seem somewhat smaller than the corresponding unmodified vortex vorticity contours of Figure 3.11. Also, the secondary vortices are nearly eliminated. The calculated net circulation for this fairing experiment is $\Gamma = 0.047\,\mathrm{m}^2/\mathrm{s}$. Thus a 20% reduction in Γ has been achieved

(a) (b)

Figure 4.1 (a) Leading Edge Fairing
(b) Wing Model with Fairing in Place

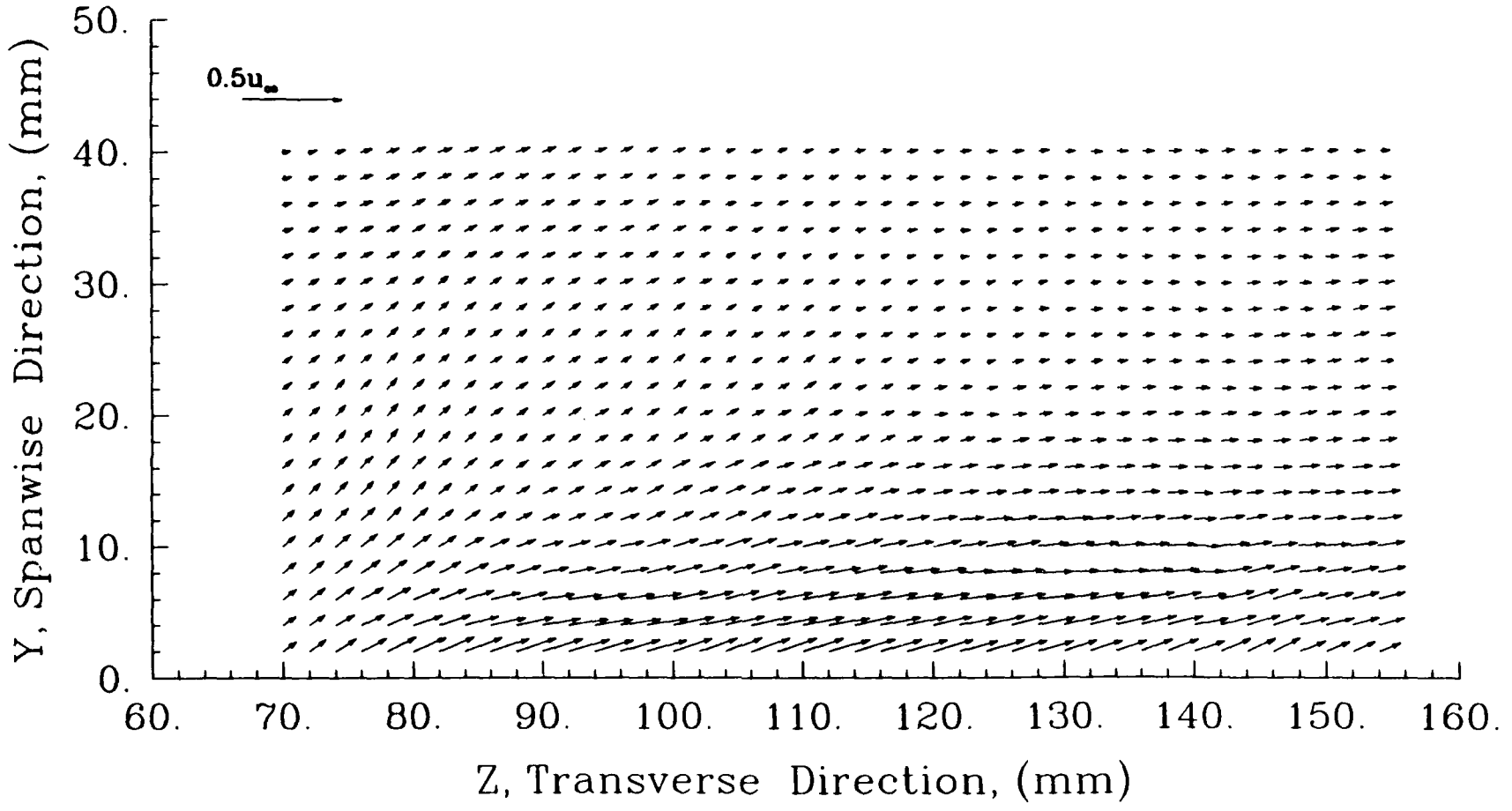

Figure 4.2 Filtered Secondary Flow Velocity Vectors for Experiment with: Solid Wall, Fairing in Place

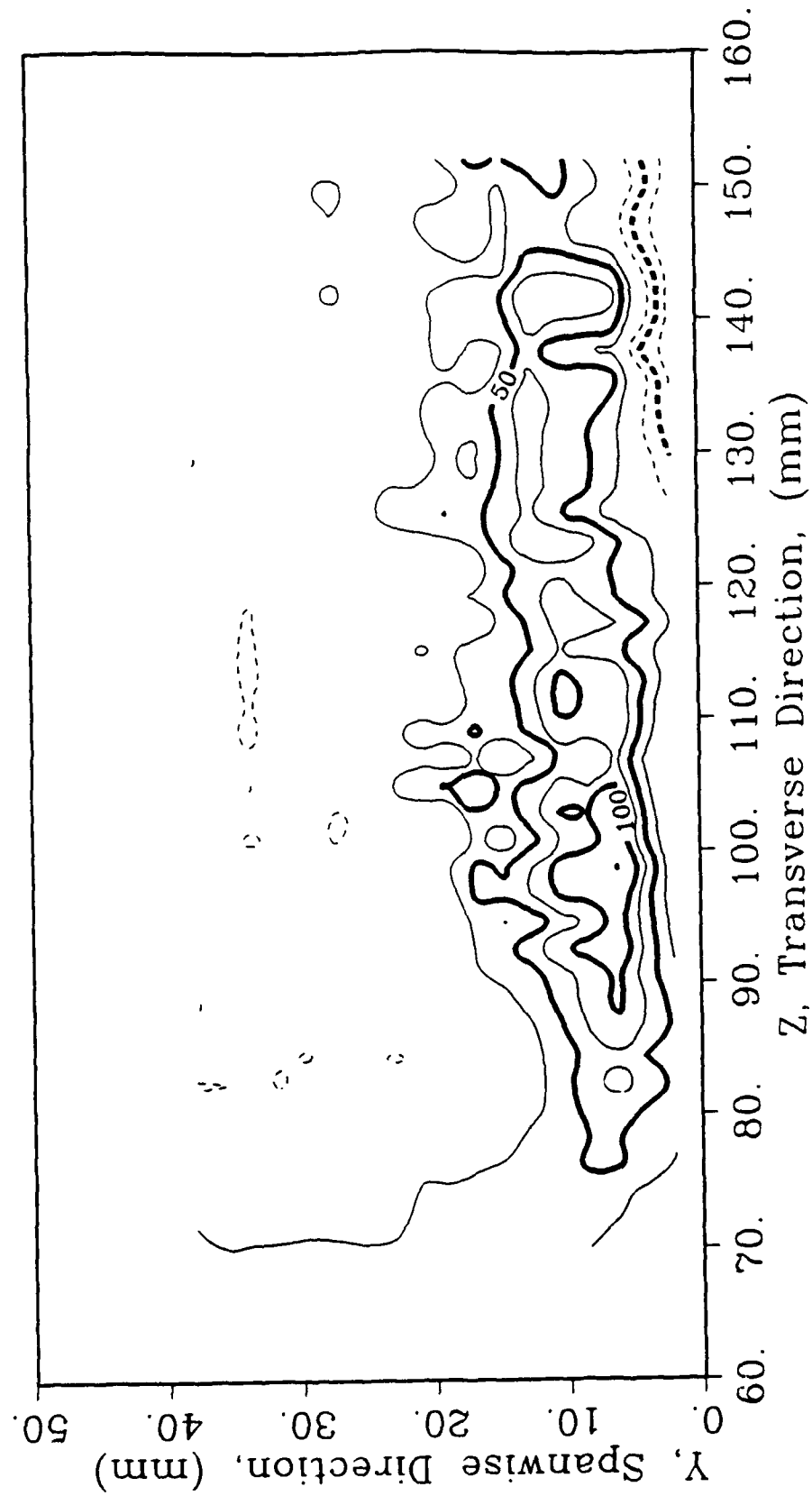

Figure 4.3 Streamwise Vorticity Contours for Experiment with: Solid Wall, Fairing in Place

utilizing this passive approach of geometry modification.

Of the previous investigations discussed in Section 1.2, the wing geometries used in Mehta's 1984 study are the most similar to the one used here because of the two-dimensional configurations. But such a comparison cannot be considered too accurate because the leading edges used were of different designs. It was found, though, that the circulation reduction in this experiment does agree quite well with Mehta's 1984 results (note also that he used a different circulation definition).

The cusped edge of the fairing used here presumably nearly eliminated $\frac{\partial W}{\partial X}$ at the leading edge, but its high curvature just downstream of the cusp probably introduced a high lateral divergence into the flow (see discussion in Section 1.1). Therefore, greater circulation reductions could be achieved by more careful design of the entire forward portion of the wing.

4.2. Suction Experiments

For the experiments of this section, the suction system and porous wall segment were installed in the wind tunnel. Various suction volumetric flow rates were applied to remove the boundary layer and its bound vorticity from the flow field.

The porous section in the wind tunnel wall through which the suction was applied was 150 mm wide (in the Z-direction). The volumetric flow rate through a control volume enclosing the solid wall boundary layer, and being as wide as this porous section was calculated to be $Q_{bl} \approx 0.026\,\mathrm{m}^3/\mathrm{s}$ (see Section 3.2). If the suction could be applied with 100% efficiency, Q_{bl} would be the minimum required flow rate to remove the entire boundary layer. Therefore this is a reference volumetric flow rate, to allow nondimensionalization of suction volumetric flow rates.

Example near wall velocity profiles, with and without suction applied, are given in Figure 4.4; both of these experiments were performed with the porous wall

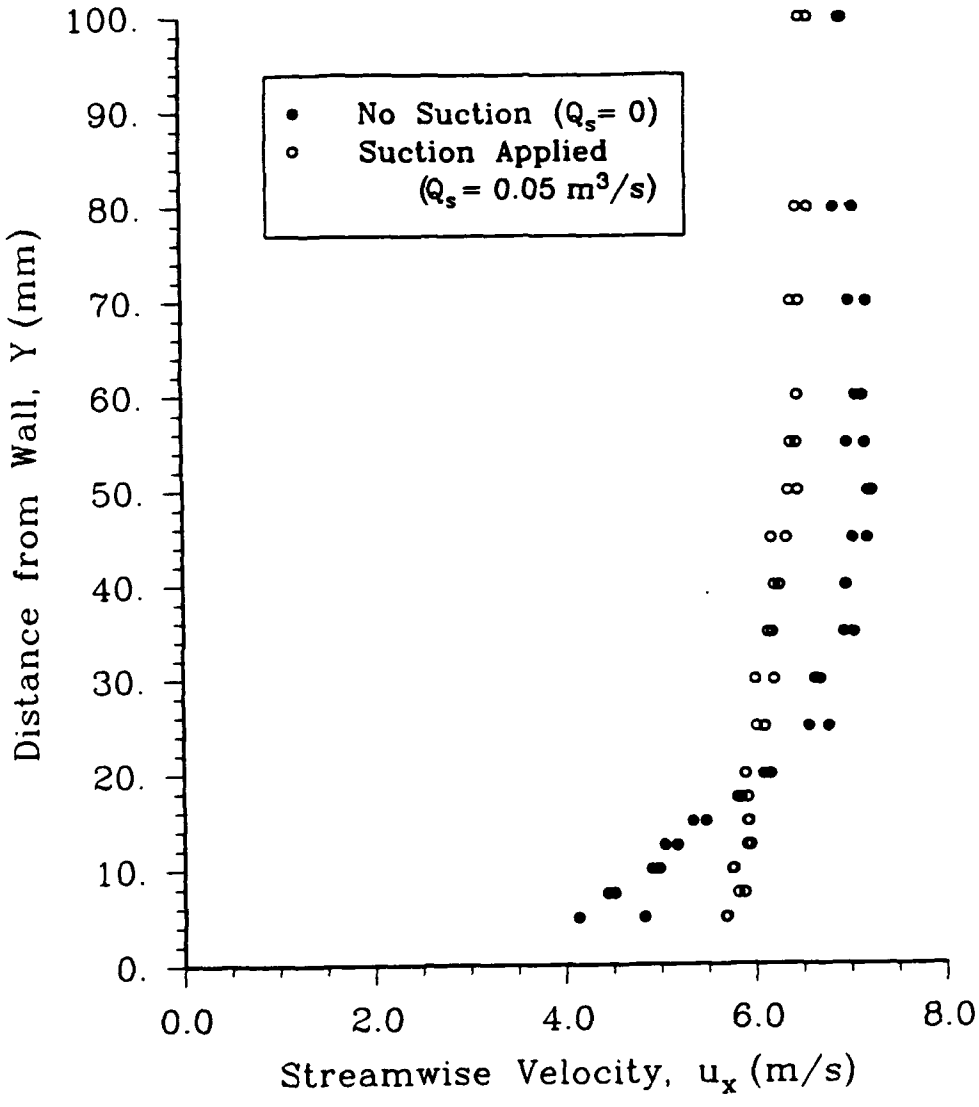

Figure 4.4 Example Boundary Layer Surveys Illustrating the Effect of Suction

segment installed. A concentrated region of viscous activity was not discernable for the case with suction applied; however, a small and nearly constant velocity gradient was measured. This affected the flow quite far from the wall surface.

This observation can be reconciled by the fact that the application of suction at the wind tunnel wall removes fluid from the test section. Therefore, air from the freestream must expand to fill that void. This expansion requires a decrease in fluid velocity to satisfy the incompressible continuity equation. Thus, near wall velocity decreases are largely pressure driven, and not friction driven as in the case of a boundary layer.

Of course, very close to the surface a boundary layer must exist, but this level of near-wall detail is not measurable with a five-hole probe. Because a definitive boundary layer was not measured when suction was applied, boundary layer quantities (i.e. δ_{99}, δ^*, and θ) will not be reported.

The first suction experiment involved the application of a suction volumetric flow rate of $Q_s \approx 0.03\,\mathrm{m}^3/\mathrm{s}$. This corresponded to a nondimensional volumetric flow rate of:

$$Q^* = \frac{Q_s}{Q_{bl}} \approx 1.2\,. \tag{4.2.1}$$

The orifice attachment was connected to the pump exhaust to achieve this small volumetric flow rate. Specifically, the pump power controller was set on low, and an orifice plate with a hole diameter of 38 mm was used.

The resulting velocity vector plot for this experiment is presented in Figure 4.5. As with the leading edge fairing experiment, the flow turning associated with the horseshoe vortex is not visually apparent. But the vorticity contour plot shows that the vortex structure still exists, although greatly diminished in size and strength (see Figure 4.6). Even at this level of suction, the results are more pronounced than with the fairing. For this experiment, the net circulation was computed to

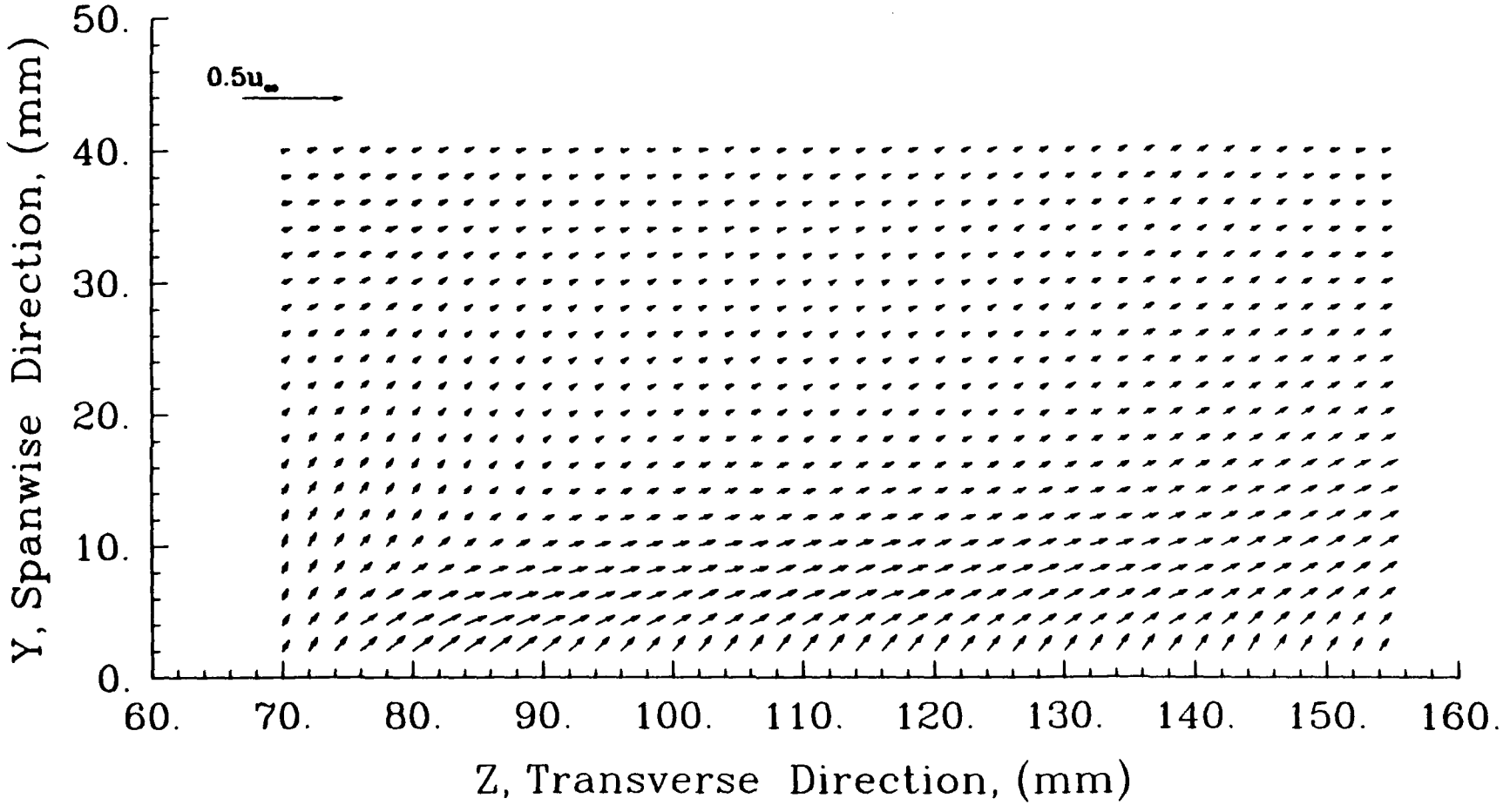

Figure 4.5 Filtered Secondary Flow Velocity Vectors for Experiment with: Porous Wall, Suction Applied $Q_s = 0.03 m^3/s$

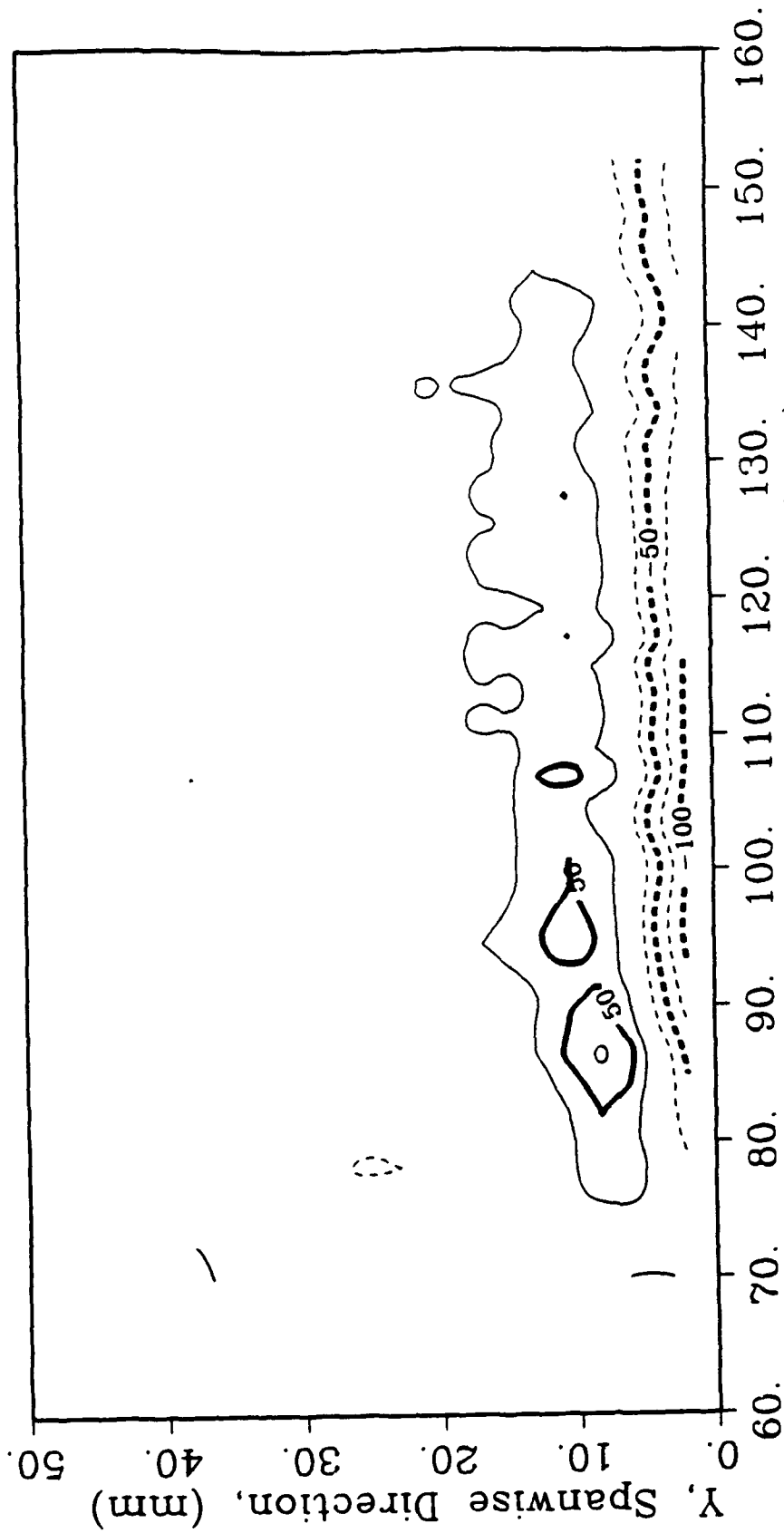

Figure 4.6 Streamwise Vorticity Contours for Experiment with: Porous Wall, Suction Applied $Q_s = 0.03\ m^3/s$

be $0.025\,\mathrm{m}^2/\mathrm{s}$; this corresponds to a 57% decrease in Γ compared to the no-fairing, solid wall experiment, and a 71% decrease compared to the no-suction porous wall experiment.

In the next experiment a suction volumetric flow rate of $Q_s \approx 0.04\,\mathrm{m}^3/\mathrm{s}$ ($Q^* \approx 1.5$) was applied. This volumetric flow rate was achieved by again setting the pump power controller on low, and using an orifice plate with an orifice diameter of 51 mm. The filtered velocity vectors and resulting vorticity contours are shown in Figures 4.7 and 4.8, respectively. It is clearly seen that the horseshoe vortex has been reduced in size and strength compared to the previous experiment. The calculated net circulation is $\Gamma = 0.018\,\mathrm{m}^2/\mathrm{s}$; 69% less than in the no-fairing, solid wall experiment, and 79% less than in the no-suction porous wall experiment. This is only a modest decrease in the vortex strength from the $Q^* \approx 1.2$ case.

The results of an experiment with $Q_s \approx 0.05\,\mathrm{m}^3/\mathrm{s}$ ($Q^* \approx 1.9$) applied are shown in Figures 4.9 and 4.10. This suction level was produced by setting the pump power controller on low, and using no orifice plate. No horseshoe vortex is discernable in either the velocity vector plot or in the vorticity contour plot, for $Q^* \approx 1.9$. The net circulation calculated for this experiment's flow field is $0.014\,\mathrm{m}^2/\mathrm{s}$. The reason for this value of Γ being nonzero seems to be the vortical structures occurring in the vicinity of $Y = 10$ mm, $Z = 140$ mm in Figure 4.10. With some hindsight, a similar but weaker structure can be observed in the previous experiment (see Figure 4.8). The position of these structures implies that their origin was very likely the edge of the suction hole parallel to the X-axis. This can be shown by adding half the wing thickness to half the suction hole width, yielding a sum of 145 mm. This value is quite similar to the already observed Z-location of the vortical structures.

What probably occurred is that regions with high transverse gradients of spanwise velocity were setup at the edges of the suction hole, because of the

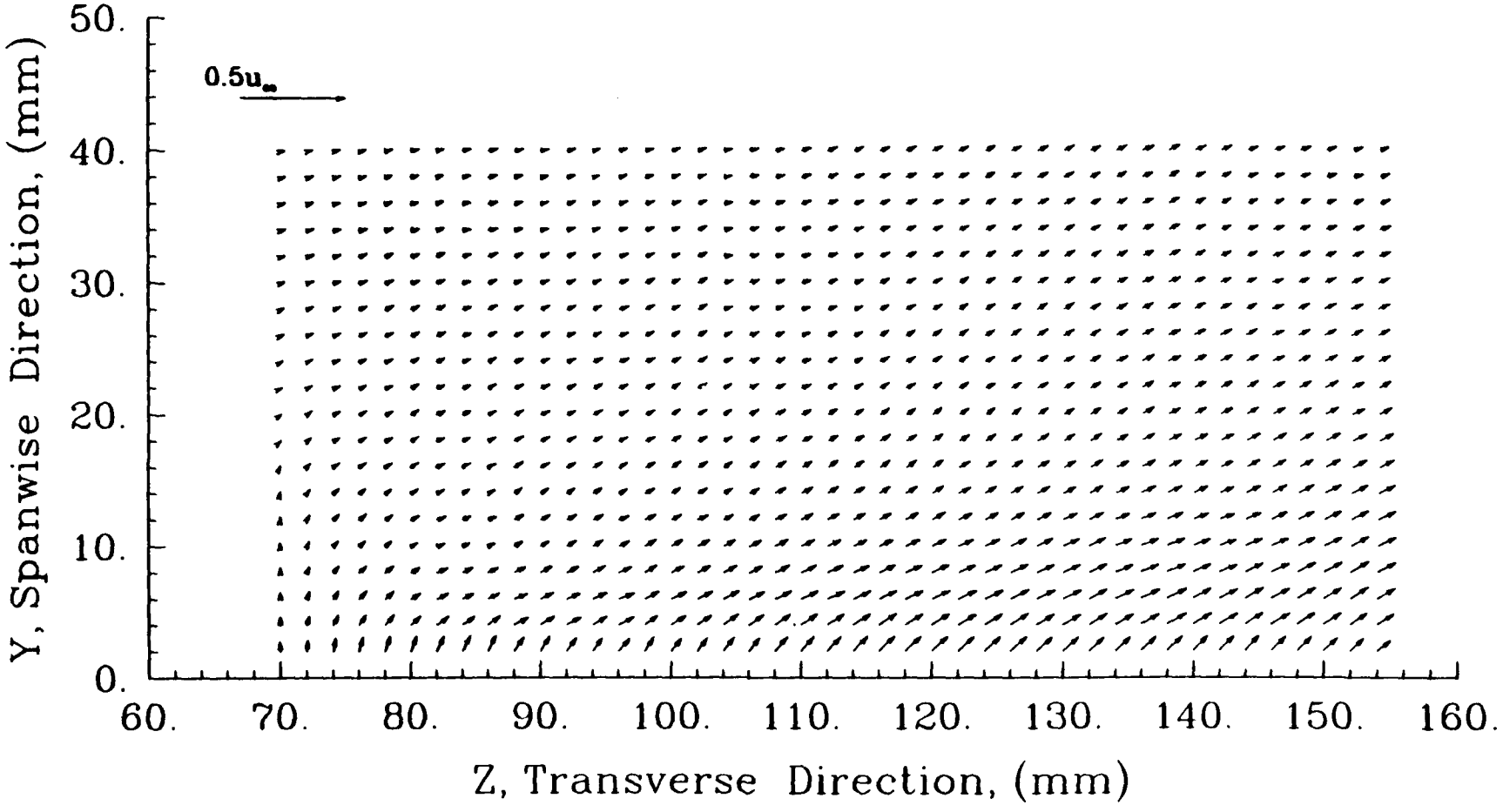

Figure 4.7 Filtered Secondary Flow Velocity Vectors for Experiment with: Porous Wall, Suction Applied Q_s= 0.04 m^3/s

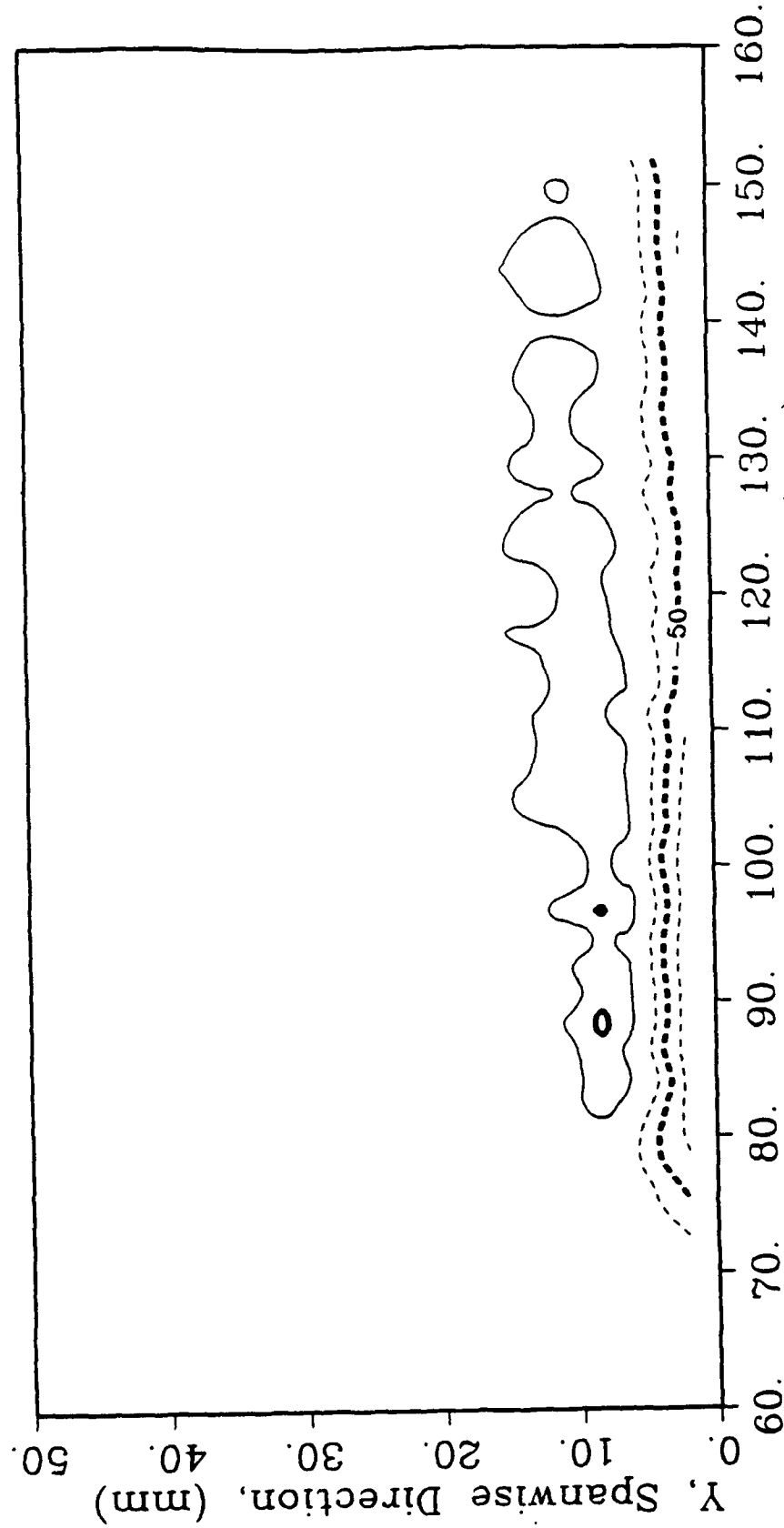

Figure 4.8 *Streamwise Vorticity Contours for Experiment with:* **Porous Wall, Suction Applied $Q_s = 0.04\ m^3/s$**

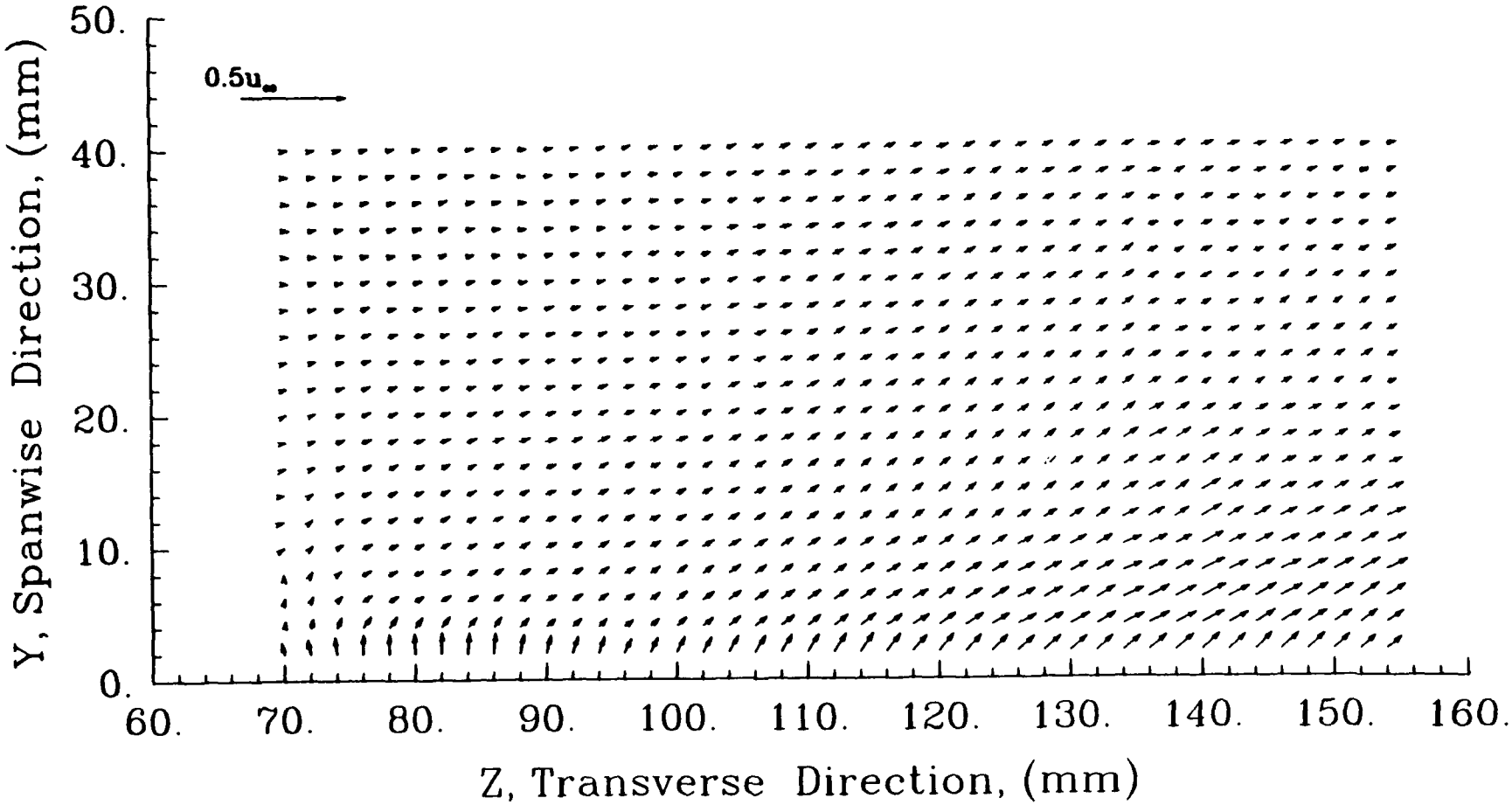

Figure 4.9 Filtered Secondary Flow Velocity Vectors for Experiment with: Porous Wall, Suction Applied Q_s= 0.05 m^3/s

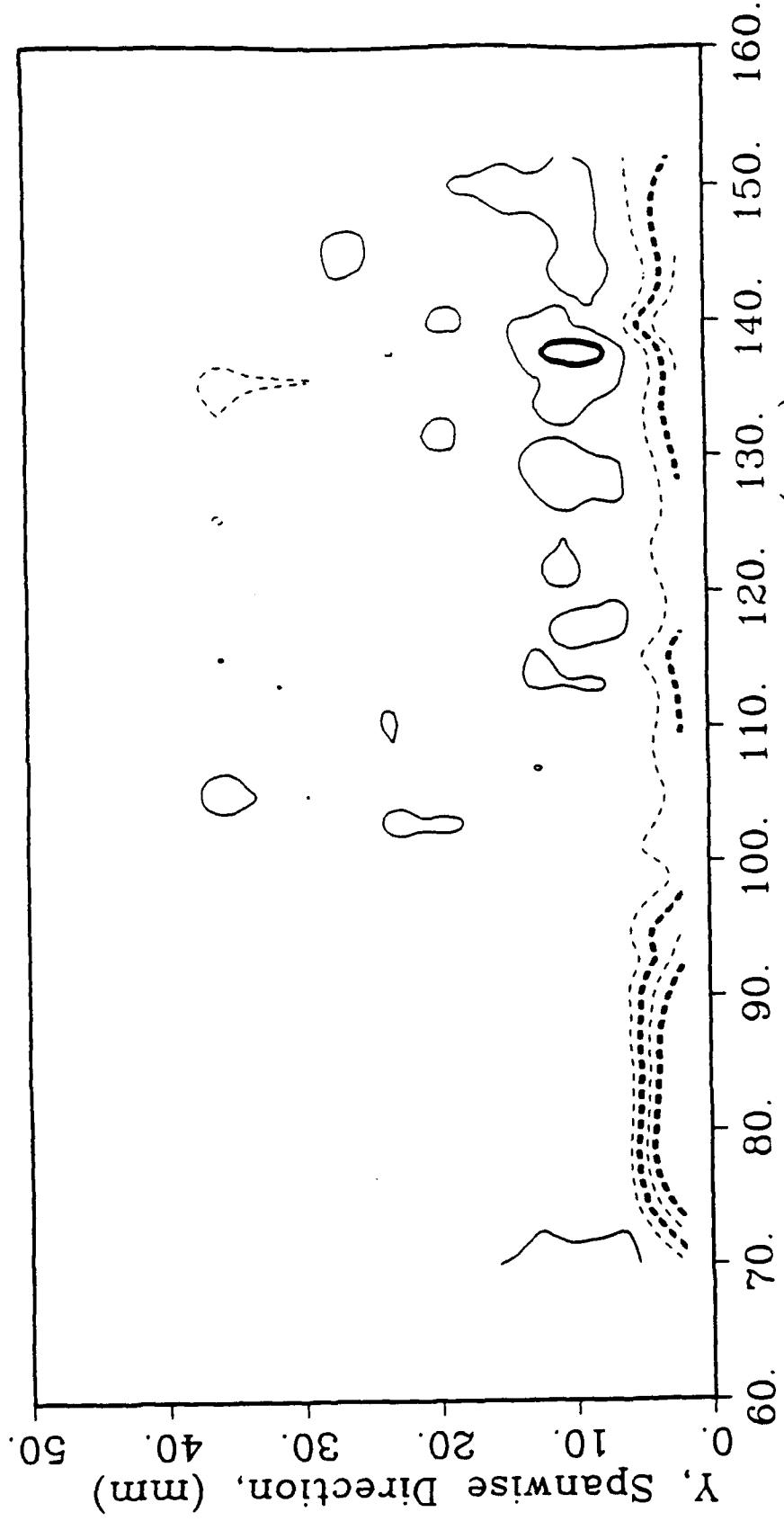

Figure 4.10 Streamwise Vorticity Contours for Experiment with: Porous Wall, Suction Applied Q_s= 0.05 m^3/s

interface between the normal flow (with a boundary layer) and the suction flow (boundary layer removed). The normal flow in a boundary layer had a small positive Y-velocity component due to boundary layer displacement effects. In the region of the suction hole, a negative Y-velocity component existed, as the boundary layer was being removed from the test section. These effects produced a velocity gradient appropriate for generating a positive streamwise vorticity, which was then convected downstream.

Because the negative Y-velocity produced by the suction was the source for these vortical spots, one expects that the greater the suction volumetric flow rate which is applied, the greater the vorticity generated will be. This postulation is supported by Figures 4.8 and 4.10. It is further supported by the results of an experiment performed with an even higher value of Q_s.

By setting the pump power on high, with no orifice attachment used, an experiment with $Q_s \approx 0.09\,\mathrm{m}^3/\mathrm{s}$ ($Q^* \approx 3.5$) was performed. The results are given in Figures 4.11 and 4.12. The vorticity plot shows no coherent horseshoe vortex, but does display more incoherent spots of vorticity than seen in experiments with smaller values of Q^*. A net circulation of $\Gamma = 0.015\,\mathrm{m}^2/\mathrm{s}$ was computed, which is actually larger than the previous experiment with a smaller Q^*. These observations reinforce the conjectures discussed above.

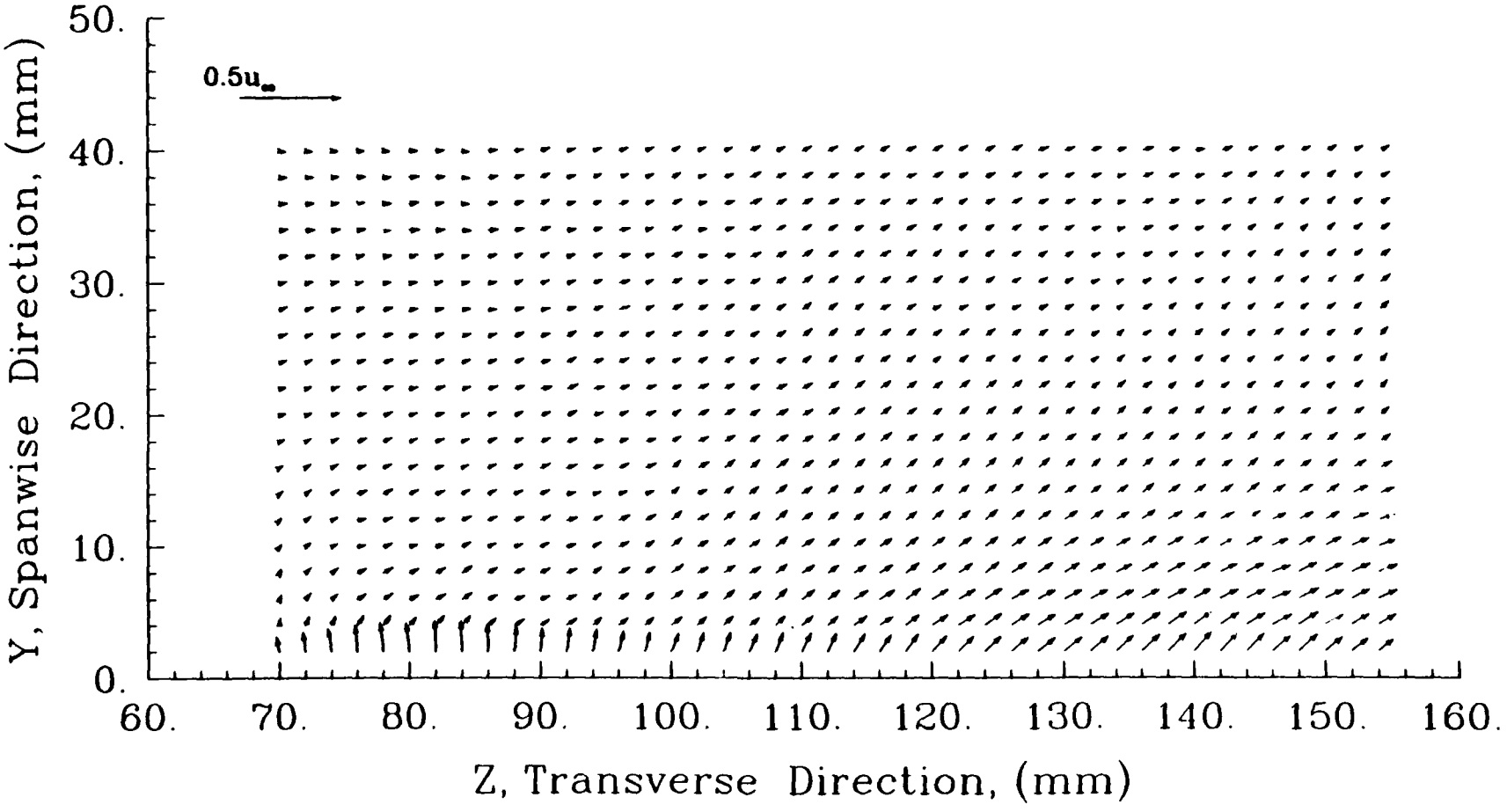

Figure 4.11 Filtered Secondary Flow Velocity Vectors for Experiment with: Porous Wall, Suction Applied $Q_s = 0.09\ m^3/s$

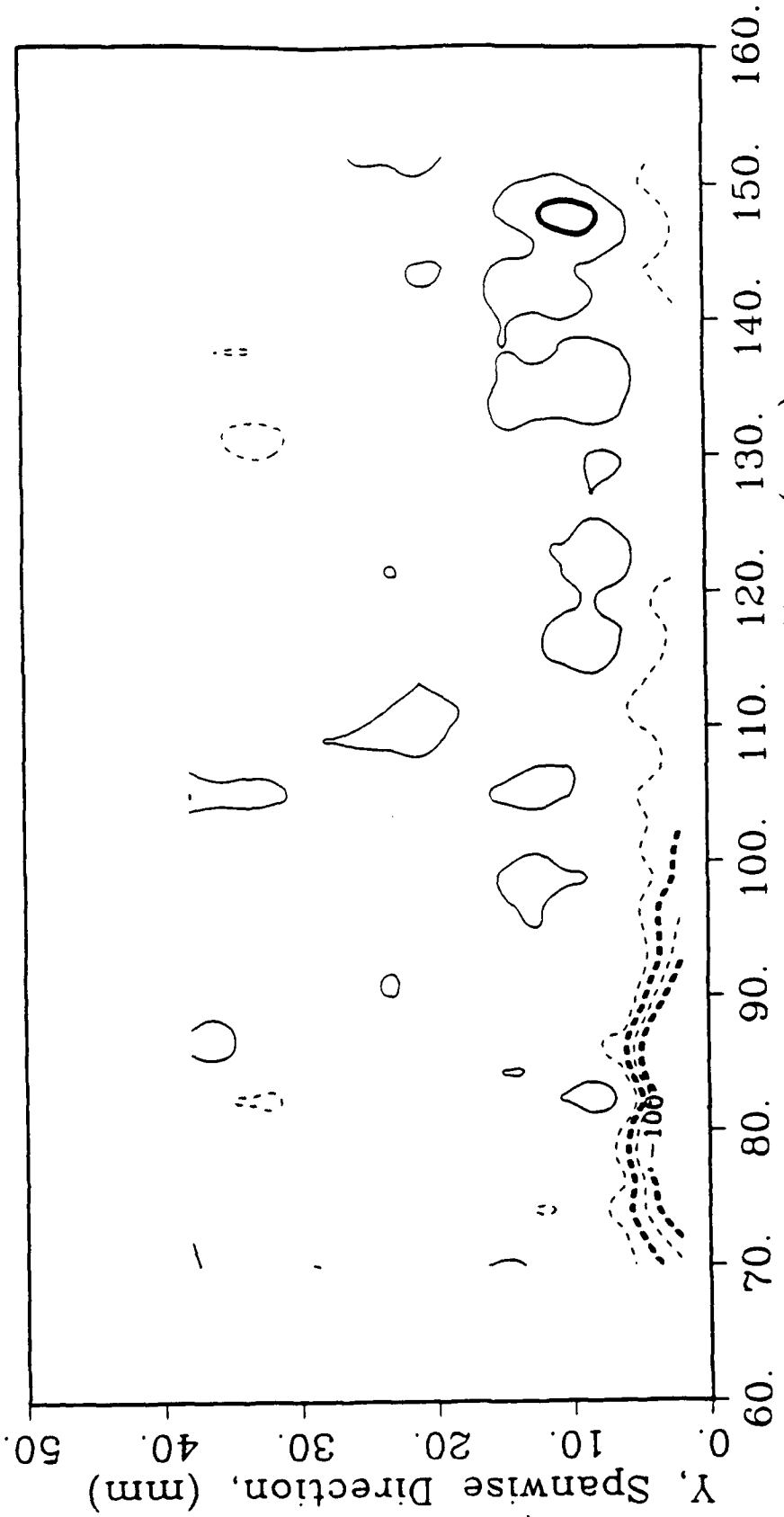

Figure 4.12 Streamwise Vorticity Contours for Experiment with: Porous Wall, Suction Applied $Q_s = 0.09\ m^3/s$

Chapter 5

DISCUSSION AND CONCLUSIONS

An experimental study of the steady state nature of the wing-body junction vortex and methods of reducing its effects on the flow field has been performed. Two specific methods of achieving this reduction were implemented experimentally. The first was the passive approach of wing geometry modification. The second was the active approach of boundary layer suction on the body surface.

The unmodified vortex was examined qualitatively utilizing smoke-wire flow visualization, and some quantitative data were obtained from these photographs as well. The results of these experiments showed for the present experimental setup that the horseshoe vortex root was approximately 10 mm in diameter and independent of freestream velocity. This implies that the vortex size at flow visualization wind speeds should be quite similar to that measured at the higher wind speeds used in the five-hole probe surveys.

From a five-hole probe survey in the solid wall, unmodified vortex experiment, the spanwise height of the concentrated region of vorticity was about 15 mm. This agrees well with the previously stated flow visualization results, particularly when the effect of diffusion is considered. The observed large transverse size of the vortex was presumably due to the shear forces that turned the vortex into the streamwise direction.

The height of the vortex was in the range of twice to four times the size of the approaching boundary layer displacement thickness. This result was shown in both the solid wall experiment and in the porous wall experiment without suction.

The installation of a cusped fairing on the wing model nose successfully reduced the vortex strength by about 20%; this value agrees well with the findings of previous studies. Based upon this result, as well as the qualitative agreement of the flow visualization and five-hole probe studies, the experimental technique appears to have been sound.

The application of suction to actively reduce/eliminate the horseshoe vortex was investigated at various suction volumetric flow rates. These included $30\,m^3/s$, $40\,m^3/s$, $50\,m^3/s$ and $90\,m^3/s$; nondimensionalizing by the solid wall boundary layer volumetric flow rate, these values corresponded to 1.2, 1.5, 1.9, and 3.5, respectively. Theoretically, if the porous wall had been designed perfectly, a nondimensional flow rate of 1.0 would be required to eliminate the boundary layer and thus the horseshoe vortex.

Using net circulation as a measure of vortex strength, the results of this study are illustrated in Figure 5.1. From this figure and the observations noted throughout this report some conclusions can be stated as follows:

1. The horseshoe vortex structure can be eliminated from a flow field by removing the upstream boundary layer which acts as a vorticity source. This active technique of boundary layer suction was far more successful than known passive techniques.
2. For the present experimental setup a nondimensional volumetric flow rate of about 1.9 was required to suppress the vortex generation. The deviation of this value from unity represents the inefficiency in the suction hole design.
3. The streamwise edges of the rectangular suction hole used here acted as a vorticity source, thus making it impossible to reduce the circulation to zero. Furthermore, more vorticity was produced at larger suction flow rates.
4. From items 2 and 3 it can be deduced that a particular suction volumetric

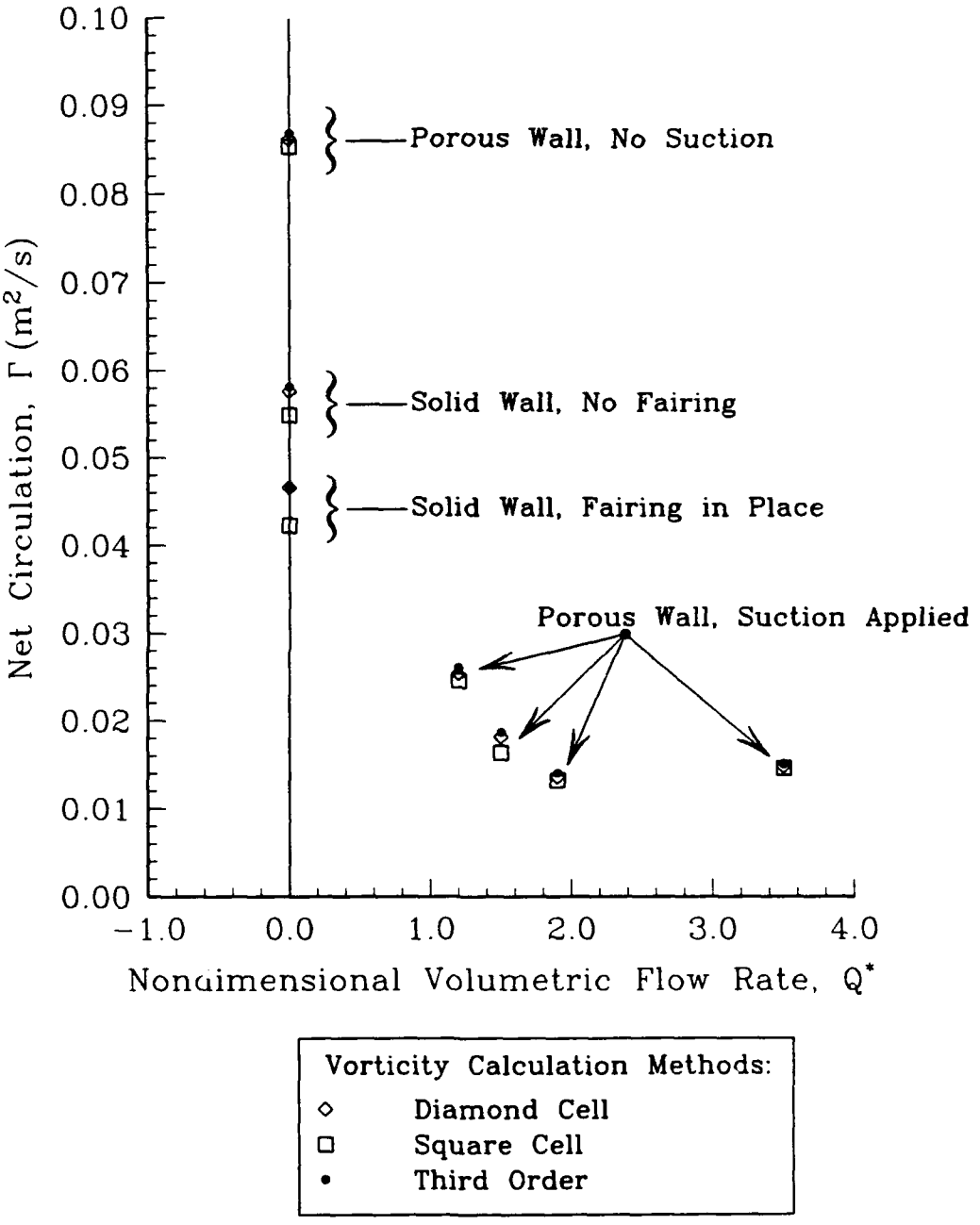

Figure 5.1 Net Circulation for Each Experimental Situation

flow rate must exist at which the value of Γ has a minimum. This can also be seen by the parabolic nature of the porous wall data shown in Figure 5.1. The parabola's minimum will depend on the suction hole design.

A horseshoe vortex with a diameter in the vicinity of 2 mm could still exist in the higher suction flow rate experiments, even though it is not observable in the vorticity contour plots. This is because the no-slip condition requires a boundary layer, however small, to exist on the simulated body surface. Therefore a small and concentrated wing-body junction vortex could have developed. But because this small boundary layer developed in a region where the flow is nearly stagnated, the small scale vortex would be weaker than normally expected. A small and fairly weak vortex would have little effect on the flow field, so the ability of suction to eliminate the *large* scale vortex is still important.

Further studies will need to be performed to address some of the concerns stemming from the above conclusions as well as other issues more applications oriented in nature. The following are recommendations for future investigations:

1. More efficient suction holes can be designed to approach the ideal value of $Q^* = 1.0$ and to reduce the suction hole edge vorticity production. The study performed by Goldsmith (1961) on laminar flow control at a wing-body junction may give some guidance for future work.
2. The possibility of early separation off the wing when the approaching boundary layer is removed needs to be studied on a complete airfoil model; this problem was observed by Barber (1978). If early separation is found to be a problem, trailing edge wing fairings near the body surface may prove to be useful (see the 1988 study of Sung and Lin).
3. The effect of different operating conditions encountered for a particular application, such as varying Reynolds numbers, needs investigation. Any

required suction power adjustment could be easily accomodated, but if the suction hole design must be different, then mechanical complications would be introduced.

In conclusion, it has been successfully shown that the application of suction to the approaching boundary layer can reduce and even eliminate the horseshoe vortex structure. This approach was shown to be capable of a more complete suppression of the horseshoe vortex than known passive systems. Further research and development must be performed to determine the most efficient method of applying the suction, as well as determining the effect of varying operating conditions.

REFERENCES

Barber, T.J., "An Investigation of Strut-Wall Intersection Losses," J. Aircraft, Vol. 15, No. 10, 1978, pp. 676-681

Devenport, W.J., Dewitz, M.B., Agarwal, N.K., Simpson, R.L. and Poddar, K., "Effects of a Fillet on the Flow Past a Wing Body Junction," AIAA Paper 89-0986, 2nd Shear-Flow Control Conference, Tempe, AZ, 1989

Dickinson, S.C., "Flow Visualization and Velocity Measurements in the Seperated Region of an Appendage-Flat Plate Junction," DTNSRDC Report 86/020, March 1986

Dickinson, S.C., "An Experimental Investigation of Appendage-Flat Plate Junction Flow. Volume I: Description," DTNSRDC Report 86/051, December 1986

Goldsmith, J., "Laminar Flow at the Juncture of Two Aeroplane Components," Boundary Layer and Flow Control, Vol. 2, 1961, pp. 1000-1006

Kubendran, L.R., Bar-Sevar, A. and Harvey, W.D., "Flow Control in a Wing/Fuselage-Type Juncture," AIAA Paper 88-0614, 26th Aerospace Sciences Meeting, January 1988

Mehta, R.D., "Effect of Wing Nose Shape on the Flow in a Wing/Body Junction," Aeronautical J., Vol. 88, December 1984, pp. 456-460

Press, W.H., Flannery, B.P., Teukolsky, S.A., and Vetterling, W.T., "Numerical Recipes, The Art of Scientific Computing," Cambridge University Press, 1986

Sung, C.H. and Lin, C.W., "Numerical Investigation on the Effect of Fairing on the Vortex Flows around Airfoil/Flat-Plate Junctures," AIAA Paper 88-0615, 26th Aerospace Sciences Meeting, January 1988

Treaster, A.L. and Yocum, A.M., "The Calibration and Application of Five-Hole Probes," ISA Transactions, Vol. 18, No. 3, 1979, pp. 23-34

Appendix A

FIVE-HOLE PROBES IN APPLICATIONS WITH LOW DYNAMIC PRESSURES

A.1. Background

Velocity measurements in three-dimensional steady-state flow fields are often required. Five-hole probe systems have advantages over other three-dimensional anemometry systems that make them desirable for certain applications. These probes are capable of spatial resolutions down to about 1.5 mm (slightly less than their tip diameter); this is usually not attainable with three wire hot-wire systems. And laser doppler velocimeter's inherent complications of seed injection and optics alignment are totally avoided.

The use of five-hole probes classically requires the painstaking process of nulling, sometimes impossible due to space limitations. But the 1978 paper of Treaster and Yocum presented a new technique for utilizing five-hole probes in a non-nulling mode. This approach requires a calibration to be performed for each probe used. The geometry of the type of five-hole probe used in this study is shown in Figure A.1.

Treaster and Yocum's calibration scheme instructs the user to mount the five-hole probe in a uniform flow, on a pitch-yaw device. In this manner, the angularity of the flow relative to the probe tip axis can be varied. The relative flow angles are referred to as the pitch angle, α, and the yaw angle β. Total and static pressures at the probe tip are needed as well; these can be supplied by installing a pitot-static probe near the five-hole probe.

The pitch-yaw device is oriented to seven values of α and seven values of β,

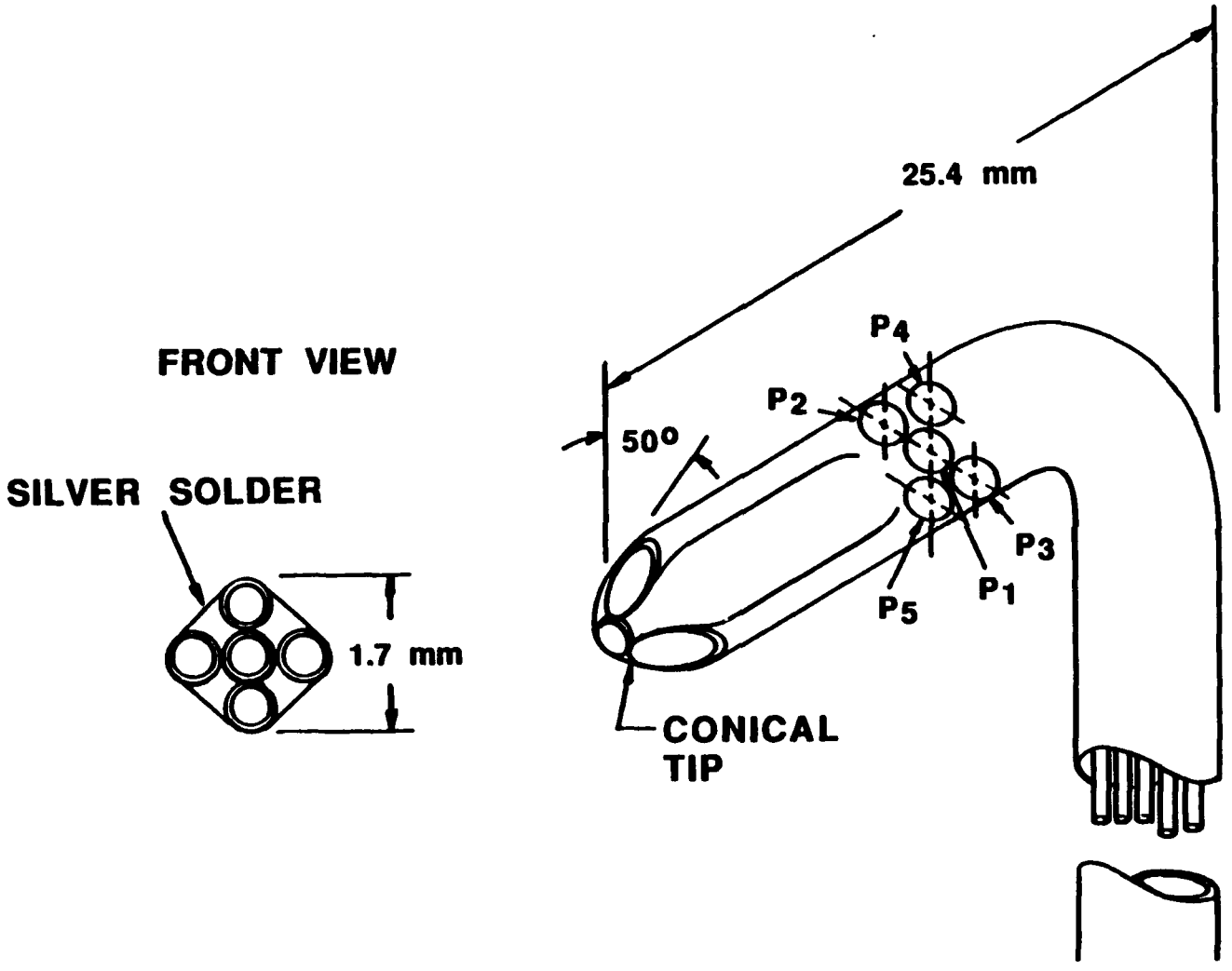

Figure A.1 Five-Hole Probe Geometry, Showing Hole Assignments
(Not Drawn to Scale)

thus making a calibration grid of 49 points. At each of these points, seven pressures are measured: P_1, P_2, P_3, P_4, P_5, (pressures at each of the five-hole probe's holes), P_{total}, and P_{static}. Usually, these pressures are measured as a differential pressure with respect to some constant reference pressure (for most applications, atmospheric pressure).

The seven pressures are combined to yield the following four calibration coefficients:

$$C_{P_{yaw}} = \frac{(P_2 - P_3)}{(P_1 - \overline{P})}, \tag{A.1.1}$$

$$C_{P_{pitch}} = \frac{(P_4 - P_5)}{(P_1 - \overline{P})}, \tag{A.1.2}$$

$$C_{P_{total}} = \frac{(P_1 - P_{total})}{(P_1 - \overline{P})}, \text{and} \tag{A.1.3}$$

$$C_{P_{static}} = \frac{(\overline{P} - P_{static})}{(P_1 - \overline{P})}, \tag{A.1.4}$$

$$\text{where} \quad \overline{P} = \frac{(P_2 + P_3 + P_4 + P_5)}{4}. \tag{A.1.5}$$

The calibration data set is a record of 49 of each of the four pressure coefficients defined above.

In utilizing a five-hole probe to measure an unknown flow field, the five pressures at the probe tip are measured, and $C_{P_{yaw}}$ and $C_{P_{pitch}}$ are calculated. Via a spline fit of the calibration data, the flow angles α and β can then be interpolated. Thus, knowing α and β, $C_{P_{total}}$ and $C_{P_{static}}$ can be calculated, again using interpolation from a spline fit of the calibration data. Then from the total and static pressure coefficients, Equations A.1.3 and A.1.4 can be solved for the total and static pressure values. The velocity magnitude can then be calculated from Bernoulli's equation. From the velocity magnitude and the relative flow angles, the three components of velocity are determined.

Corrections for large variations in Reynolds number and close proximity to a

wall are sometimes needed. These concerns are addressed in the Treaster and Yocum paper referenced above.

A.2. Low Dynamic Pressure Concerns

The obvious requirement in applying a five-hole probe system accurately is the need for accurate pressure measurements. When performing studies with water as the medium, or with air above about 20 m/s, this does not present a problem. Inexpensive pressure transducers with sufficient range and accuracy are commercially available. But in systems operating in low speed air, where the dynamic pressures are quite small, obtaining the required accuracy becomes a primary concern.

Appropriate transducers are of course available, for example the 1 mm Hg full scale MKS Baratron system described in Section 2.3. But these transducers are costly, and many laboratories cannot afford the cost of purchasing five or more of these. Thus a Scanivalve system must be used to port each of the pressure lines individually to the transducer. Such a configuration is shown schematically in Figure 2.3 and briefly described in Section 2.3.

This setup introduces another concern. A settling time is required after each pressure line is ported to the transducer to allow pressure equilization between the pressure source (e.g. a probe tip) and the transducer's diaphragm. The settling time depends on too many factors to use a simple delay loop in the computer software (unless the delay loop is very long, which can waste a lot of time). A few methods for determining the end of the settling period were explored, and a fairly simple one was found to be the best.

The approach specifies that the data acquisition system reads in N pressure data points from the signal conditioner (where $20 \tilde{<} N \tilde{<} 30$). The standard deviation of

this set is determined and if the standard deviation is greater than some tolerance, it is assumed that this indicates an unequilized pressure. If so, three more pressure data points are read which replace the first three of the N pressure points. In this way, the first three data points are repeatedly replaced by new ones until the standard deviation of the set is determined to be less than the tolerance. Finally the mean of the latest set of pressure points is returned as the measured pressure.

Selection of the standard deviation tolerance level depends mostly on the magnitude of the dynamic pressure in the particular application and the ability of the system to maintain steadiness. No general criterion can easily be specified.

As stated, accurate measurement of pressure is a prerequisite to accurate application of a five-hole probe system. The communication of these values to the data acquisition system should also be examined. If the transducer outputs an analog voltage, a minimum 16-bit analog-to-digital (A/D) conversion is best. If available, using digital output may prove to be the more accurate approach. Digital data transmission will probably require many digital input ports on the data acquisition system, but these are less costly to purchase than 16-bit A/D convertors.

In the standard application of five-hole probes in the nonnulling mode, all pressures are measured with respect to some reference pressure. For normal applications, atmospheric pressure can act as an adequately steady reference. But in low dynamic pressure applications, deviations in atmospheric pressure may dominate relative to the measured pressures. A bottle of air could be used as a reference pressure, if leakage could be totally eliminated. Another possibility is to use the total pressure at the pitot-static probe in the wind tunnel freestream as a reference pressure, though this eliminates the possibility of measuring P_{total}.

A.3. Modification of the Equations

Using total pressure as a reference pressure presents the problem that the total pressure is then unavailable, since a measurement of it would always yield zero (it would be its own reference pressure). This means that a re-examination of Treaster and Yocum's pressure coefficients is required (Equations A.1.1 through A.1.5).

The $C_{P_{pitch}}$ and $C_{P_{yaw}}$ calibration coefficients are unaffected by this modification because any reference pressure will be subtracted out. $C_{P_{total}}$ must be dropped from the list of coefficients since the total pressure cannot be measured; thus the number of coefficients is reduced to three. $C_{P_{static}}$ is still usable, but must be corrected, mostly for semantic reasons. Since the total pressure is acting as a reference, the actual static pressure cannot be measured, but rather the difference between the static and total pressures is measured. This difference is often referred to as the "dynamic head", and as such this differential pressure will be referred to here as P_{head}. Therefore, $C_{P_{static}}$ is now replaced in the list of calibration coefficients by $C_{P_{head}}$:

$$C_{P_{head}} = \frac{(\overline{P} - P_{head})}{(P_1 - \overline{P})}. \tag{A.3.1}$$

Even with all of the special considerations discussed above taken into account, the pressure coefficients still show nonnegligible random scatter. At the calibration stage, the effect of these errors can be reduced by performing a least squares fit to the calibration data, rather than generating spline curve fits.

Using a least squares algorithm requires a statement of an estimated functional form. By plotting each of $C_{P_{pitch}}$ and $C_{P_{yaw}}$ versus α, the order of the polynomial required for a proper curve fit may be inferred. Figure A.2a shows that the pitch angle, α, is an odd function of $C_{P_{pitch}}$. A linear approximation could be used, but cubic seems more accurate. On the other hand, $C_{P_{yaw}}$ versus α shows a family of

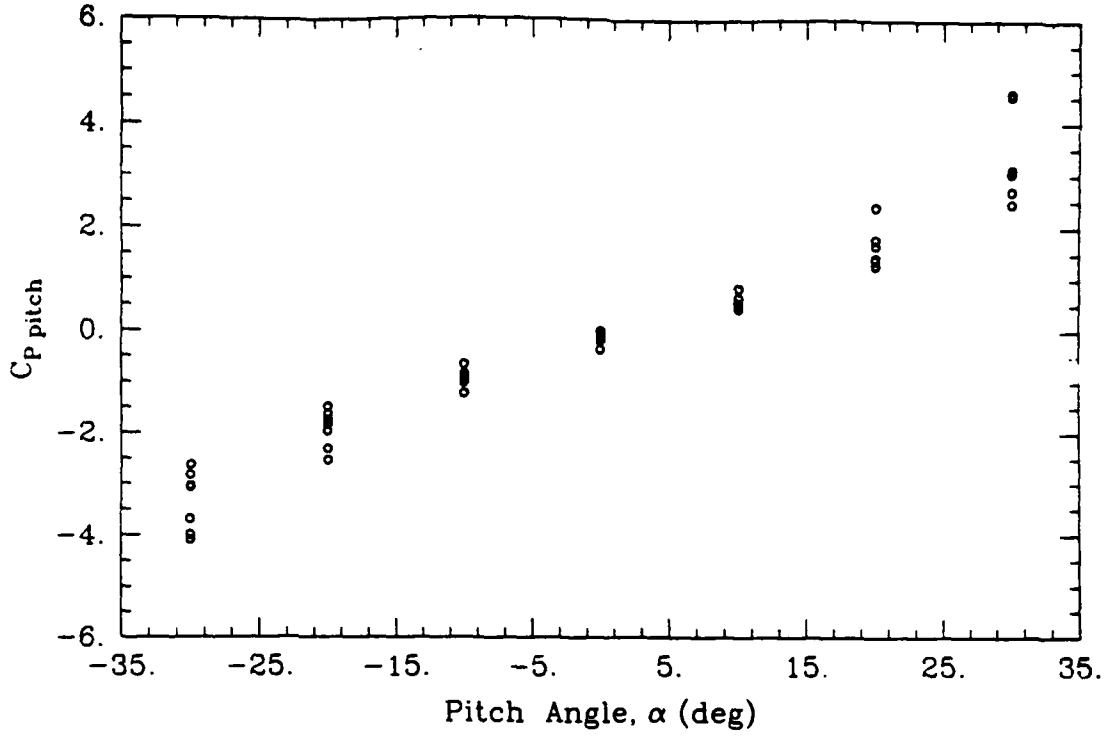

a. $C_{P\ pitch}$ versus α, Showing a Family of Cubic Curves

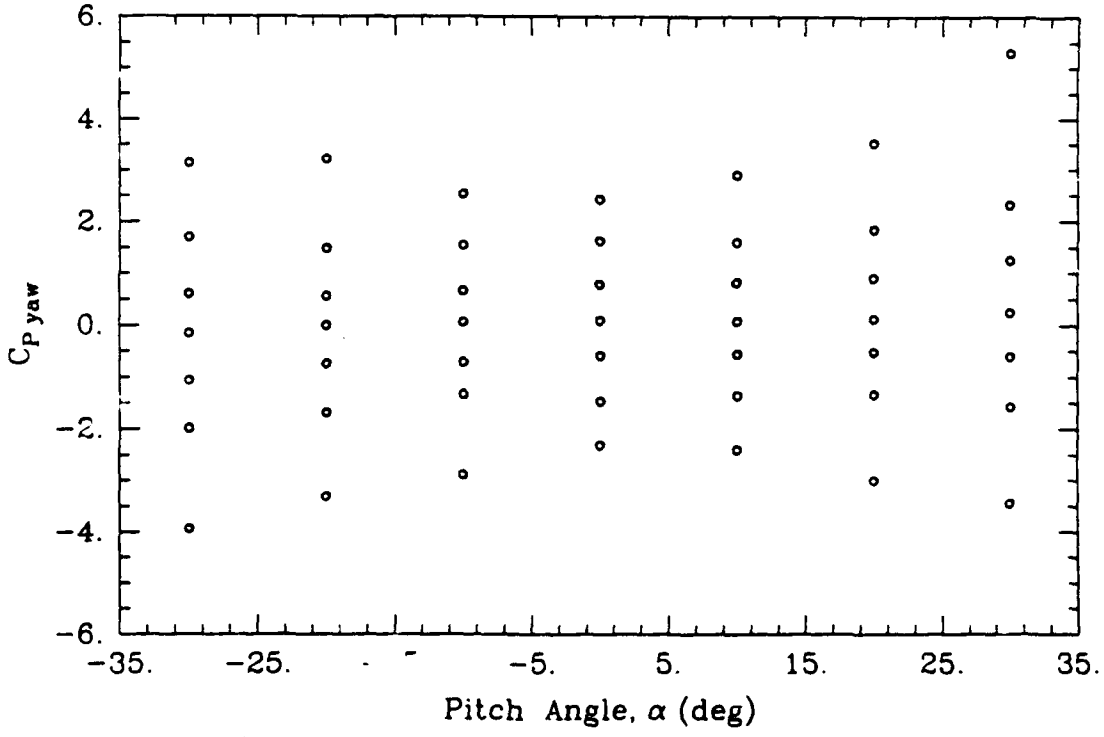

b. $C_{P\ yaw}$ versus α, Showing a Family of Parabolas

Figure A.2 Calibration Data Plotted to Illustrate Functional Dependence

parabolic curves, implying a quadratic dependance (see Figure A.2b). Furthermore, it can be seen that α and $C_{P_{pitch}}$ have a strong interdependence, whereas α and $C_{P_{yaw}}$ are more weakly interdependent. The yaw angle, β displays an analogous behavior with these two pressure coefficients.

Although other functional forms could be chosen, the ones used here for the least square fitting are as follows:

$$\begin{aligned} \alpha &= \alpha(C_{P_{pitch}}, \beta) \\ &= A_1 C_{P_{pitch}}^3 + A_2 C_{P_{pitch}}^2 + A_3 C_{P_{pitch}} + A_4, \\ \text{where } A_i &= a_{i1}\beta^2 + a_{i2}\beta + a_{i3} \\ \text{and } a_{ij} &= \text{least square fit constants } (i=1,2,3,4,\ j=1,2,3). \end{aligned} \tag{A.3.2}$$

Of course this equation can be expanded and simplified, but this form clearly shows the functional dependencies. And similiarly for β, it was assumed that

$$\begin{aligned} \beta &= \beta(C_{P_{yaw}}, \alpha) \\ &= B_1 C_{P_{yaw}}^3 + B_2 C_{P_{yaw}}^2 + B_3 C_{P_{yaw}} + B_4, \\ \text{where } B_i &= b_{i1}\alpha^2 + b_{i2}\alpha + b_{i3} \\ \text{and } b_{ij} &= \text{least square fit constants } (i=1,2,3,4,\ j=1,2,3). \end{aligned} \tag{A.3.3}$$

The least squares routine should be done using point weighting. Normally point weighting is done by placing more weight in the curve fit process on points with a small error or standard deviation. In this application it is convenient to place more weight on data points near the center of the calibration grid (that is, the calibration points with small angularity). These points are normally more accurately determined because at high flow angularity unsteady separation on the probe may occur. Furthermore, the flows studied here have small angularity, so these data points are more important and should be more tightly fit.

A least squares fit was also performed for $C_{P_{head}}$ of the following form:

$$\begin{aligned} C_{P_{head}} &= C_{P_{head}}(\alpha, \beta) \\ &= H_1\,\alpha^2 + H_2\,\alpha + H_3, \\ \text{where } H_i &= h_{i1}\,\beta^2 + h_{i2}\,\beta + h_{i3} \\ \text{and } h_{ij} &= \text{least square fit constants } (i{=}1,2,3,\ j{=}1,2,3). \end{aligned} \tag{A.3.4}$$

The parabolic relationships were chosen by observation of the curve forms presented in Figures A.3.

Reynolds number corrections were attempted, but typically ended up adding error to the final results. Velocities at largely different Reynolds numbers can be studied without any correction, as long the data are viewed in a qualitative manner. This was the approach taken in this study for boundary layer surveys. Wall proximity effects were also ignored because only those data points that are within about two probe diameters (in this study, about 3 mm) of the wall should show any such errors.

In summary, this procedure has reduced the calibration data to three equations with the following functional forms:

$$\alpha = \alpha(C_{P_{pitch}}, \beta), \tag{A.3.2}$$

$$\beta = \beta(C_{P_{yaw}}, \alpha), \tag{A.3.3}$$

$$C_{P_{head}} = C_{P_{head}}(\alpha, \beta). \tag{A.3.4}$$

In applying this five-hole probe system, measurements are made to determine $C_{P_{pitch}}$ and $C_{P_{yaw}}$. Given initial guesses at α and β, Equations A.3.2 and A.3.3 quickly iterate to convergence. For this study, initial guesses of zero for both angles served quite well. Then knowing α and β, $C_{P_{head}}$ can be calculated in a straightforward manner, from Equation A.3.4.

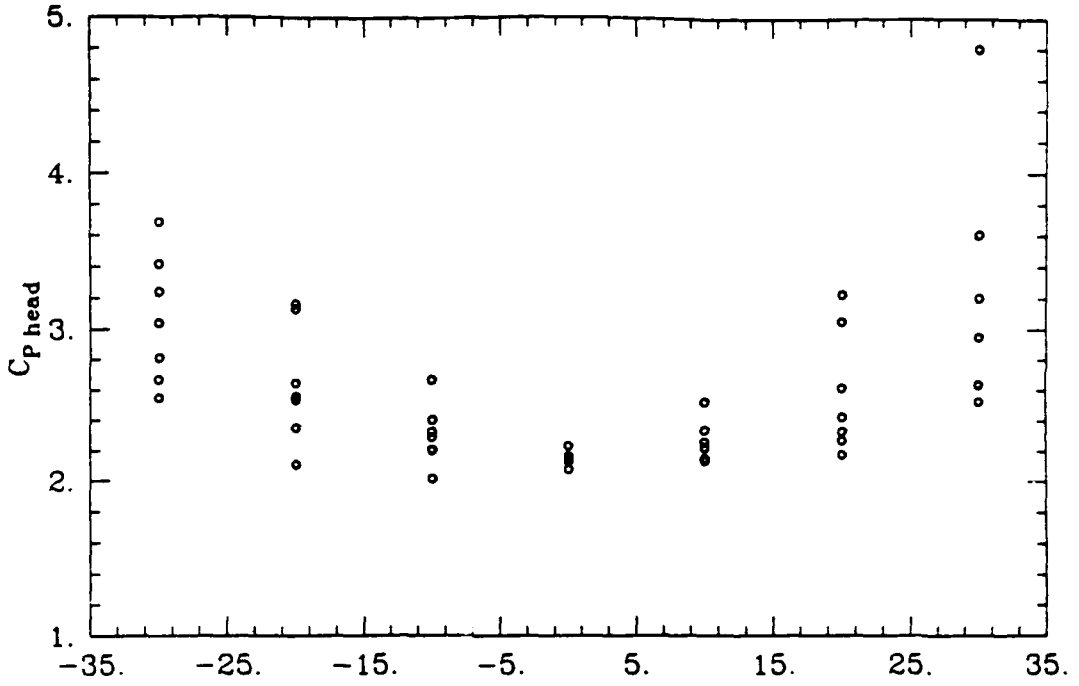

a. $C_{P\,head}$ versus α, Showing a Family of Parabolas

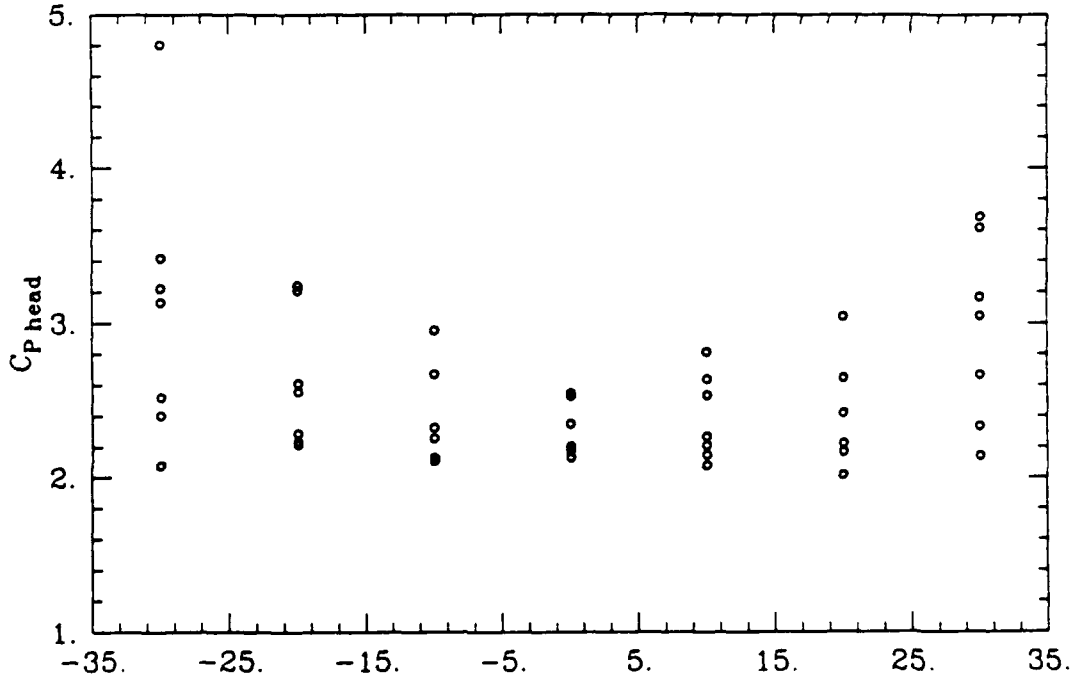

b. $C_{P\,head}$ versus β, Showing a Family of Parabolas

Figure A.3 Calibration Data Plotted to Illustrate Functional Dependence

A.4. Filtering the Data

Even with all the care and patience that has been spent on getting accurate data, there will still be some noticeable experimental error. But the guidelines discussed in Sections A.2 and A.3 will suffice, if the final goal is to generate vector velocity plots showing the large scale flow characteristics.

In this study, vorticity data were desired, thus necessitating differentiation of the velocity data. Random experimental error tends to amplify when taking derivatives, so this error must be reduced or eliminated prior to differentiation. Two obvious approaches to reducing experimental error are (1) to decrease the pressure data standard deviation tolerance, or (2) to read in more pressures before averaging. But both of these solutions extend the experiment execution time, which for this study is already quite long (as discussed in Section 2.6). A third approach, namely smoothing the data before performing the derivatives, was employed in the present application.

For computer applications, the easiest filtering method is Fast Fourier Transform (FFT) filtering. For a one-dimensional study this is quite commonly performed, and the technique is fairly straightforward. A frequency spectrum is generated by performing a forward FFT on the experimental data. (Note that if the independant variable in the original data set is a spatial coordinate, the frequency spectrum is really a wave number spectrum, where the "frequency" has units of inverse length.) The frequency spectrum plot is then examined to choose regions of high amplitude waves. A low-pass, high-pass, or band-pass filter is applied to the frequency space data, and the inverse FFT is performed yielding the filtered data. In applications such as that described here, a low-pass filter is almost always used, to keep the more "DC" (large scale) components of the spectrum, and eliminate the high frequency noise (experimental error).

For this particular application, a two-dimensional FFT was required, because data were taken in a plane. The FORTRAN subroutine for performing this multi-dimensional fourier transform was found in the text by Press et al. (1986).

A filtering process in two dimensions is analogous to the one-dimensional situation, except that the low frequency components must be preserved for both dimensions. The two-dimensional frequency spectrum is shown in Figure A.4 displaying the large amplitude components in the center (near zero wave numbers for both dimensions). A cross-shaped pattern of other relatively high amplitude components can be observed as well. One line of the cross corresponds to low frequency characteristics in one dimension, and the other line corresponds to low frequency characteristics in the other dimension. The low-pass filter in this situation will effectively filter out the four corners of the spectrum (corresponding to high frequency noise).

To illustrate this filtering process, Figure A.5 shows the same spectrum as did Figure A.4, except with a $\log_{10}$ amplitude scale to exaggerate the high frequency noise components. Figure A.6 is again the same spectrum, after the low-pass filtering described above was applied (again, with a $\log_{10}$ scale). As can be seen, the frequency cutoffs were chosen so that only the highest amplitude peaks (lowest frequencies) were included in the filtered spectrum. Figures A.4 through A.6 are a spectrum for the x-velocity component. The same filtering process must also be applied for the y- and z-velocity components (filtering at the same frequency cutoffs).

Once this filtering process is performed, velocity data can be differentiated to yield physically realistic results. Several methods for differentiation of a discrete data set are compared in Appendix C.

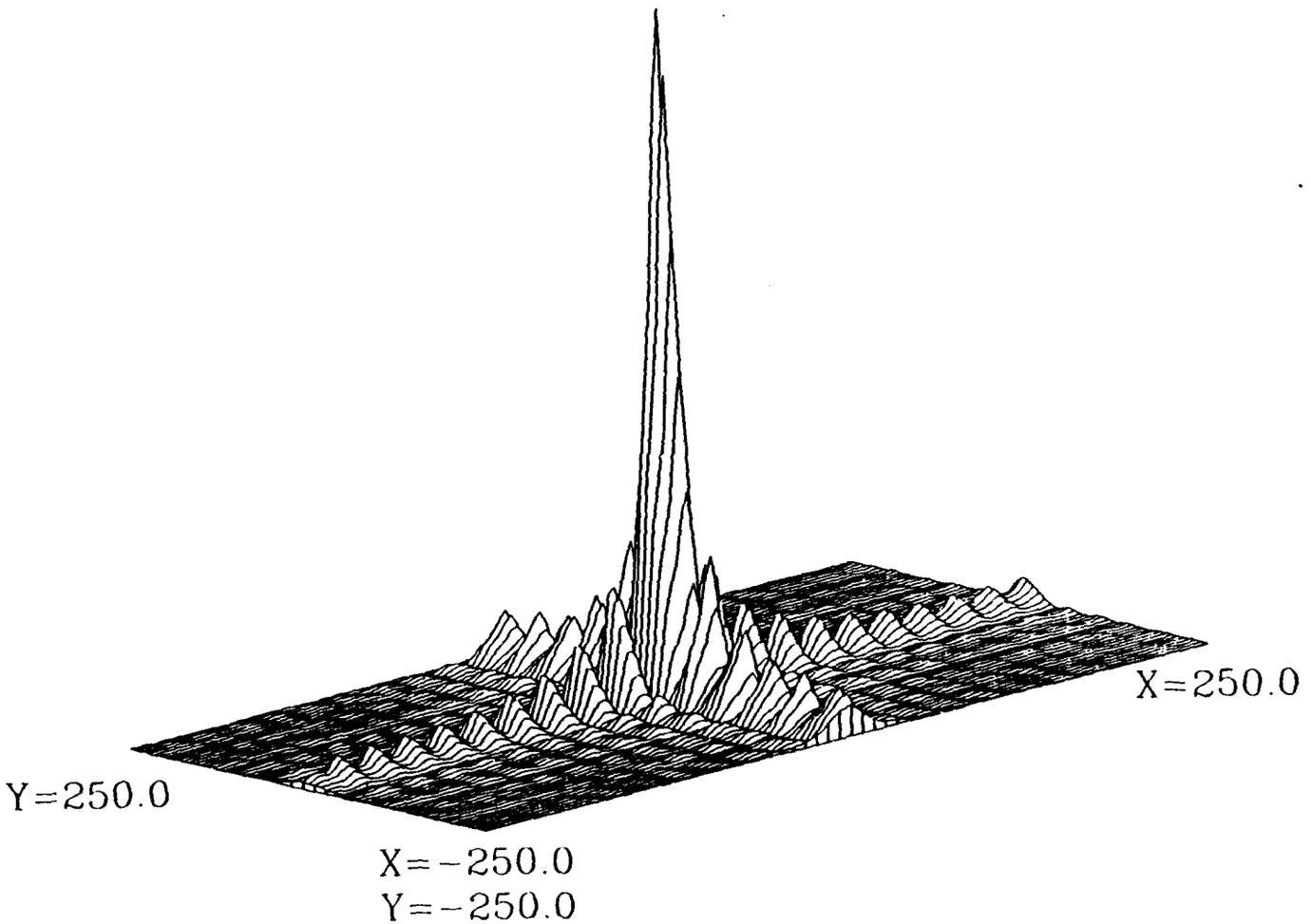

Figure A.4 Example Two-Dimensional Velocity Spectrum, before Filtering (Proportional Amplitude Scaling)

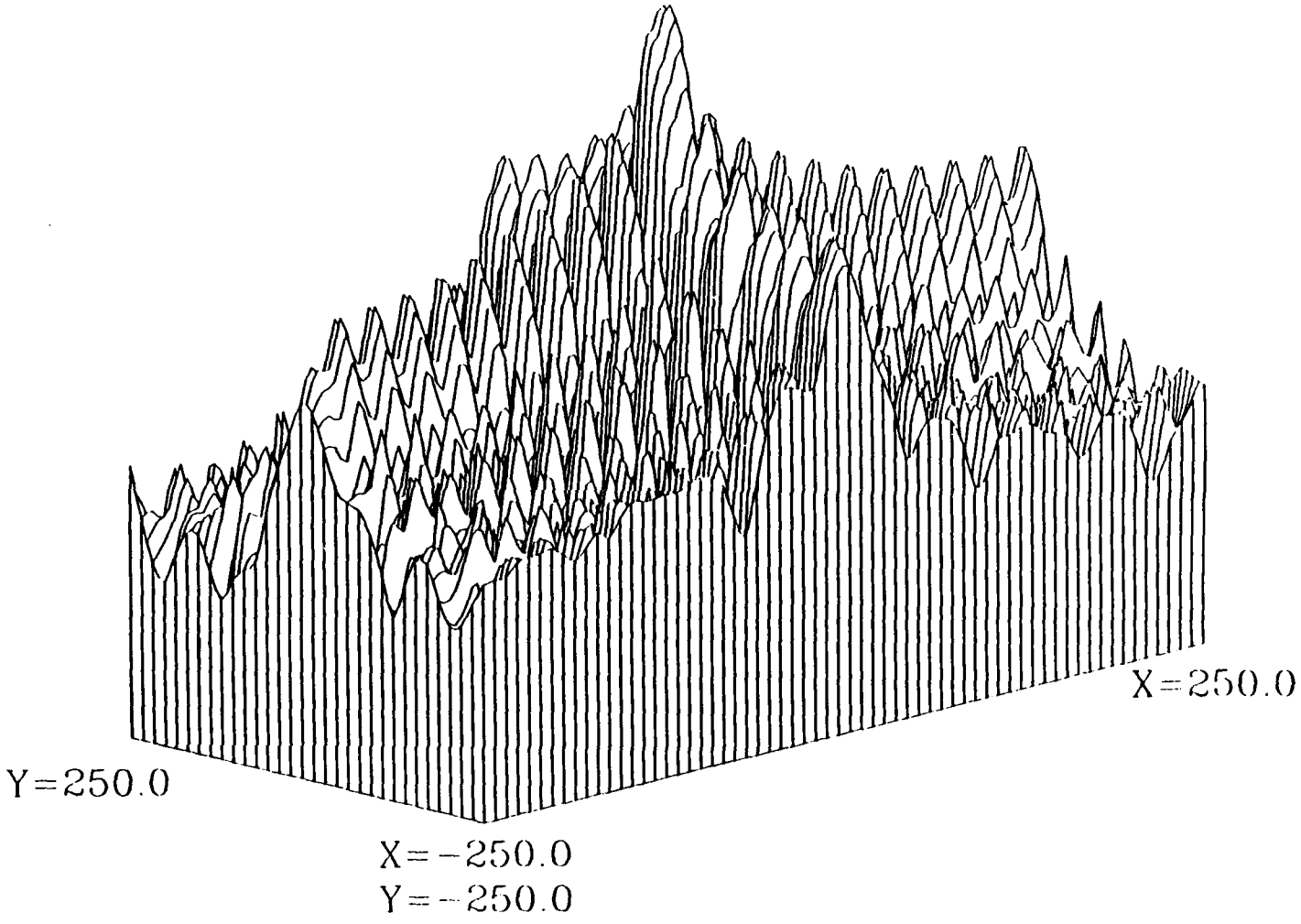

Figure A.5 Example Two-Dimensional Velocity Spectrum, before Filtering (Logarithmic Amplitude Scaling)

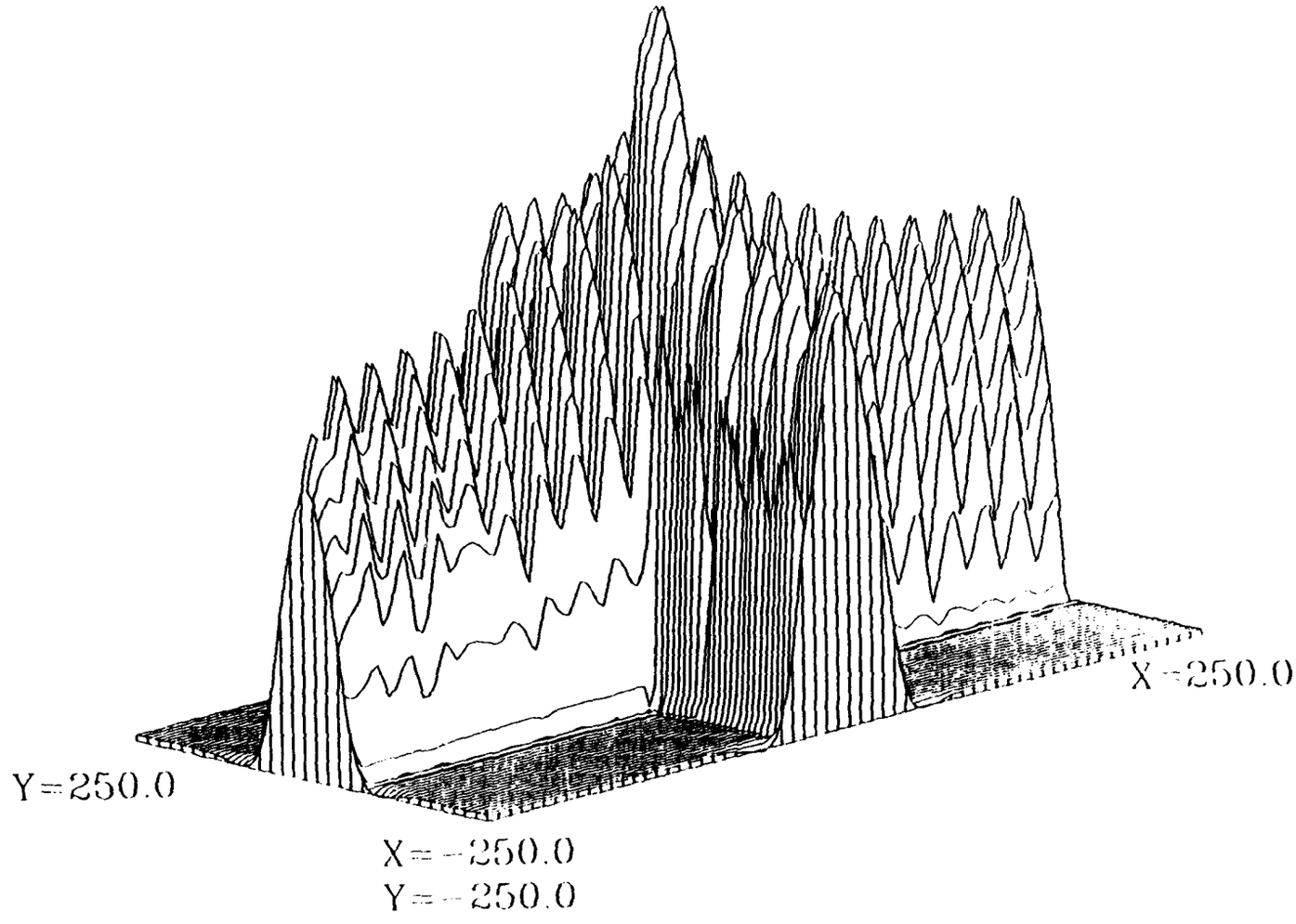

Figure A.6 Example Two-Dimensional Velocity Spectrum, after Filtering (Logarithmic Amplitude Scaling)

Appendix B

FIVE-HOLE PROBE CALIBRATION DATA

In the 1978 paper of Treaster and Yocum, five-hole probe calibration data are presented by plotting the 49 angular calibration coefficients as $C_{P_{yaw}}$ versus $C_{P_{pitch}}$. The static and total pressure coefficients are also plotted as two more graphs, $C_{P_{static}}$ versus α and $C_{P_{total}}$ versus α. This is a standard format; the corresponding graphs for the current system used in this study are presented in Figures B.1. Note that Figure B.1b shows $C_{P_{head}}$ versus α, as per the modified equations discussed in Section A.3.

The standard angular calibration plot format was not convenient for showing the least square fit curves because of the implicit nature of Equations A.3.2 and A.3.3. To make a plot of these curves, each of the 49 points shown in Figure B.1a were substituted into the least square fit equations represented by Equations A.3.2 and A.3.3. To produce a plot of the curves, rather than just a set of 49 points, linear interpolation was used to generate ten extra data points between adjacent points in Figure B.1a. These points were also substituted into the least square fit equations, and the resulting angles plotted to create Figure B.2a.

If the scheme outlined in Appendix A had worked perfectly, the least square fit curves would form a rectangular grid with a calibration angle located at each vertex. The errors seen in Figure B.2a are mostly due to calibration coefficient errors, as illustrated by the fact that many points in Figure B.1a did not fall on smooth curves. These errors did not adversely affect the derivation of the least square fit equations because of the smoothing nature of the least square fitting

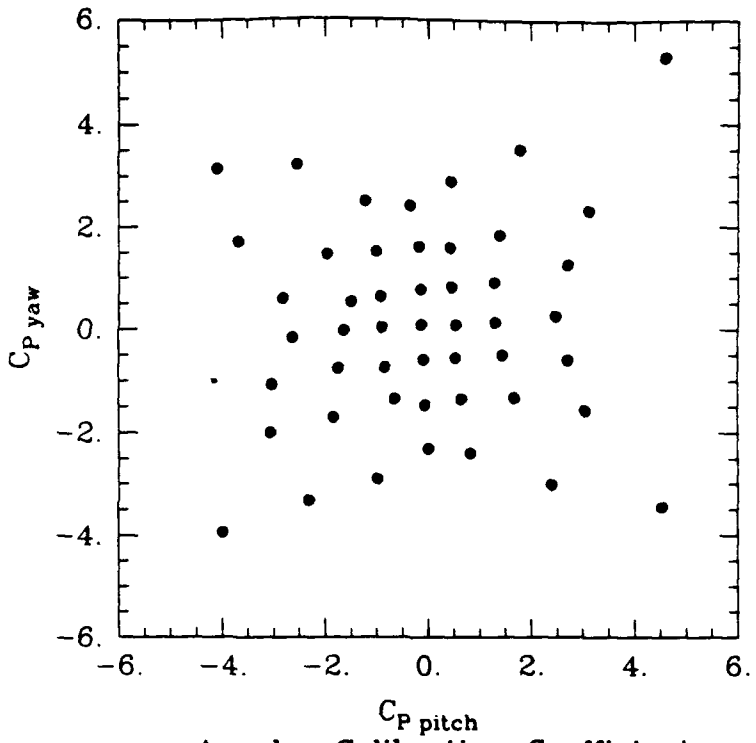

a. Angular Calibration Coefficients

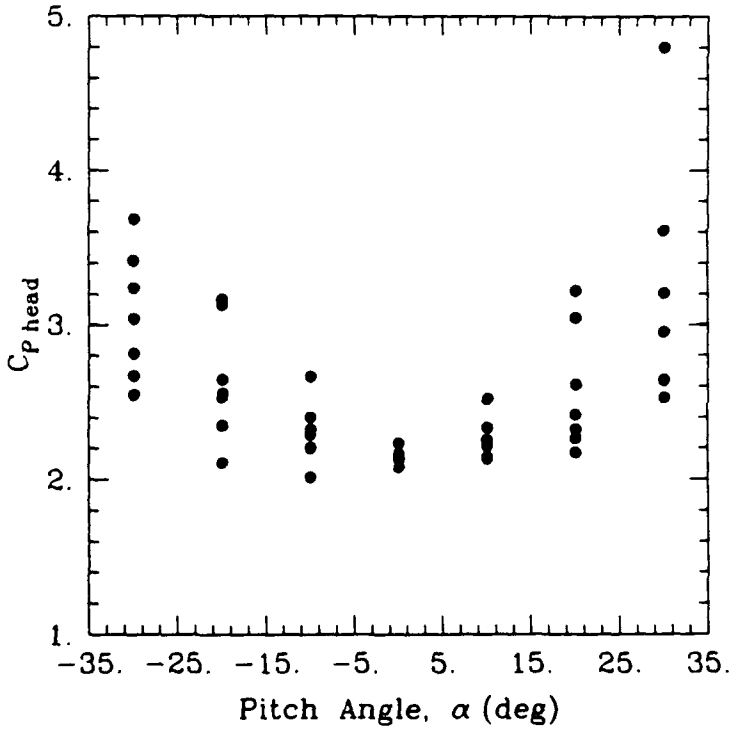

b. Dynamic Head Calibration Coefficients

Figure B.1 Five-Hole Probe Calibration Data Plotted in Standard Format

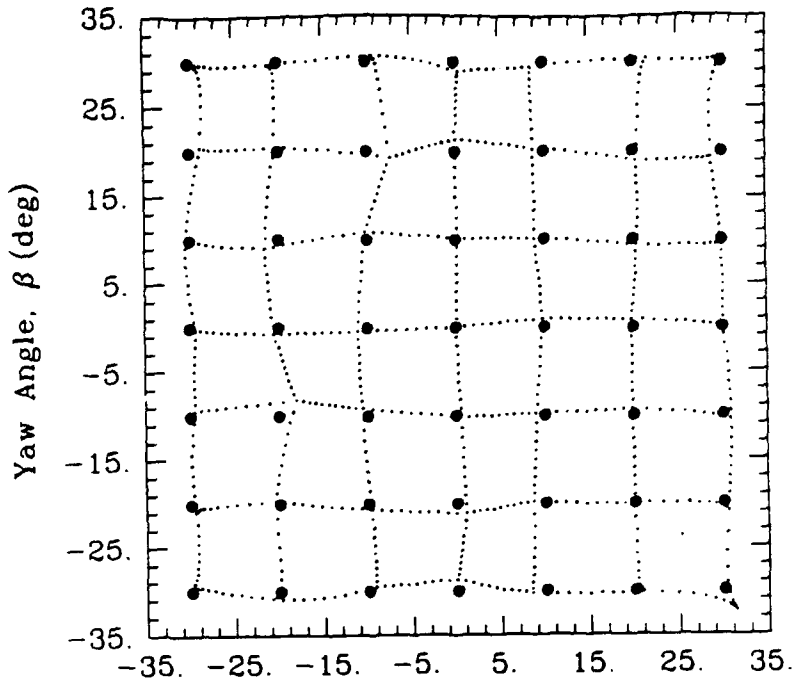

a. Angular Calibration Grid

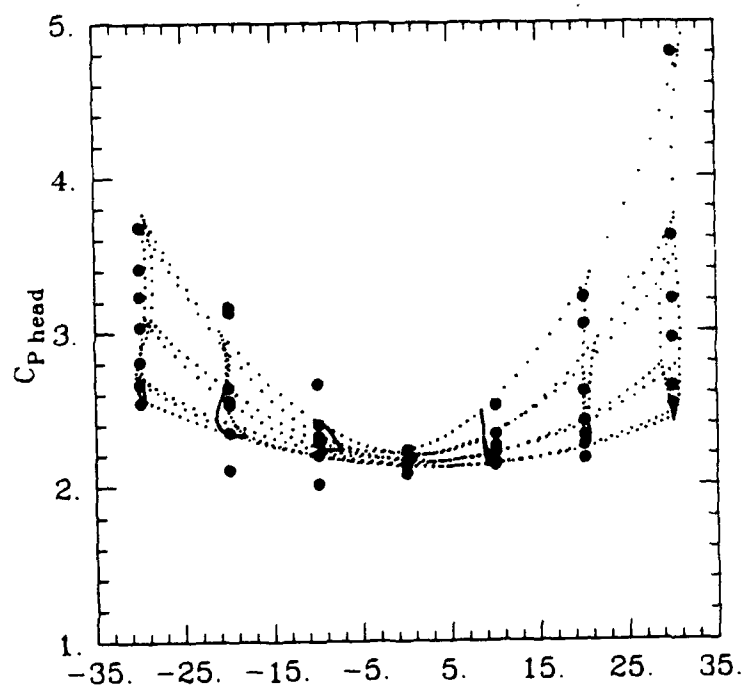

b. Dynamic Head Calibration Coefficients

Figure B.2 Five-Hole Probe Calibration Data Showing Least Square Fit Curves

process. When the erroneous points are substituted into the equations to produce the curves of Figure B.2a, the direct influence of these points on the results cannot be avoided.

An analagous procedure was performed to show the least square fit curves as derived for determining $C_{P_{head}}$ (see Figure B.2b).

Appendix C

VORTICITY CALCULATION METHODS

C.1. Description of Calculations

The calculation of streamwise vorticity from the measured velocity data sets allowed for a better understanding of the flow characteristics. This enabled the plotting of vorticity contours for graphical depictions of the vortical flow, as well as computation of overall circulation values.

Appendix A dealt extensively with methods for minimizing velocity vector scatter. Here, three methods for differentiating the discrete velocity data to generate vorticity data are presented and compared.

The exact vorticity definition, used in this study was

$$\omega_x = \frac{\partial V}{\partial Z} - \frac{\partial W}{\partial Y}. \tag{C.1.1}$$

This is the negative of most vorticity definitions, because of the left-handed coordinate system used. The three approaches to making a finite difference approximation of Equation C.1.1 are for convenience referred to as "Diamond Cell", "Square Cell", and "Third Order".

Figure C.1 shows a general data grid in the Y-Z plane, with an equal node point spacing of Δ in each direction. For calculating the vorticity at (i,j), the Diamond Cell approach uses nodes $(i+1,j)$, $(i-1,j)$, $(i,j+1)$, and $(i,j-1)$ to discretize Equation C.1.1. This diamond-shaped calculation cell yields a second order accurate vorticity using a standard central difference formula

$$\omega_{x_{i,j}} = \frac{V_{i+1,j} - V_{i-1,j}}{2\Delta} - \frac{W_{i,j+1} - W_{i,j-1}}{2\Delta}. \tag{C.1.2}$$

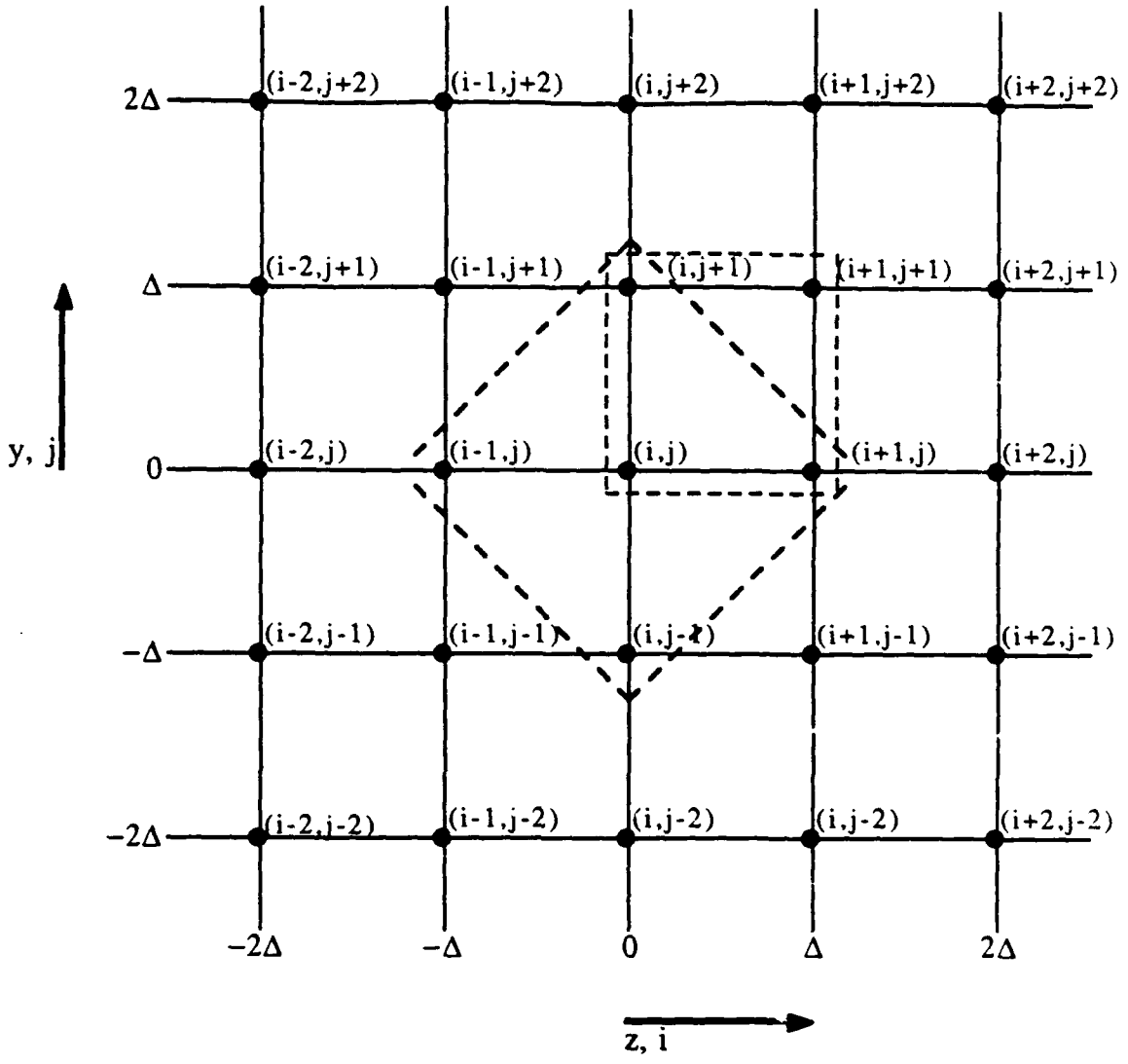

Figure C.1 Finite Difference Calculation Grid

The Square Cell approach utilizes four nodes on the corners of a square to compute the vorticity at the square's center, say $(i+\frac{1}{2}, j+\frac{1}{2})$. The values of V at the left nodes of the square are averaged to find V at $(i, j+\frac{1}{2})$. The same operation is performed at the right two nodes to find V at $(i+1, j+\frac{1}{2})$. A similar procedure is used at the top and bottom of the square to yield W at $(i+\frac{1}{2}, j+1)$ and $(i+\frac{1}{2}, j)$, respectively. Then central differences are applied, much as was done in the Diamond Cell approach, except that the diamond is half the size as the one used in the Diamond method. The final form of the equation is

$$\omega_{z_{i+\frac{1}{2},j+\frac{1}{2}}} = \frac{V_{i+1,j+\frac{1}{2}} - V_{i,j+\frac{1}{2}}}{\Delta} - \frac{W_{i+\frac{1}{2},j+1} - W_{i+\frac{1}{2},j}}{\Delta}, \qquad \text{(C.1.3)}$$

$$\text{where in general: } A_{k+\frac{1}{2}} = \frac{A_{k+1} + A_k}{2}.$$

Therefore, we expect double the spatial resolution using squares. But the appropriateness of using average values for achieving the superior resolution is questionable; it is the equivalent of performing a linear interpolation.

The Third Order method simply uses third order central difference formulas, much the same way as the Diamond Cell approach uses second order central difference formulas. Here though, the four data points $(i, j+2)$, $(i, j+1)$, $(i, j-1)$, and $(i, j-2)$ are needed to find $\frac{\partial W}{\partial Y}$ at (i, j). And similarly, four points along the horizontal grid line at j are required to find $\frac{\partial V}{\partial Z}$ at (i, j). The result is

$$\omega_{z_{i,j}} = \frac{-V_{i+2,j} + 8\,V_{i+1,j} - 8\,V_{i-1,j} + V_{i-2,j}}{12\,\Delta} - \frac{-W_{i,j+2} + 8\,W_{i,j+1} - 8\,W_{i,j-1} + W_{i,j-2}}{12\,\Delta}. \qquad \text{(C.1.4)}$$

The derivation of a circulation value was also quite useful in giving an overall summary of the vorticity distribution in a flow field. Circulation can be expressed as:

$$\Gamma = \int \omega_z \, dA. \qquad \text{(C.1.5)}$$

In this study, the determined values of ω_z are evenly distributed on a rectangular grid, with node spacing Δ. This allows the simplification of Equation C.1.5 to the following form:

$$\Gamma = \Delta^2 \sum_{i,j} \omega_z. \tag{C.1.6}$$

C.2. Comparison of Results

Vorticity data were generated using all three finite difference approaches discussed in the previous section, for the unmodified geometry case in this study (see Section 3.2). These are presented here as Figures C.2 through C.4.

As can be seen in Figure C.2 the Square Cell approach showed a great deal of small scale detail, thus obscuring the large scale characteristics of the flow. The Diamond Cell approach showed much less fine detail, and allowed clear observation of the vortex's vorticity lines (Figure C.3). The Third Order method gave a picture with less detail the Diamond, but more than the Square, as seen in Figure C.4.

While it is unclear which level of detail most accurately reflected the physics of the flow, all three approaches shared the same general patterns of regions of high vorticity, regions of low vorticity, and regions of negative vorticity. Therefore it was concluded that all three methods generated valid, physical results; the choice of which one to use merely depended on the level of detail required for the particular application. Besides, filtering of the high detail vorticity could have been used to wash out undesired small scale features.

The calculation of circulation values using each method's vorticity data was performed to further investigate the agreement of the three methods. It was found that the deviation in total circulation was less than $\pm 1.5\%$ between the three techniques, for the unmodified geometry test case. For some other experimental situations, the total circulation agreement was not quite as good, as seen in

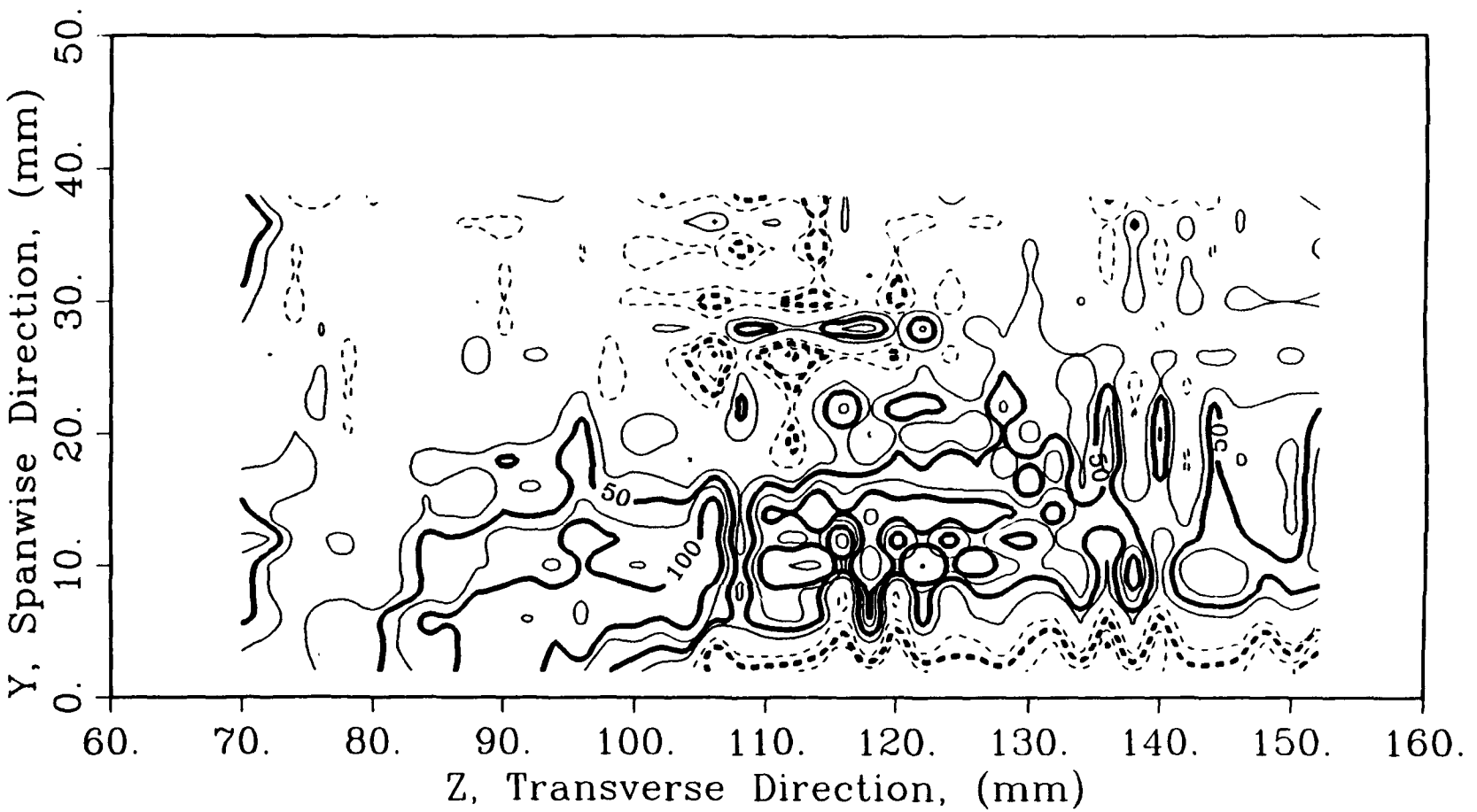

Figure C.2 Example Streamwise Vorticity Contours Using Square Cell Finite Differences

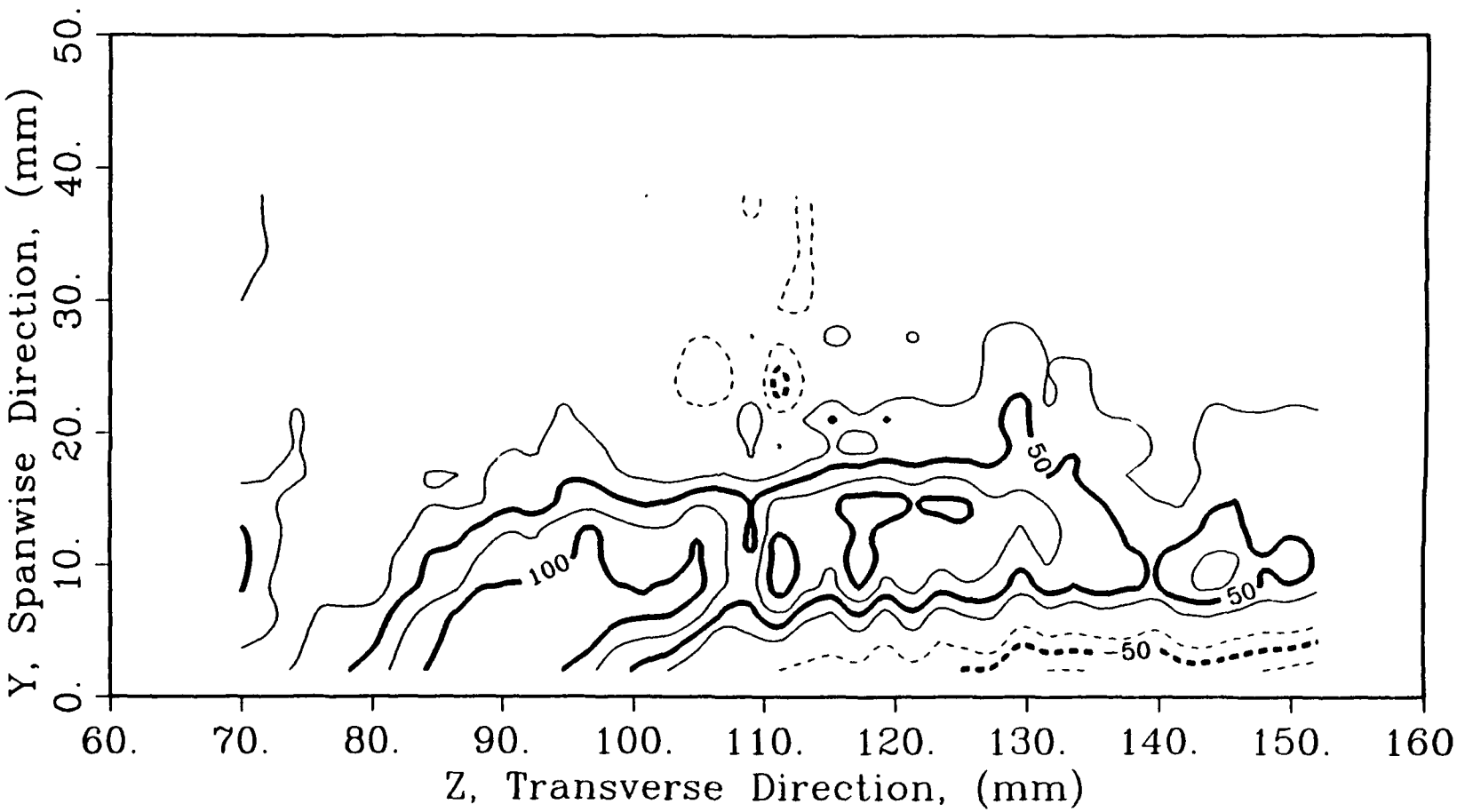

Figure C.3 Example Streamwise Vorticity Contours Using Diamond Cell Finite Differences

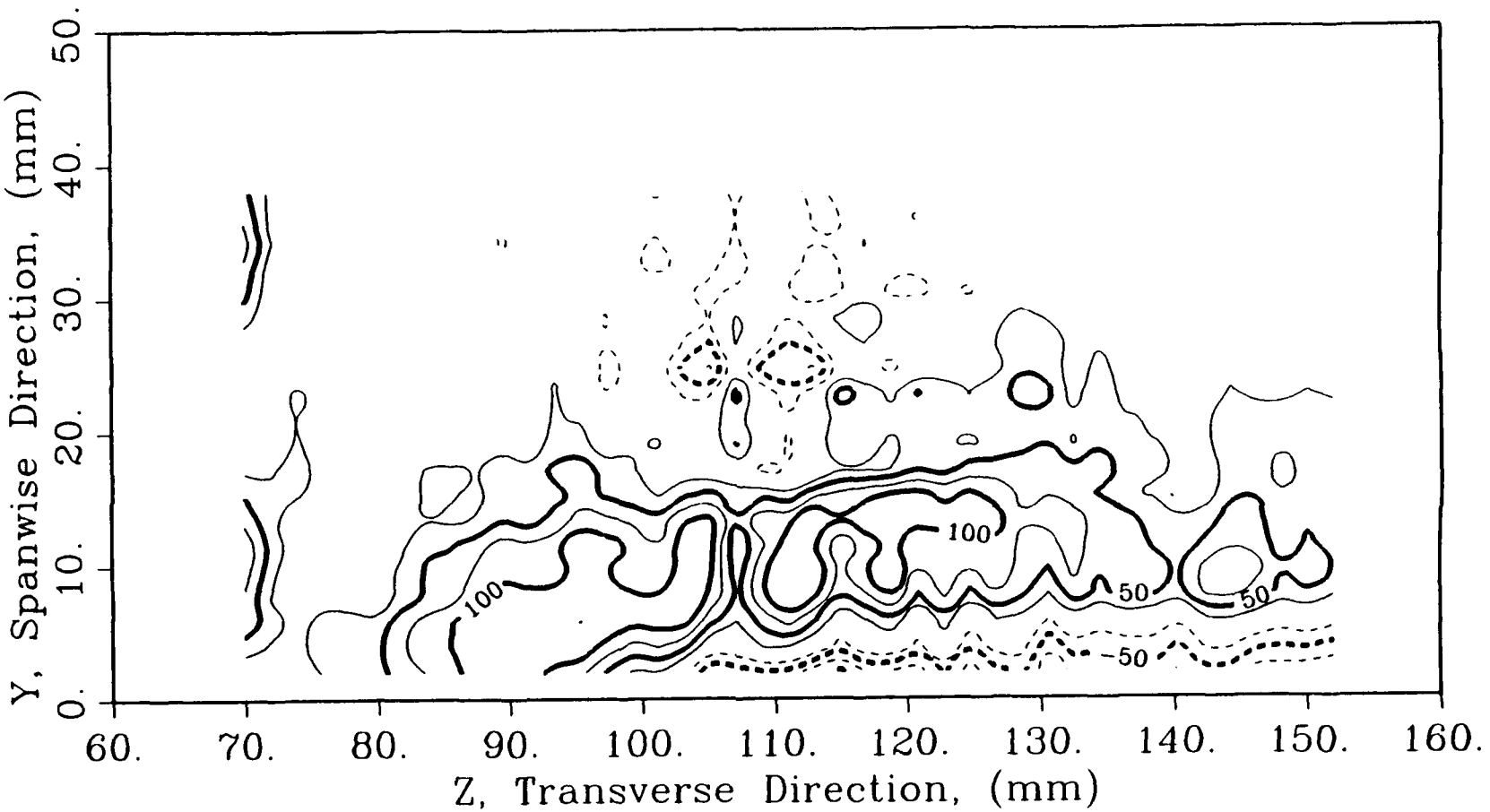

Figure C.4 Example Streamwise Vorticity Contours Using Third Order Finite Differences

Figure 5.1.

The Diamond Cell approach was chosen as the most convenient calculation method for the purposes of this study. It showed the required large scale phenomena, without unnecessary small scale details, and without requiring further data filtering. Additionally, it happened to be the most computationally efficient approach of the three presented here. Therefore, only Diamond Cell vorticity contours have been presented in the body of this text.

Appendix D

RAW DATA

PRESENTED IN GRAPHICAL FORM

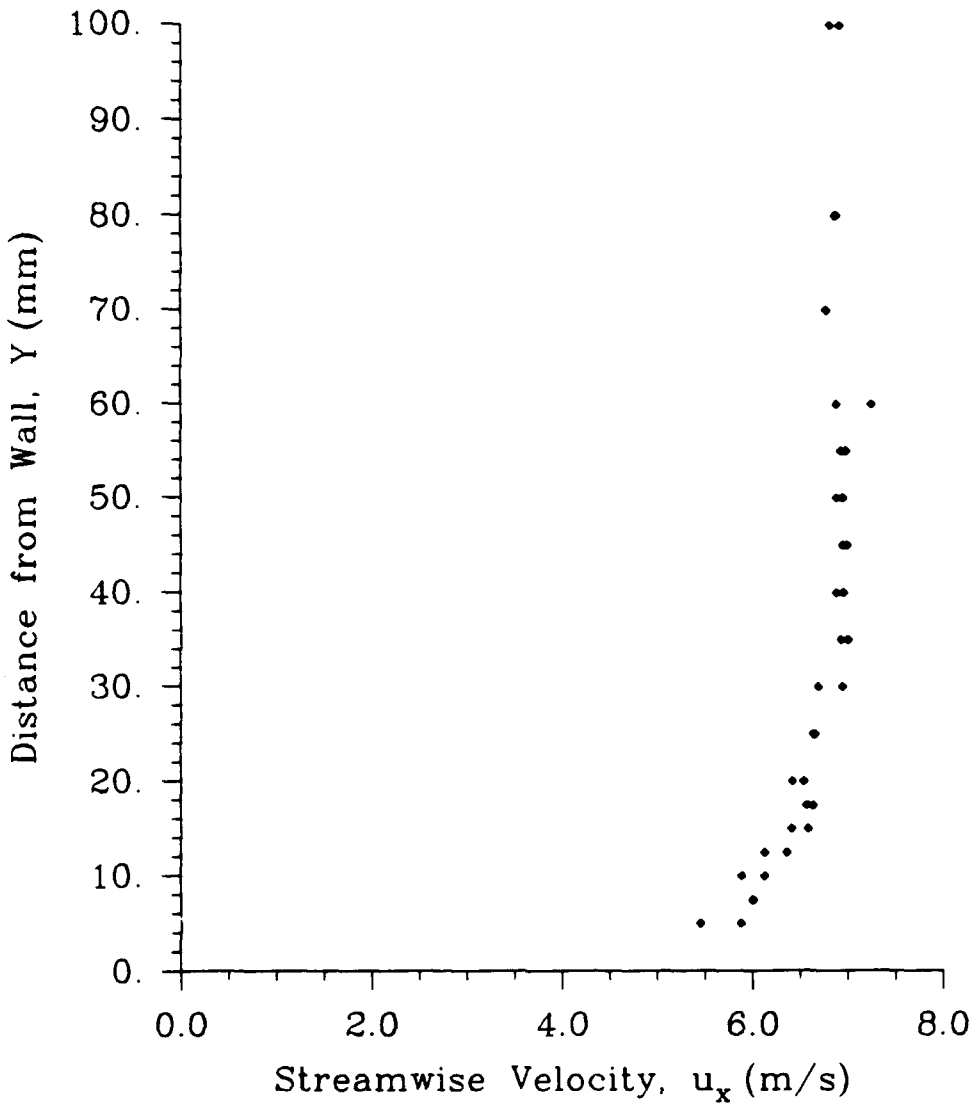

Figure D.1 Boundary Layer Survey for Experiment with: Solid Wall

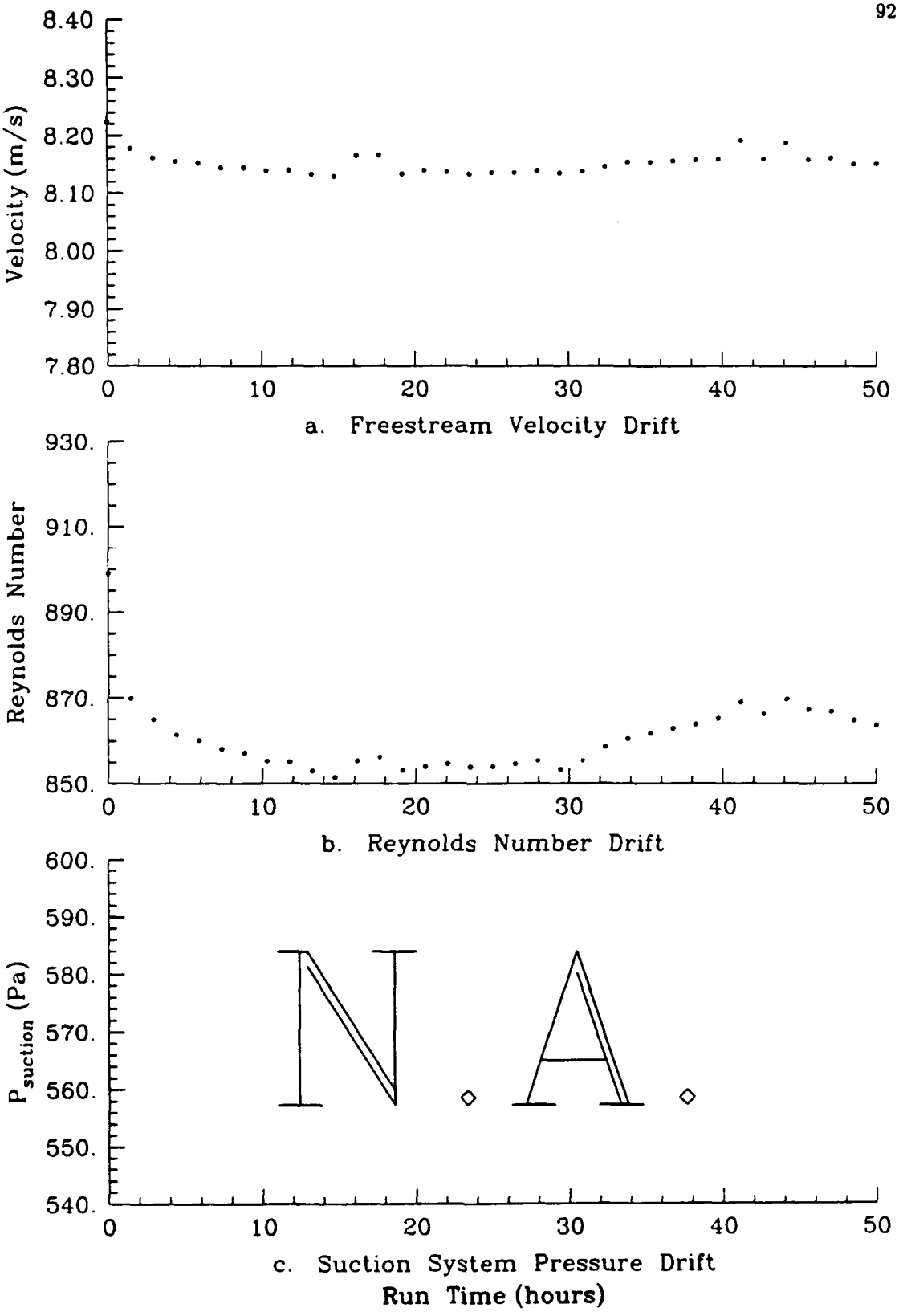

Figure D.2 Property Drifts for Experiment with: Solid Wall, Unmodified Geometry

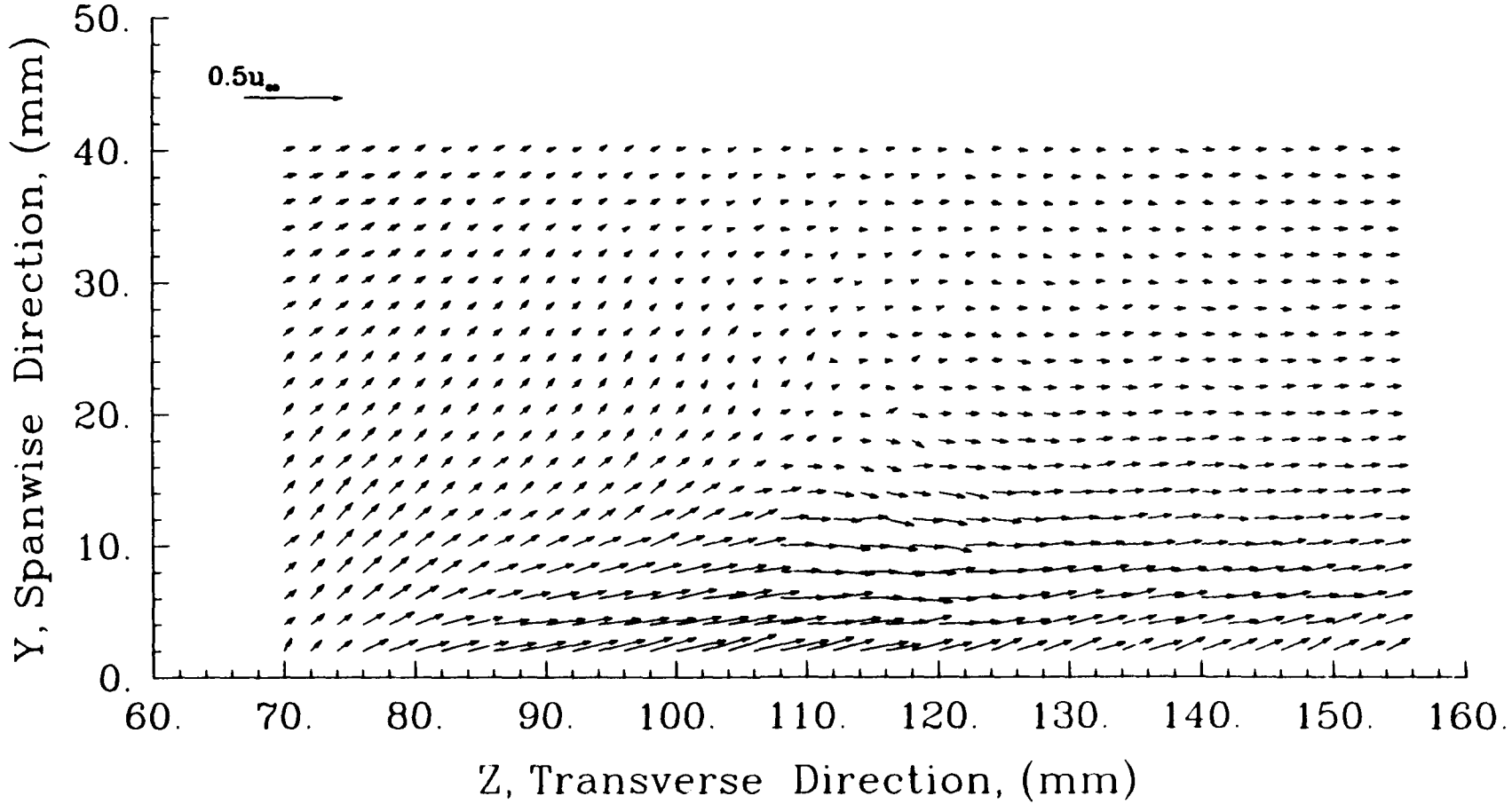

Figure D.3 Unfiltered Secondary Flow Velocity Vectors for Experiment with: Solid Wall, Unmodified Geometry

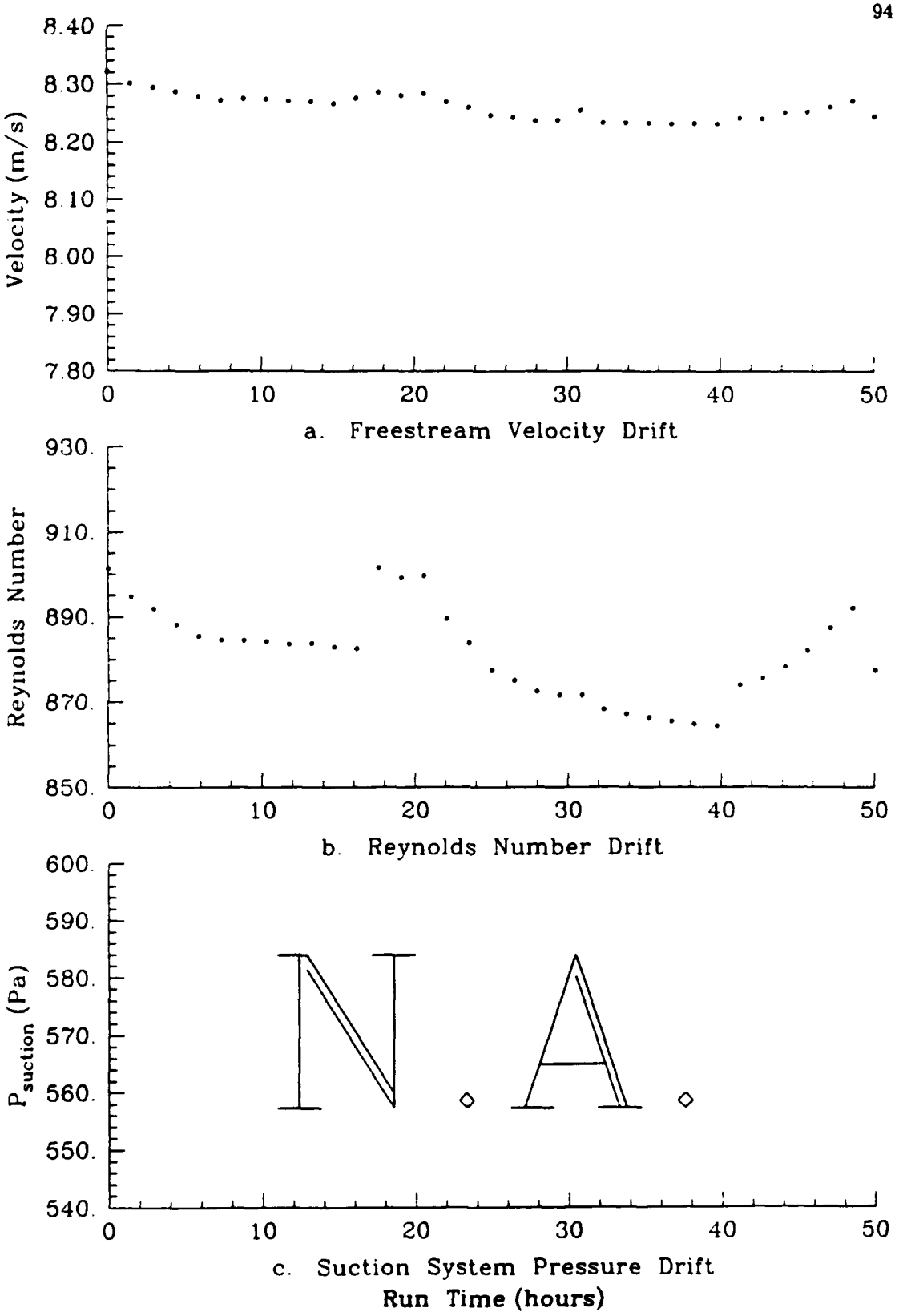

Figure D.4 **Property Drifts for Experiment with: Solid Wall, Fairing in Place**

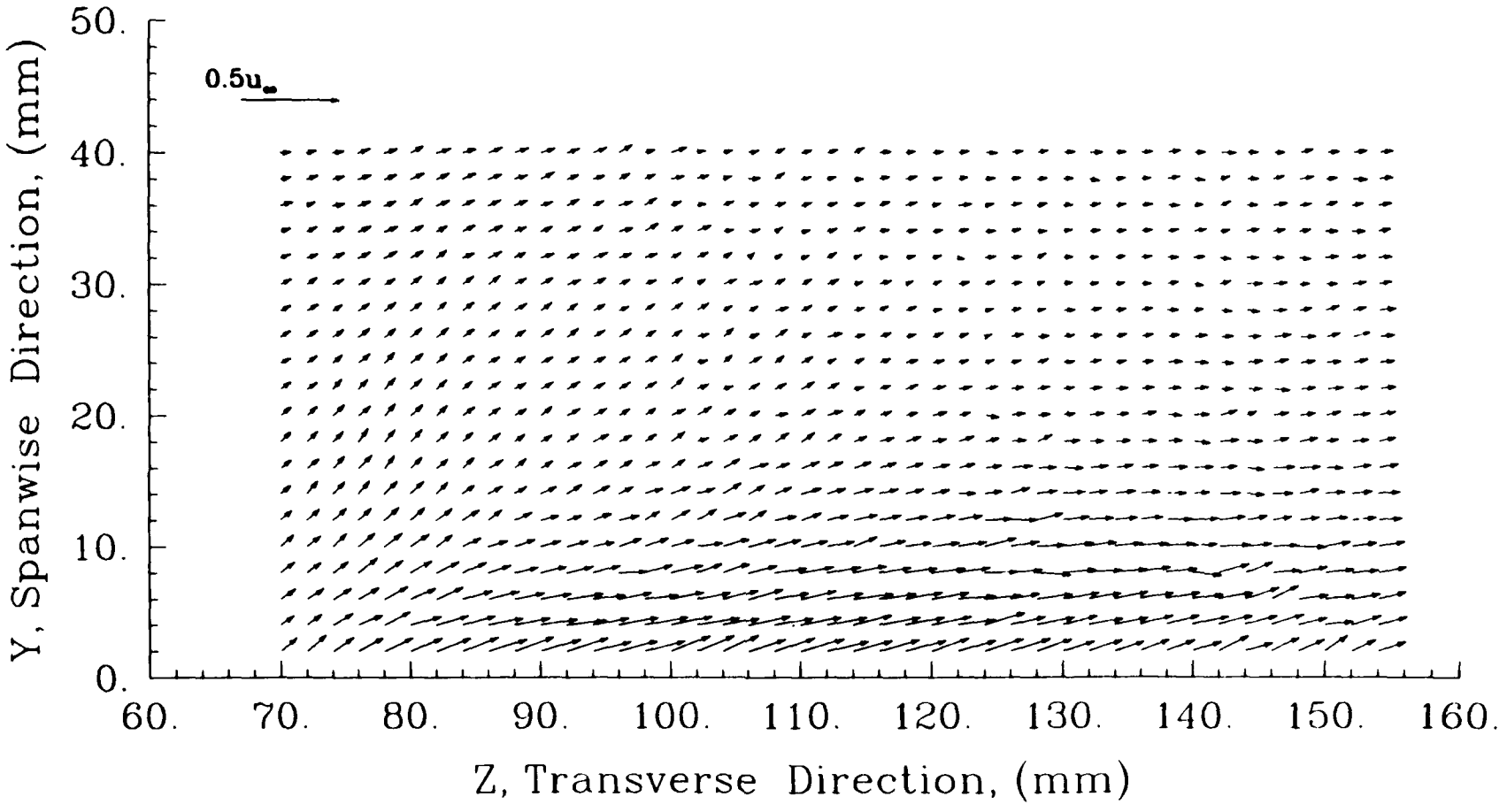

Figure D.5 Unfiltered Secondary Flow Velocity Vectors for Experiment with: Solid Wall, Fairing in Place

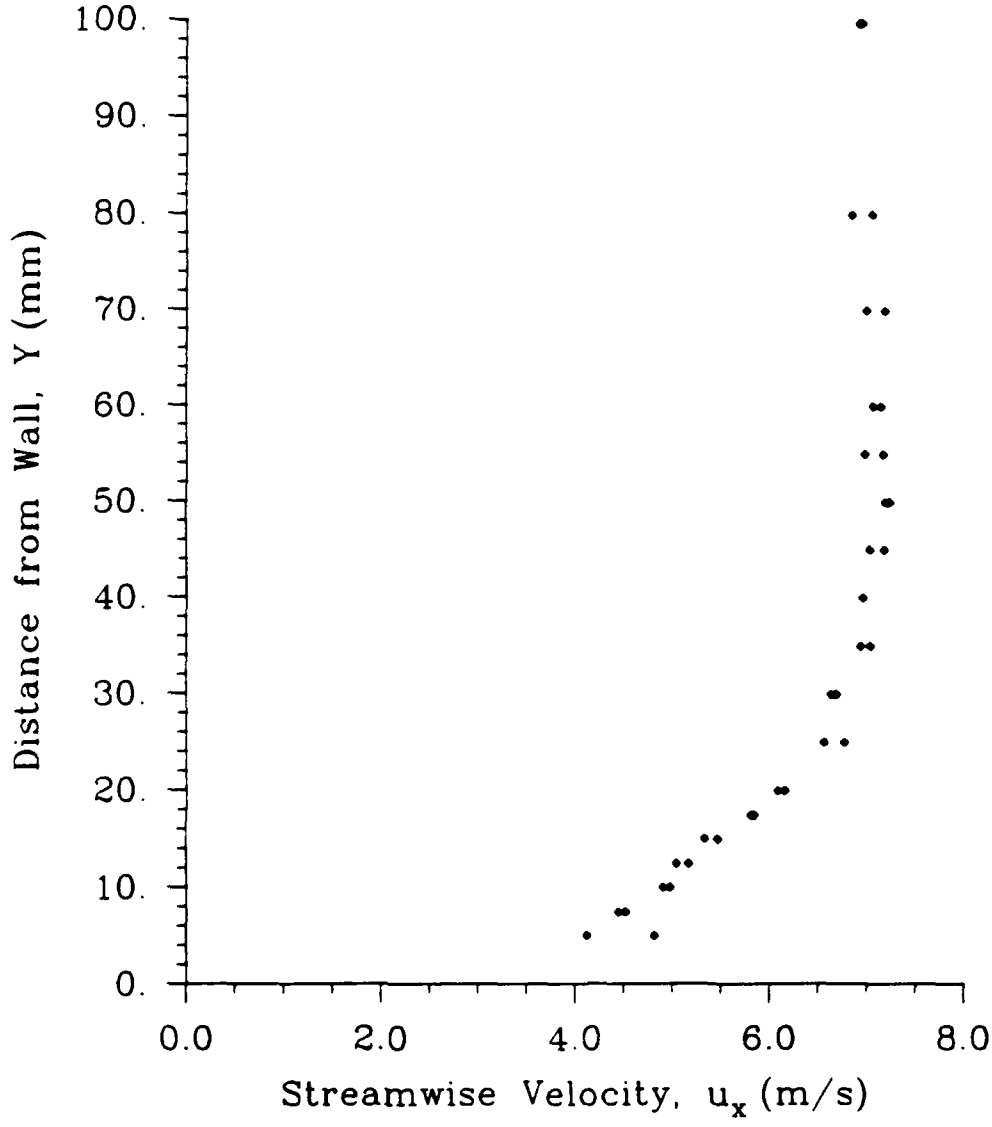

Figure D.6 Boundary Layer Survey for Experiment with: Porous Wall, No Suction ($Q_s = 0$)

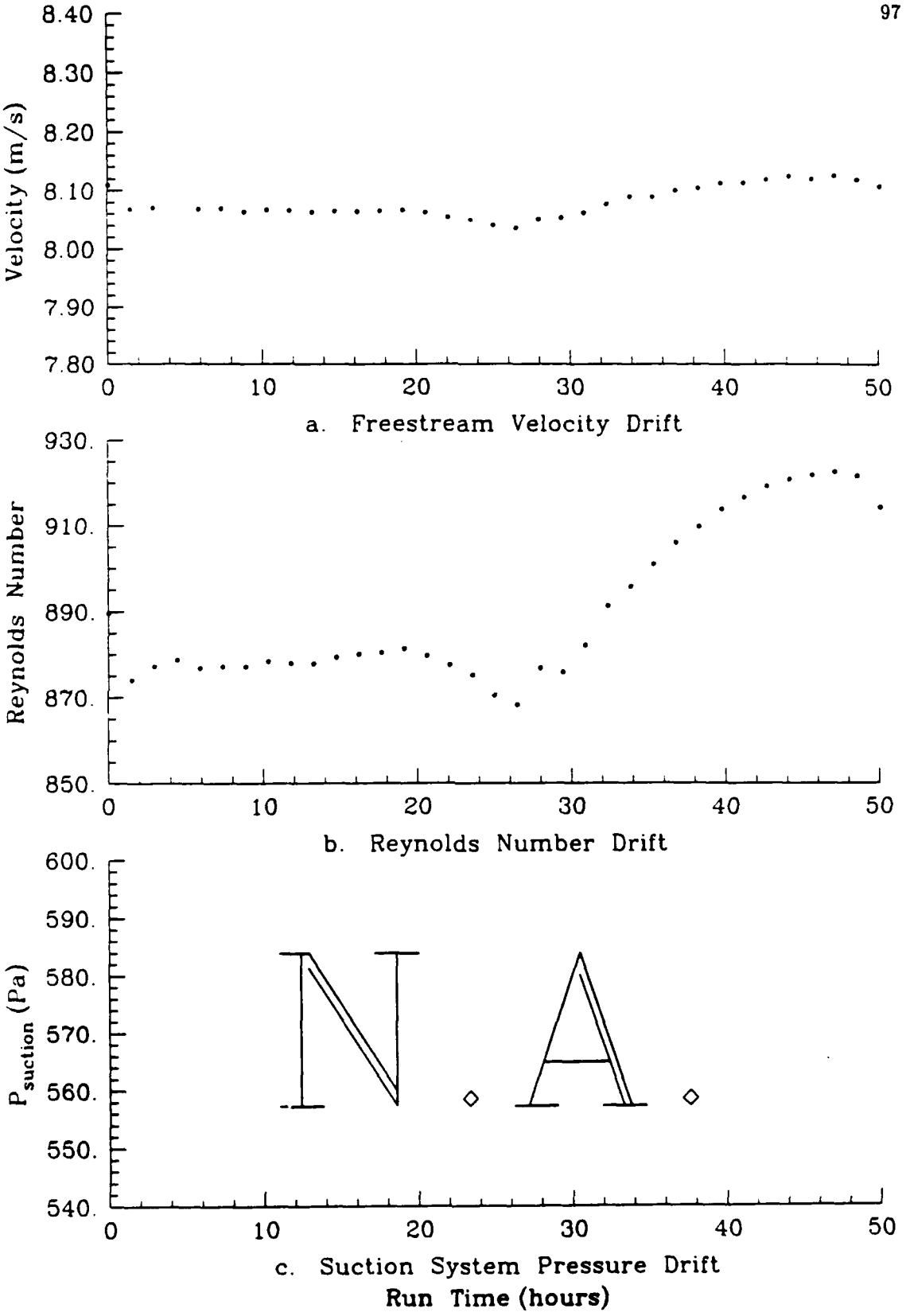

Figure D.7 Property Drifts for Experiment with: Porous Wall, No Suction (Q_s= 0)

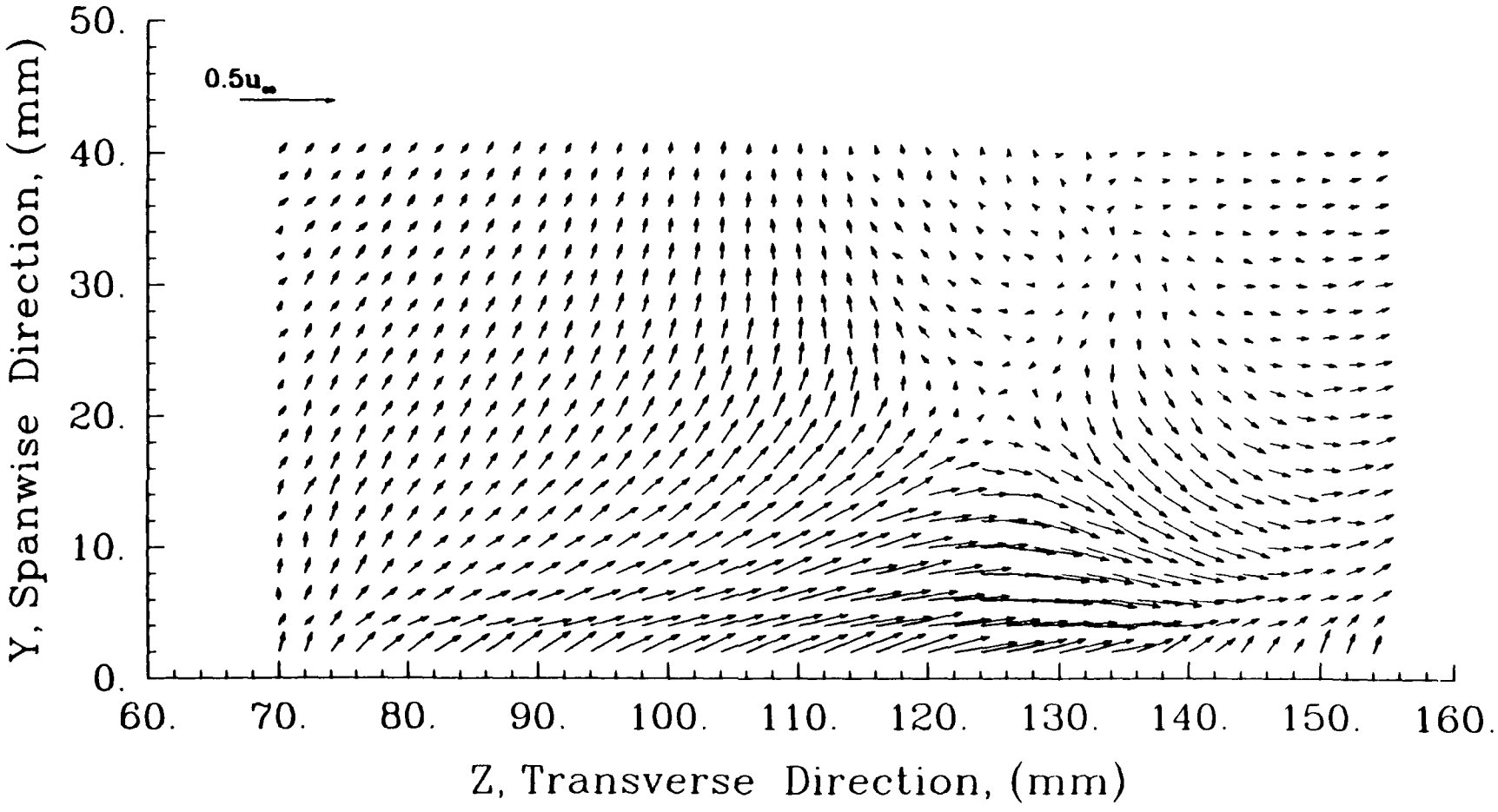

Figure D.8 Unfiltered Secondary Flow Velocity Vectors for Experiment with: Porous Wall, No Suction (Q_s= 0)

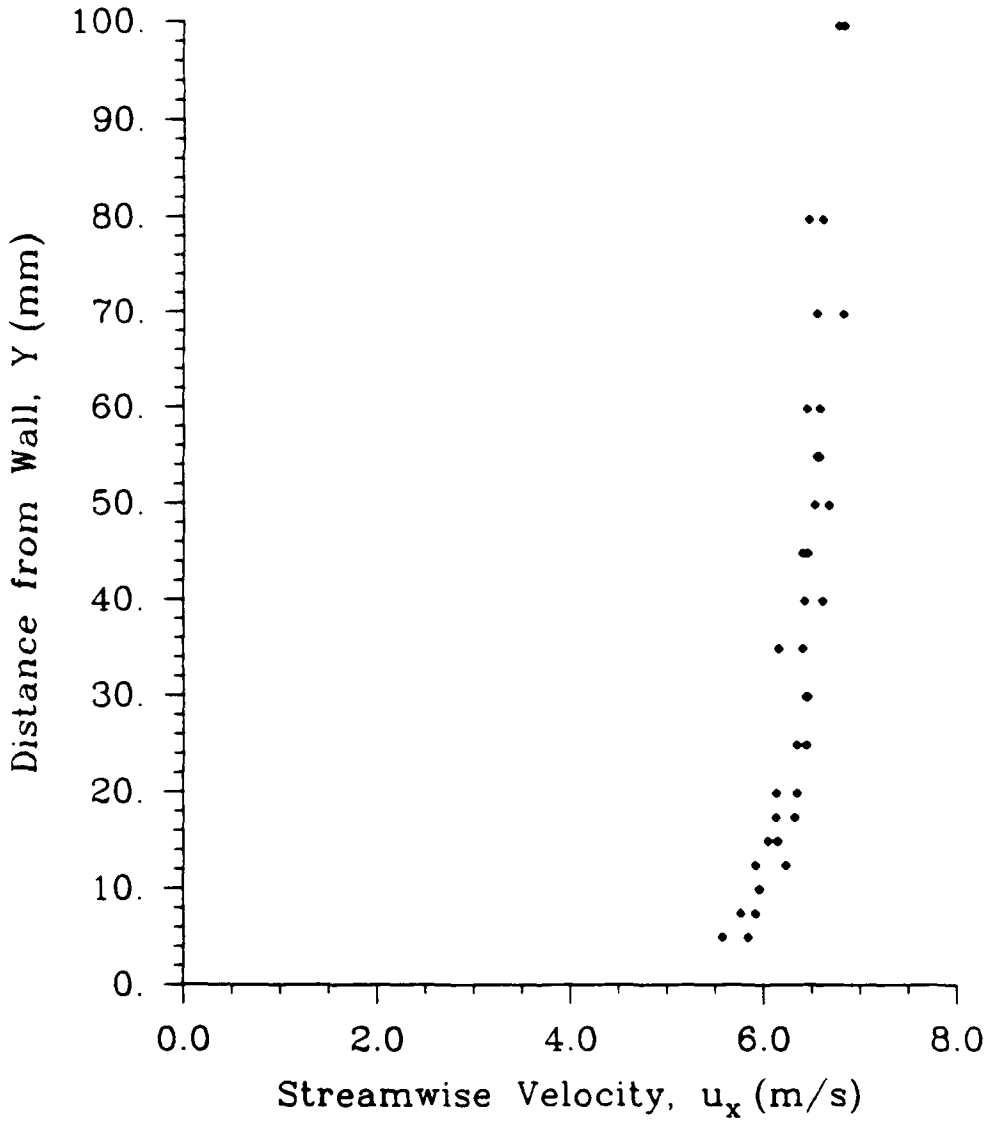

Figure D.9 Boundary Layer Survey for Experiment with: Porous Wall, Suction Applied $Q_s = 0.03\ m^3/s$

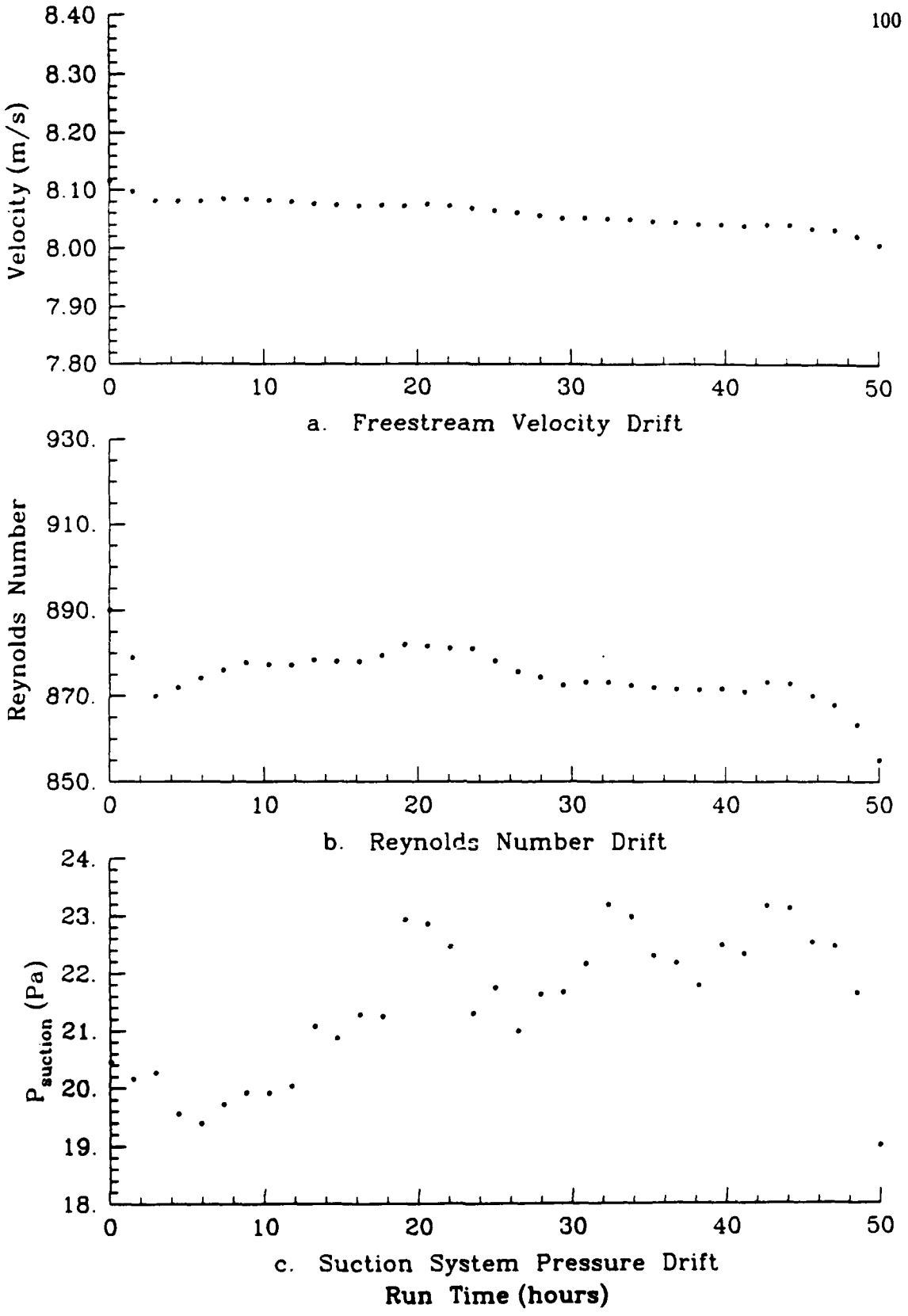

Figure D.10 Property Drifts for Experiment with: Porous Wall, Suction Applied Q_s= 0.03 m^3/s

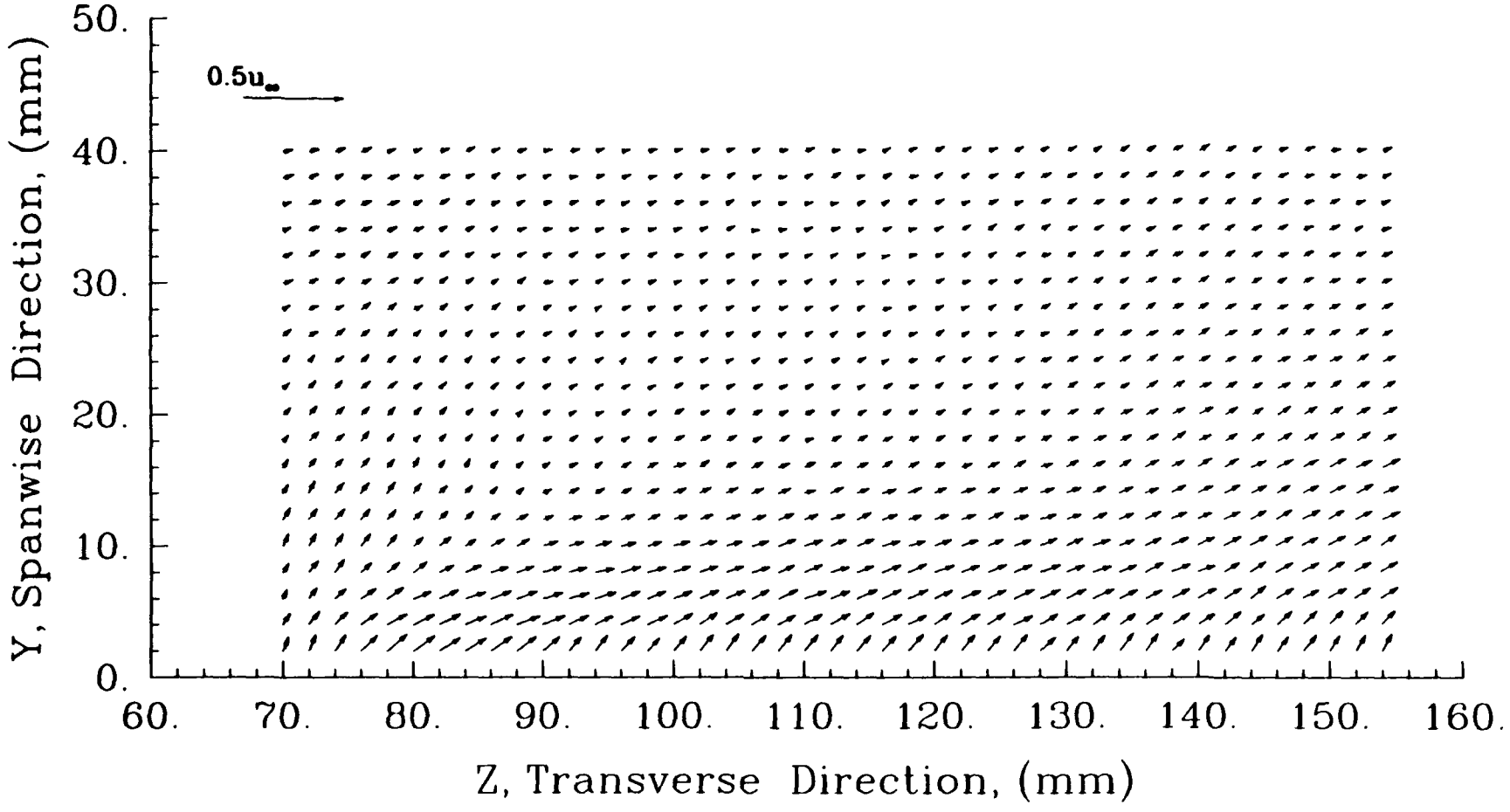

Figure D.11 Unfiltered Secondary Flow Velocity Vectors for Experiment with: Porous Wall, Suction Applied Q_s= 0.03 m^3/s

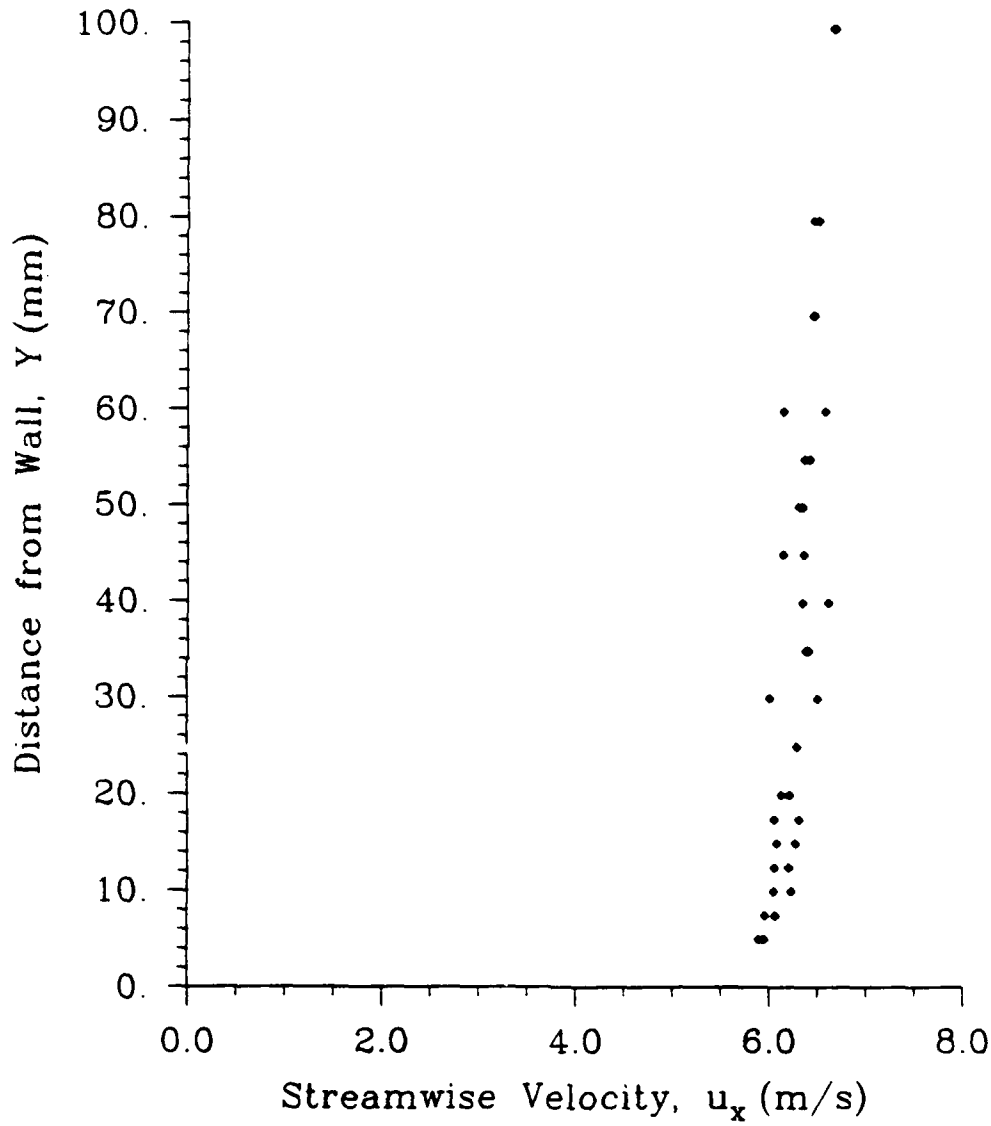

Figure D.12 Boundary Layer Survey for Experiment with: Porous Wall, Suction Applied Q_s= 0.04 m^3/s

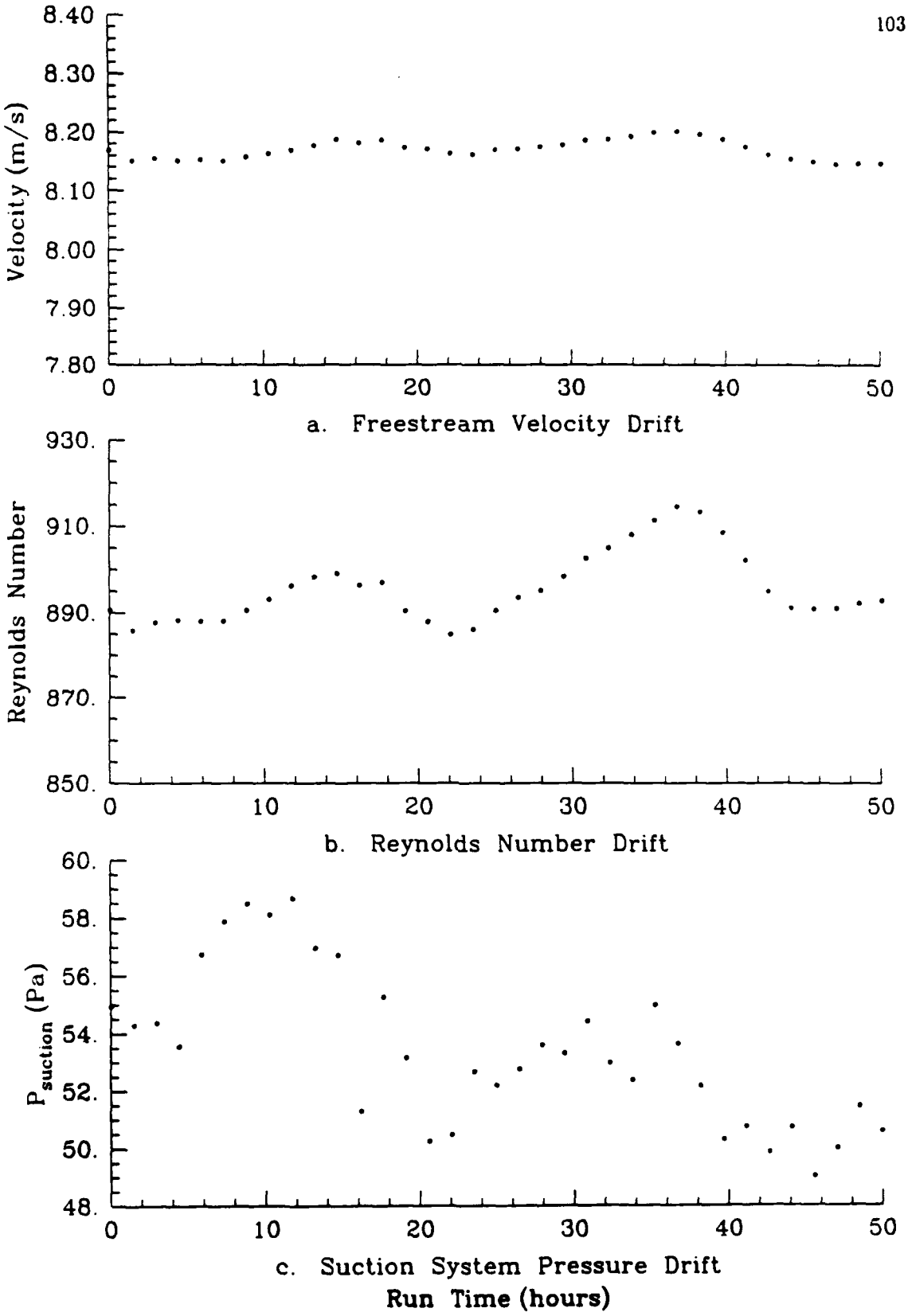

Figure D.13 Property Drifts for Experiment with: Porous Wall, Suction Applied $Q_s = 0.04\ m^3/s$

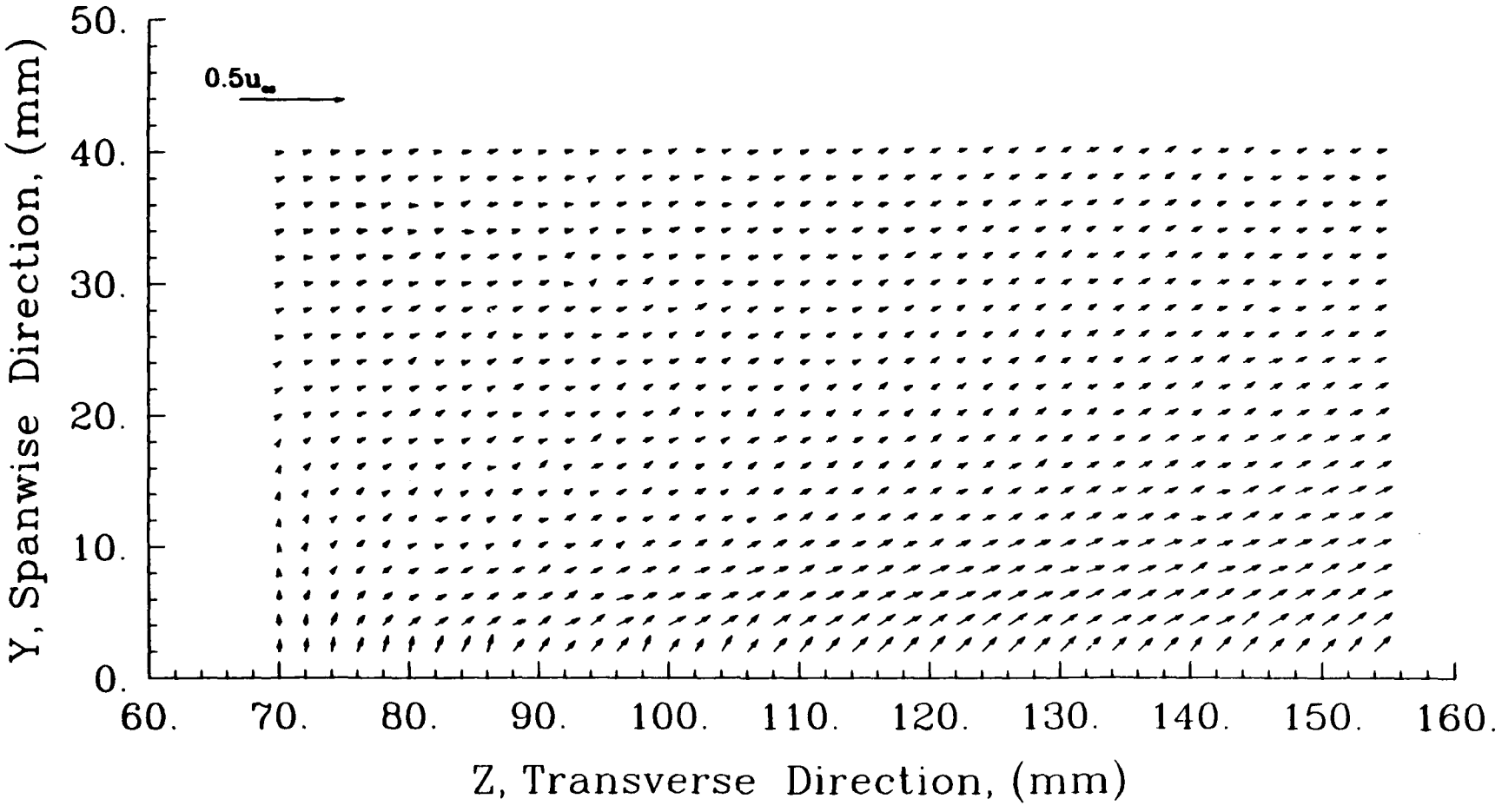

Figure D.14 Unfiltered Secondary Flow Velocity Vectors for Experiment with: Porous Wall, Suction Applied Q_s= 0.04 m^3/s

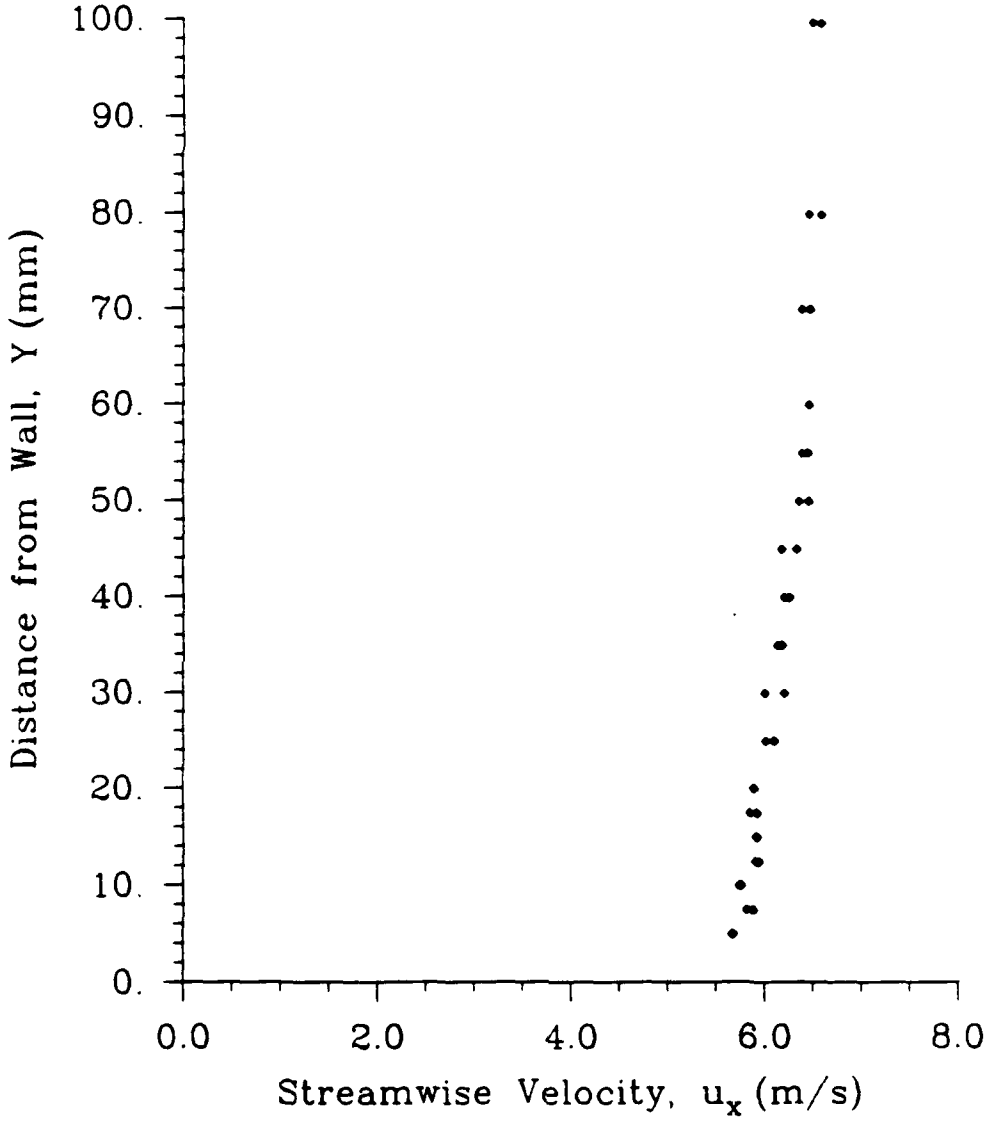

Figure D.15 Boundary Layer Survey for Experiment with: Porous Wall, Suction Applied Q_s= 0.05 m^3/s

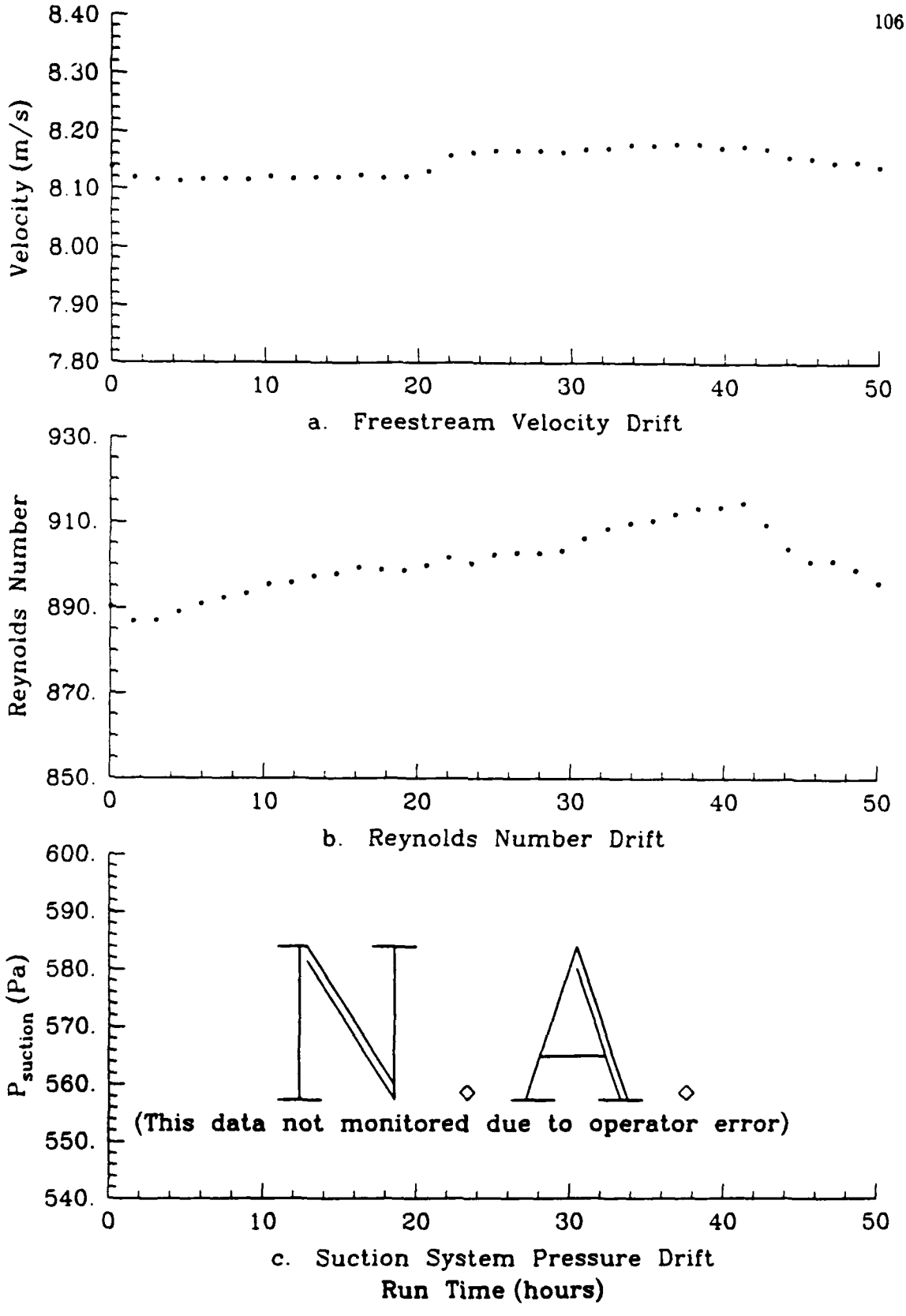

Figure D.16 Property Drifts for Experiment with: Porous Wall, Suction Applied $Q_s = 0.05 m^3/s$

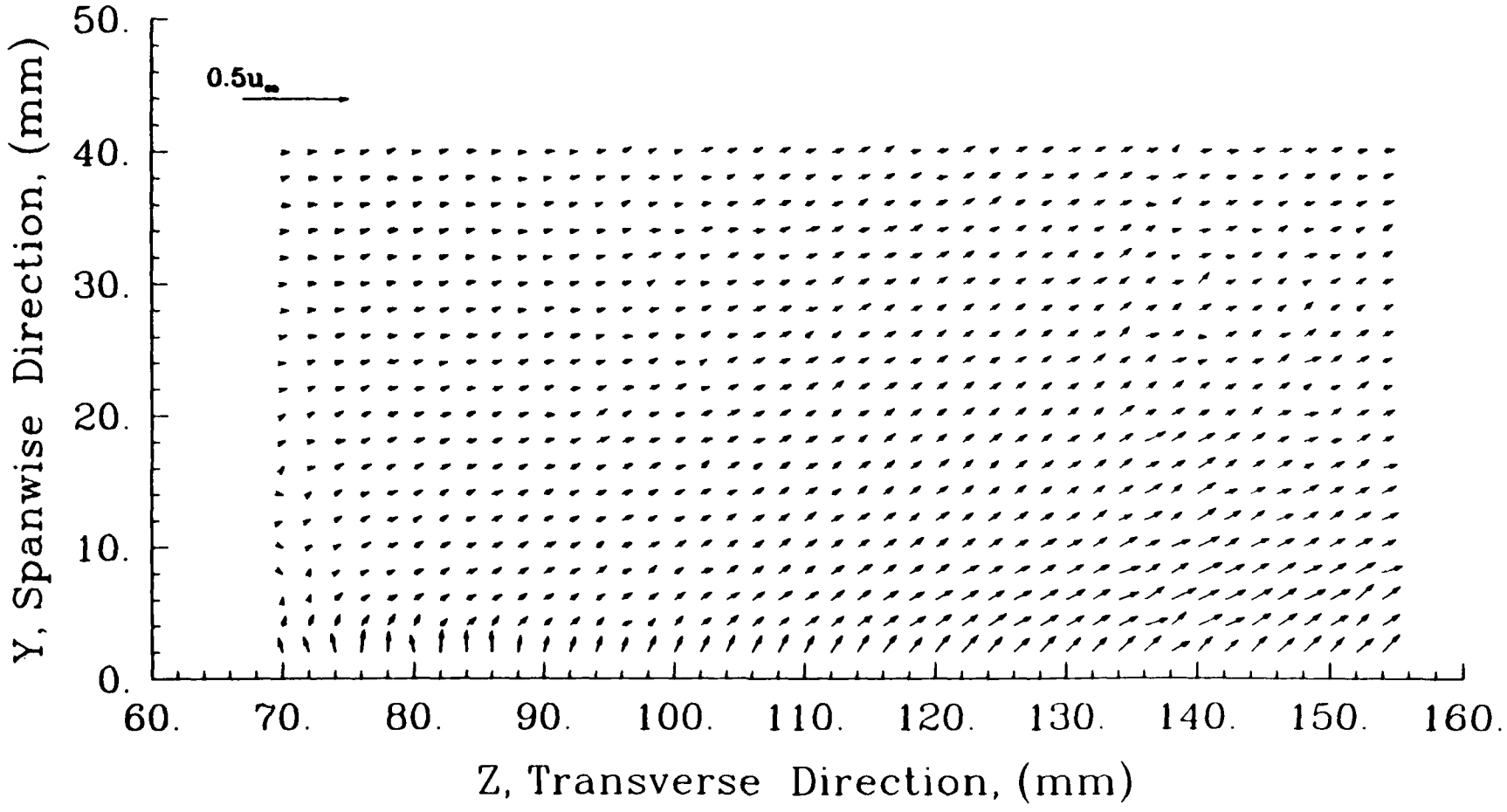

Figure D.17 Unfiltered Secondary Flow Velocity Vectors for Experiment with: Porous Wall, Suction Applied Q_s= 0.05 m^3/s

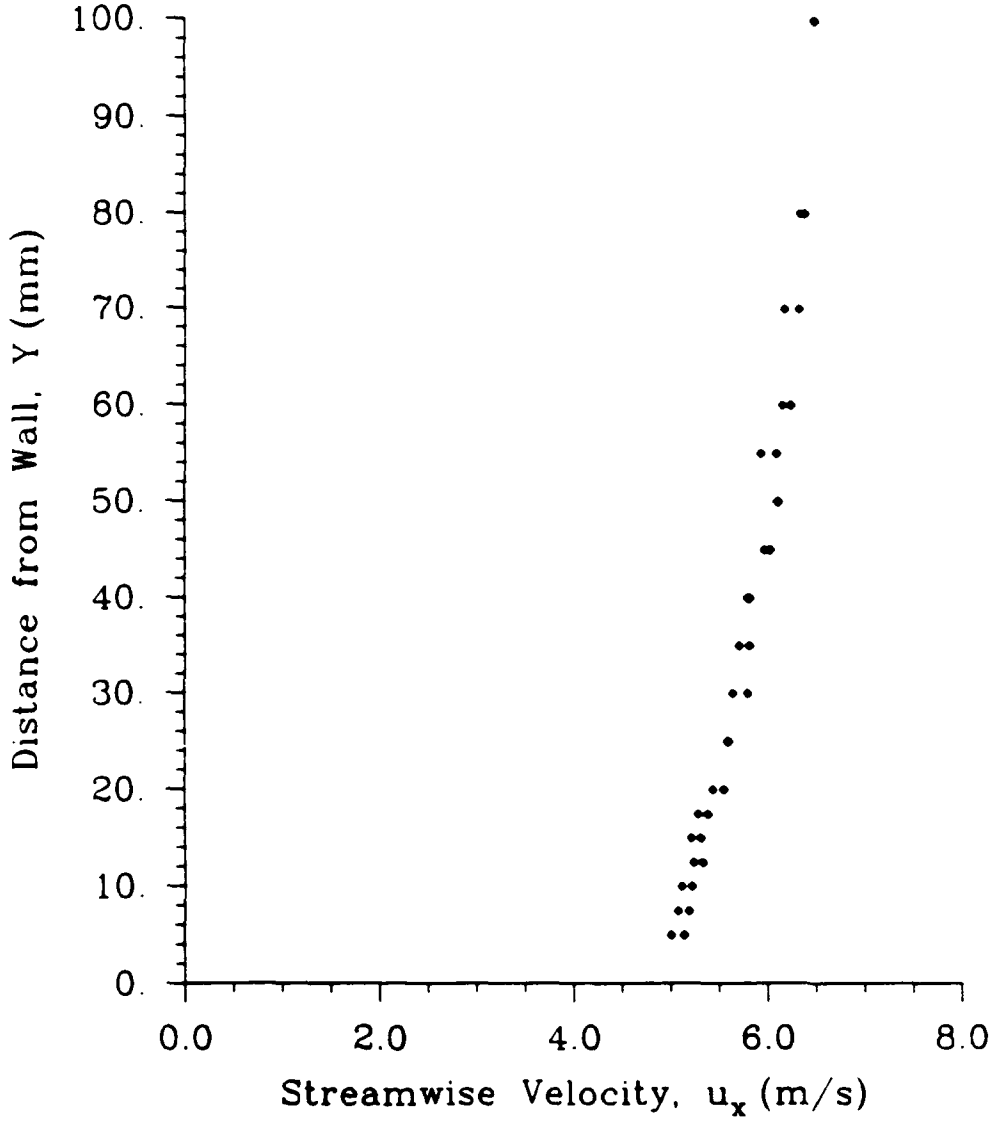

Figure D.18 Boundary Layer Survey for Experiment with: Porous Wall, Suction Applied Q_s= 0.09 m^3/s

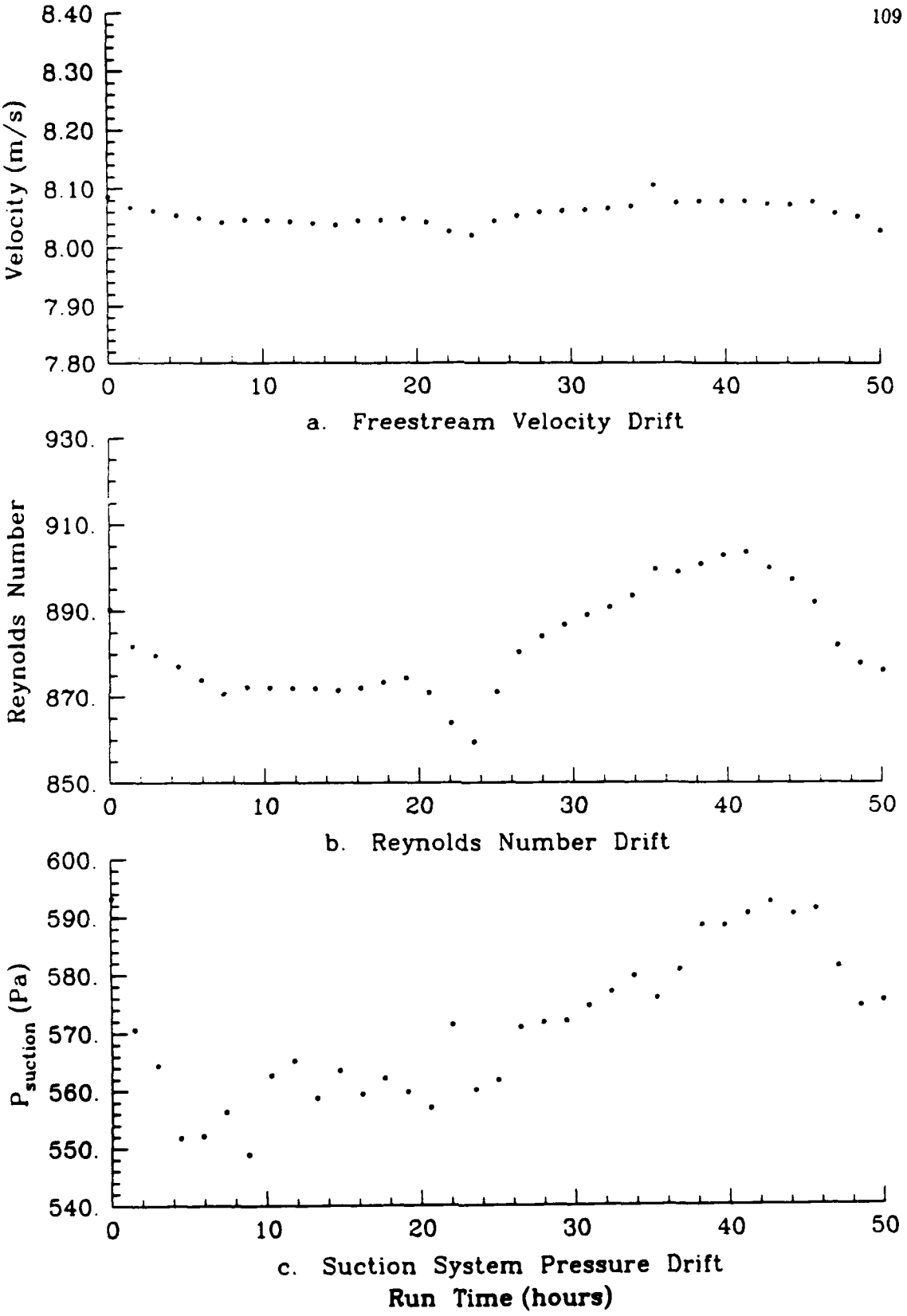

Figure D.19 Property Drifts for Experiment with: Porous Wall, Suction Applied $Q_s = 0.09\ m^3/s$

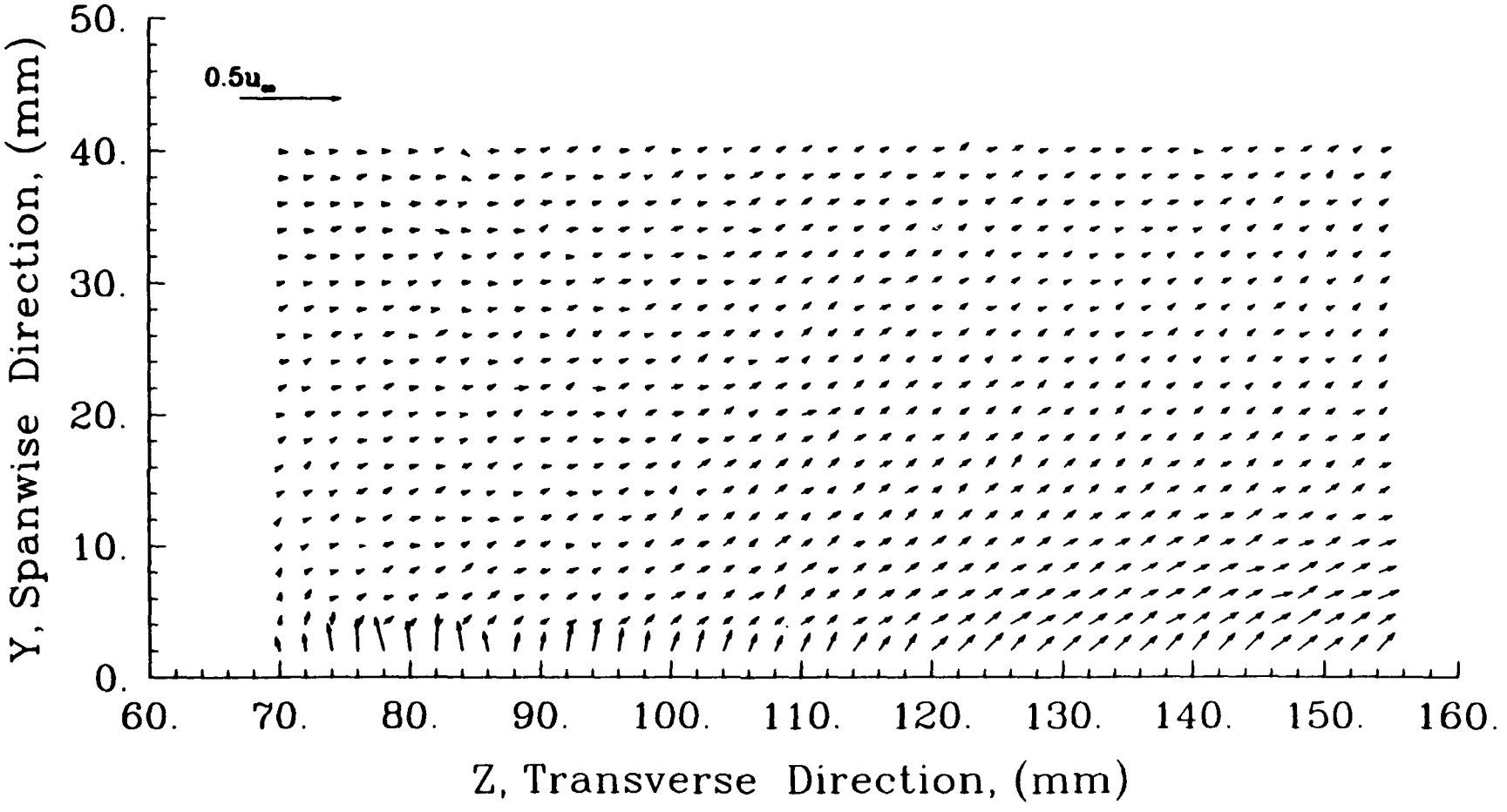

Figure D.20 Unfiltered Secondary Flow Velocity Vectors for Experiment with: Porous Wall, Suction Applied Q_s= 0.09 m^3/s